Durham E-Theses

Tephra characterisation of the 2013 eruption of San Miguel volcano, El Salvador

GUSTAV JOHN SEMANCHIK

How to cite:

SEMANCHIK, GUSTAV JOHN (2024) Tephra characterisation of the 2013 eruption of San Miguel volcano, El Salvador. Masters thesis, Durham University.

Use policy

The full-text may be used and/or reproduced, and given to third parties in any format or medium, without prior permission or charge, for personal research or study, educational, or not-for-profit purposes provided that:

- a full bibliographic reference is made to the original source
- a https://etheses.durham.ac.uk/id/eprint/15567/ is made to the metadata record in Durham E-Theses
- the full-text is not changed in any way

The full-text must not be sold in any format or medium without the formal permission of the copyright holders.

Please consult the full Durham E-Theses policy for further details.

Academic Support Office, The Palatine Centre, Durham University, Stockton Road, Durham, DH1 3LE
e-mail: e-theses.admin@durham.ac.uk Tel: +44 0191 334 6107
https://etheses.durham.ac.uk

Tephra characterisation of the 2013 eruption of San Miguel volcano, El Salvador

Gustav J. Semanchik

Thesis submitted in fulfilment of the degree of MSc by Research (MScR) in Earth Science

Department of Earth Science

Durham University

2021-2023

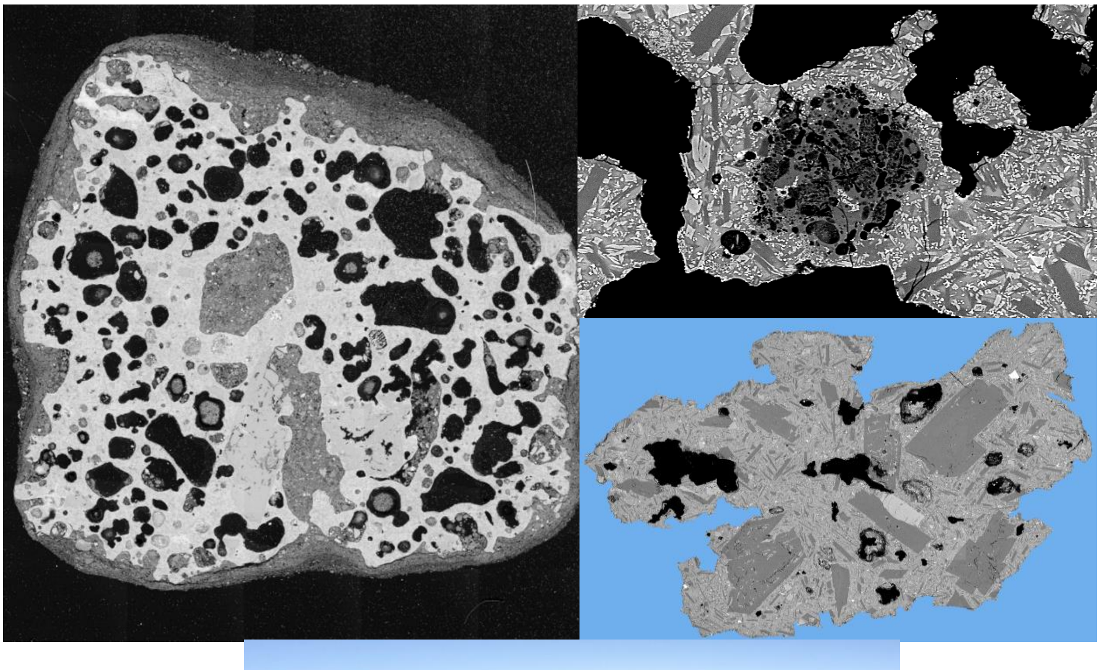

Figure Captions

Introduction

Figure 1.1: Volcanoes (triangles) along the Central American Volcanic Arc. San Miguel is located in eastern El Salvador (red triangle) (Granieri, 2015).

Figure 1.2: Map of the active volcanoes of El Salvador, including San Miguel (circled) (Escobar, 2003).

Figure 1.3: Location of the six monitored active volcanoes in El Salvador and nearby cities. Image of Ilopango Caldera (2016), San Salvador volcano (2017), Izalco volcano (2016), Santa Ana volcano (2018), San Vicente volcano (2018), and San Miguel (2020) (Gutierrez, 2021).

Figure 1.4: Geologic map of San Miguel volcano and the nearby Chinameca, Ojo de Agua, and Cerro Chambala volcanoes. Historic lavas, sample locations, important cities, towns, and roads are also depicted (Weber et al., 1978).

Figure 1.5: San Miguel volcano viewed from the SW (Photo: Brown, 2022).

Figure 1.6: Image of interior crater view of San Miguel volcano.

Figure 1.7: Volcanic rock classification diagram showing San Miguel rock sample geochemistry (145 samples) (Chesner et al., 2004).

Figure 1.8: Photographs and video stills of the eruption plume taken by observers on the ground (Brown et al., 2022).

Figure 1.9: Digital elevation model of El Salvador showing location of San Miguel volcano, major urban areas (black), and extent of the ash cloud (grey) at approximately 18.45 UTC on the 29th of December 2013 when the ash cloud then drifted in Honduras (Brown et al., 2022).

Figure 1.10: Aerial view of the volcano just after the December 29 eruption, showing the extent of singed vegetation of the coffee plantation (Brown, 2022).

Figure 1.11: Isopach map of tephra fall deposits. Contours are for 20, 10, 5, and 2 mm thickness (Brown et al., 2022).

Figure 1.12: Proximal deposits of the 2013 eruption. **A)** Indurated, grey ash coating on rocks on western inner crater wall. **B)** Large ballistic impact crater at 1360 m altitude on western flank, 1.6 km from the vent. **C)** Ballistic lithic clasts littering shoulder of volcano on upper SE flank. **D)** View east over the western bench of the crater. Unit C scoria fall deposit and ballistic clasts in foreground. Crater in mid-ground. Eastern bench and crater wall in background (taken from Brown et al., 2022).

Figure 1.13: Schematic cartoons for the key stages during the first 15 minutes of the eruption. Approximate timings given in seconds. The inset on the left shows the inferred magmatic plumbing system beneath San Miguel; the eruption was triggered when hotter basaltic melt mixed with colder basaltic andesite melt in a shallow crustal magma reservoir (Brown et al., 2022).

Methods

Figure 2.1: Sampled localities in and around San Miguel volcano. Image: Google Earth Pro.

Figure 2.2: Sedimentary log and grainsize histograms showing stratigraphic position and compositional data for samples (020/1, 020/4). Modified from Brown et al., 2022.

Figure 2.3: A) Photo and stratigraphic log of fall deposits different layers. **B)** Photo of Unit B ash aggregates, material samples are derived (from Brown et al., 2022).

Figure 2.4: Standard steps for coarse ash characterisation (Ross et al., 2021).

Figure 2.5: Sample 0201 under a binocular microscope showing black glassy juvenile ash particles and pale coloured lithic ash particles.

Figure 2.6: A, B) Two separate SEM images of the same grain being manually stitched together for complete grain image. **C)** Resulting single image of grain that was manually stitched tighter in Microsoft Photoshop.

Figure 2.7: Imported images in Photoshop being manually edited after automated sequence was ran by FIJI. **A)** Image of automated outline (above) and manual outline (below). **B)** Identified crack within particle to be filled in to prevent skewed numerical results. **C)** Outline between particle and debris or projection.

Figure 2.8: Resulting images produced from the (PASTA) program. **A)** RGB image of grain, **B)** silhouette of grain, and **C)** outline of particle.

Figure 2.9. Illustration displaying how quantitative measurements are calculated from particle outlines created in PASTA.

Results

Figure 3.1: Scoria clasts. **A)** typical scoria lapilli showing generally equant shapes and partial lithic ash coating. **B)** Plate scoria with ash coating. **C)** Zingg plot showing 3D shapes calculated using the 3 clast axes. Most scoria clasts fall into the equant or platy fields.

Figure 3.2: Mineral phases in the 2013 San Miguel scoria. **A)** Olivine-pyroxene micro-glomerocryst. **B)** Olivine micro-phenocryst with Fe-Ti oxide inclusion. **C)** Weakly zoned plagioclase phenocryst. **D**, **E)** Plagioclase-olivine glomerocryst. **F)** Olivine phenocryst.

Figure 3.3: **A-D)** Tachylite glass in scoria clasts. Not generally irregular shape of vesicles when compared with those in sideromelane glass. **E-G)** Sideromelane glass in scoria clasts. Note presence of subspherical vesicles, some of which have coalesced.

Figure 3.4: Contacts between sideromelane and tachylite glass in scoria clasts. **A)** Small domain of sideromelane (centre left) within tachylite. **B)** Irregular domain of tachylite within vesicular sideromelane. **C)** Sideromelane around tachylite with numerous complex-shaped vesicles.

Figure 3.5: Lithic-cored bombs collected in the field. **A)** Spherical bomb with platy lithic block inside. Note the thinning of the juvenile coating around the lithic clast. **B)** Exterior of spherical bomb. **C)** Composite bombs with abundant lithic clasts (white particles). **D)** Large lithic block with remnant juvenile rind. Photos: R Brown.

Figure 3.6: Lithic ash particles in scoria clasts. **A, B)** Heavily altered ash particles of pyroclastic rock. **C-F)** Heavily altered particles of crystalline lavas or scoria.

Figure 3.7: Deposits of the 2013 eruption of San Miguel. **A)** Indurated aggregate-rich Unit A, 2 km from the volcano. Deposit consists of poorly sorted aggregates and minor scoria and lithic ash particles. **B)** Loose aggregate rich Unit A. **C)** Matrix-rich Unit A with conspicuous large ash aggregates in a matrix of smaller aggregates and ash. **D)** Distal tephra fall deposit composed of ash aggregates and scoria clasts. Photos: R Brown.

Figure 3.8: Ash aggregate bulk samples. **A)** 2 mm size fraction of ash aggregates. B) 4 mm size fraction. **C)** 8 mm size fraction (with post-sieving broken fragments). **D)** Ash-coated scoria lapilli. Note different types of aggregates in A-C. Smooth surfaced, spheroidal ash pellets and irregular surfaced and more angular ash coated clasts.

Table 3.1: Ash lithofacies in the San Miguel ash aggregates.

Fig. 3.9: Examples of particle clusters (PC1) in massive, vesicular, poorly sorted ash (lithofacies MvA) in the core of an AP2 aggregate. Pore space defines irregular shaped, small PC1 aggregates.

Figure 3.10: Small coated particles (PC2) within AP1 and AP2 aggregates. **A-D)** Juvenile particles surrounded by a thin layer of fine ash. PC2 in B accreted at a late stage and sticks out from the edge of the aggregate. **E)** Lithic particle with fine ash coating within core of AP2 aggregate.

Figure 3.11: PC2 coated particles. **A)** Lava fragment partially surrounded in layers of ash (X). **B)** Hydrothermally altered lithic particle(s) with irregular coating of ash. **C)** Lithic particle composed of two crystals with partial ash coating. **D)** Hydrothermally altered lithic clast enclosed within several layers of ash.

Figure 3.12: PC2 coated juvenile particles. **A)** Poorly vesicular juvenile scoria particle enclosed in several layers of ash. **B)** Highly vesicular scoria particle with most vesicles open to the clast's exterior filled with ash. Closed vesicles in centre of clast remained empty. **C)** Juvenile clast enclosed in ash to form a spherical aggregate.

Figure 3.13: AP1 ash pellet aggregates. **A, B)** Small subspherical pellets. **C)** Larger pellet with several outsized ash particles.

Figure 3.14: Subspherical vesicles in massive, vesicular, poorly sorted ash (MvA) in AP1 aggregates.

Figure 3.15: AP2 accretionary pellets. **A, B)** Small accretionary pellets with one well developed finer-grained rim. **C, D)** details of rims in A, B. **E)** Poorly developed rims on a coated particle. **F)** Well developed rims around a coated particle.

Figure 3.16: Images of particle types: **A)** Melt-coated crystals, **B)** glassy particle, and **C)** melt coated lithic.

Figure 3.17: Groundmass textures in juvenile ash particles. **A, B)** Tachylite glass with irregular vesicles and diktytaxitic voids (B). Note lithic clast in upper half of B. **C, D)** Sideromelane glass with relatively low microlite contents.

Figure 3.18: Examples of fractured surfaces to volcanic ash particles. Solid arrows indicate crystals broken by fractures. Dotted arrows point to exteriors that have undergone plastic deformation (B, D).

Figure 3.19: Evidence for plastic deformation of juvenile ash particles, including retraction of filaments and vesicle walls and smooth bulbous exteriors.

Table 3.2: Mean axial ratio and form factor values of juvenile ash particles.

Figure 3.20: Axial ratio vs. form factor is plotted in comparing the three separate deposits. Silhouettes of representative particles are shown along the edge of the graph, tied to their sample dots on the graph.

Figure 3.21: Plots the same data as Figure 3.20, only now with the backscattered SEM images of the particles previously shown as silhouette images. Displaying the relationship between particle texture/composition and morphological form.

Figure 3.22: Convexity vs. solidity is plotted in comparing the three separate deposits. Silhouettes of representative particles are shown along the edge of the graph, tied to their sample dots on the graph.

Figure 3.23: Plots the same data as Figure 3.22, only now with the backscattered SEM images of the particles previously shown as silhouette images. Displaying the relationship between particle texture/composition and morphological roughness.

Table 3.3: Mean convexity and solidity values of juvenile ash particles.

Interpretation

Figure 4.3.1: San Miguel samples 0201, 0204 and SM007C: Comparison of convexity, solidity, axial ratio and form factor (Located in Appendix).

Figure 4.3.2: Comparison of convexity and solidity for San Miguel and selected historic eruptions (Liu et al., 2015) (Located in Appendix).

Figure 4.3.3: Comparison of axial ratio and form factor for San Miguel and selected historic eruptions (Liu et al., 2015) (Located in Appendix).

Table 4.3.1: San Miguel's mean values of convexity, solidity, axial ratio, and form factor compared to other eruptions studied by (Liu et al. 2015).

Abstract

On December 29th, 2013, San Miguel volcano, located in the south-eastern region of El Salvador, erupted after ~40 years of inactivity. The VEI 2 eruption was multi-phased and lasted for ~2 hours. The eruption ejected approximately 10^6 m^3 of ash across more than 20,000 km^2 of El Salvador extending into Honduras. The only reported damage took place in the coffee plantations on the flanks of the volcano. This eruption was of significant importance given the safety of the coffee plantation workers. In addition, approximately 70,000 people live within a 10 km radius of the vent. The abrupt nature of this eruption is also of cause for concern; a larger eruption with as little warning would be very hazardous.

Analysis and reconstruction of the eruption is based on an assortment of video evidence, photographs, and laboratory results from field sampling. Five eruptive phases occurred during the December 29th, 2013 eruption of San Miguel, including vulcanian eruptions, a pyroclastic density current, and multiple ash plumes. The eruption was a result of reactivation and mixing of the contents of underlying magma chambers.

The purpose of this study is to aid in the understanding of this particular eruption and to expand the scientific database. Scoria, ash aggregates, and juvenile ash particles collected from the eruption were analysed for compositional and textural evidence of the nature of the eruption. Ash aggregates and lithic fragments in scoria samples provide evidence of a phreatomagmatic event. Different glass types (tachylite and sideromelane) discovered in all three types of material indicate differential magma fragmentation and movement. Different internal lithofacies of ash aggregates result from the interaction with a pyroclastic density current. A transition in tephra deposits from lithic-rich to more juvenile-rich clasts support the conclusion that the eruption transitioned from partly phreatomagmatic to magmatic.

Chapter 1: Introduction

1.1 Volcanism in Central America

The Central American Volcanic Arc (CAVA) is a chain of volcanoes that stretches approximately 1,200 km from southern Mexico to Panama. Volcanism here is due to the eastward subduction of the Cocos Plate underneath the Caribbean Plate along the Middle American Trench (Stoiber and Carr, 1973; Leeman et al., 1994; Chesner et al., 2004; MacMillan et al., 2004) (Figure 1.1). It is also a region of frequent earthquakes (Protti et al., 1995). The Cocos Plate is located at the East Pacific Rise and Cocos Ridge, and subducts at angles of 55° to 65° along the Central American Volcanic Arc (Syracuse and Abers, 2006). Volcanic structures in the CAVA range from cinder cones and domes to major stratovolcanoes. This volcanic arc contains some of the world's most active volcanoes, such as Fuego in Guatemala, Arenal in Costa Rica, and San Miguel in El Salvador.

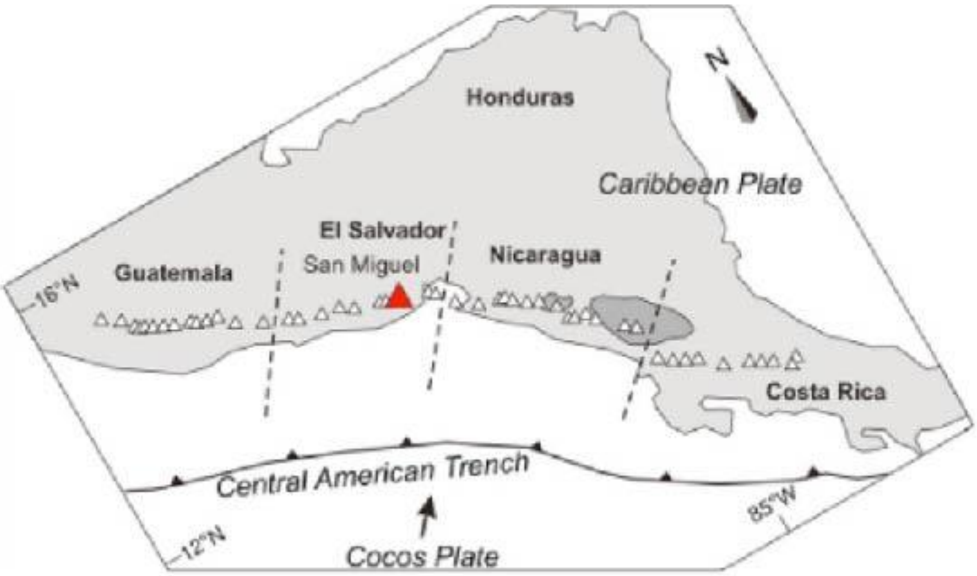

Figure 1.1. Volcanoes (triangles) along the Central American Volcanic Arc. San Miguel is located in eastern El Salvador (red triangle) (Granieri, 2015).

1.2 Volcanism in El Salvador

El Salvador is one of the most geologically active regions in the world. This is evident with more than 90 % of the country's subsurface consists of Cenozoic and Quaternary volcanic materials (Gutierrez, 2021). Volcanic edifices in El Salvador take the form of stratovolcanoes, calderas, and volcanic fields containing maars and cinder cones (Global Volcanism Program, 2023). Volcanic composition ranges mostly from basalt to basaltic-andesite to andesite; the variation is attributed to differential crustal fractionation processes and crustal thickness (Carr, 1981; Scarlato et al., 2016). Volcanic products and hazards include lava flows, ash, coarser pyroclastics such as lapilli, blocks and bombs, airfall deposits, pyroclastic density currents and lahars (Scarlato et al., 2016; Major et al., 2001). Figure 1.2 shows the location of El Salvador's active volcanoes. Six of these volcanoes are currently systematically monitored (Gutiérrez, Carcamo, 2021; MARN 2019): Izalco, Santa Ana, San Salvador, Ilopango, San Vicente, and San Miguel volcanoes (Figure 1.3). Izalco (1950 m.a.s.l.), Santa Ana (2381 m.a.s.l.), San Salvador (1890 m.a.s.l.), San Vicente (2182 m.a.s.l.),

Figure 1.2. Map of the active volcanoes of El Salvador, including San Miguel (circled) (Escobar, 2003).

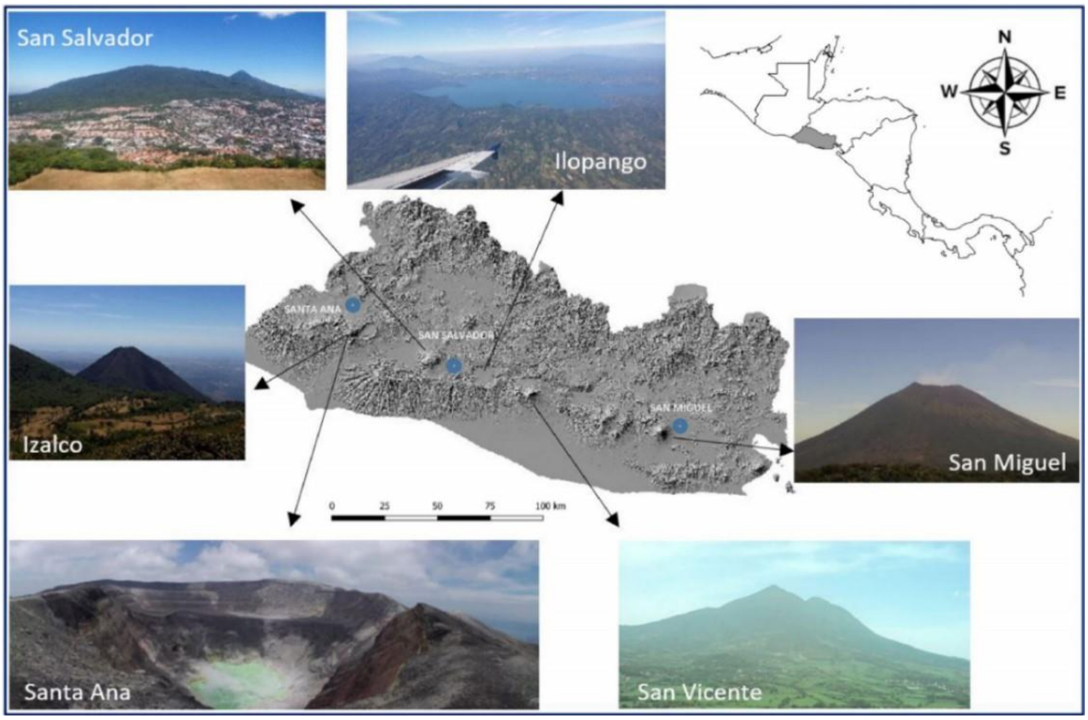

Figure 1.3. Location of the six monitored active volcanoes in El Salvador and nearby cities. Image of Ilopango Caldera (2016), San Salvador volcano (2017), Izalco volcano (2016), Santa Ana volcano (2018), San Vicente volcano (2018), and San Miguel (2020) (Castro and Gutierrez, 2021).

and San Miguel (2130 m.a.s.l.) are stratovolcanoes of basaltic-andesitic to andesitic composition, while Ilopango is a large rhyodacitic caldera structure (~13 × 17 km in size) (Gutierrez., 2021). Other volcanic features in El Salvador include arc-related composite volcanoes, dacitic domes, monogenetic fields, and several silicic calderas (Lexa et al., 2011).

1.3 San Miguel Volcano

San Miguel volcano, locally known as Chaparrastique, is located in southeastern El Salvador, 12 km southwest of the town of San Miguel. It is a 2130 m high conical stratovolcano with a symmetrical cone and upper slopes of >40° (Figures 1.4 and 1.5). The region is largely rural, with farms and coffee plantations extending up the flanks of the volcano (Chesner et al., 2004; Scarlato et al., 2016). San Miguel volcano is El Salvador's most active volcano, with 25-28 eruptions in the past 500 years (Escobar et al., 2016; Jiménez et al., 2020). It is

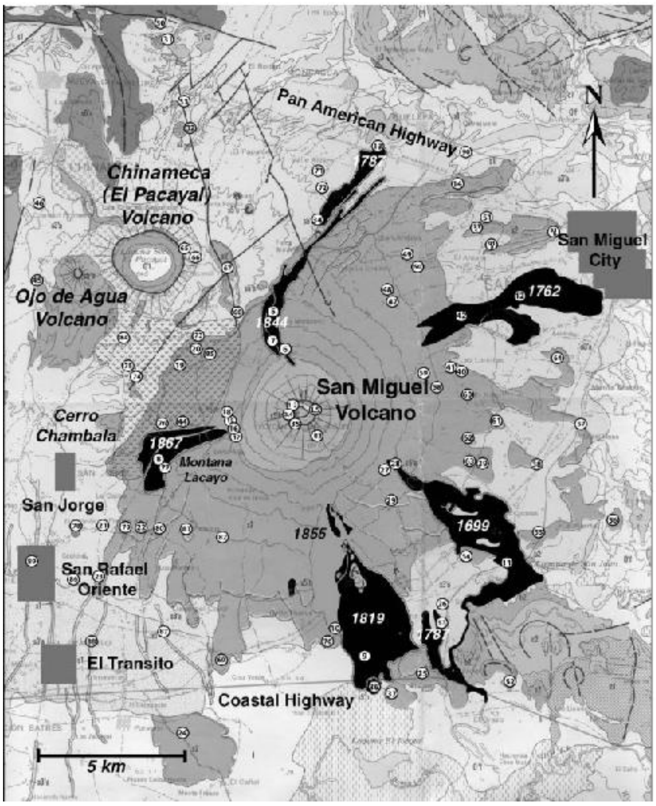

Figure 1.4. Geologic map of San Miguel volcano and the nearby Chinameca, Ojo de Agua, and Cerro Chambala volcanoes. Historic lavas, sample locations, important cities, towns, and roads are also depicted (Escobar., 2003).

Figure 1.5. San Miguel volcano viewed from the SW (Photo: Brown, 2022).

estimated to be at least Holocene in age (active for about 10,000 years), with several phases of cone creation (Escobar, 2003; Dzierma and Wehrmann, 2014). Eight flank lava flows have produced an estimated total volume of 0.51 km^3, with the longest lava flow extending 8 km from the vent (Escobar, 2003). Eruptions are typically VEI 1-2, and typically are Strombolian in nature, ejecting spatter and ash, with occasional summit lava fountains and flank lava flows (Escobar, 2003). At least thirteen small-volume tephra-producing eruptions have occurred since 1844 (Chesner et al., 2004). The summit crater has a diameter of approximately 900 m and depth of approximately 350 m. The crater is characterized by two distinct benches and a deeper internal with a diameter of approximately 500 m (Escobar, 2003; Figure 1.6).

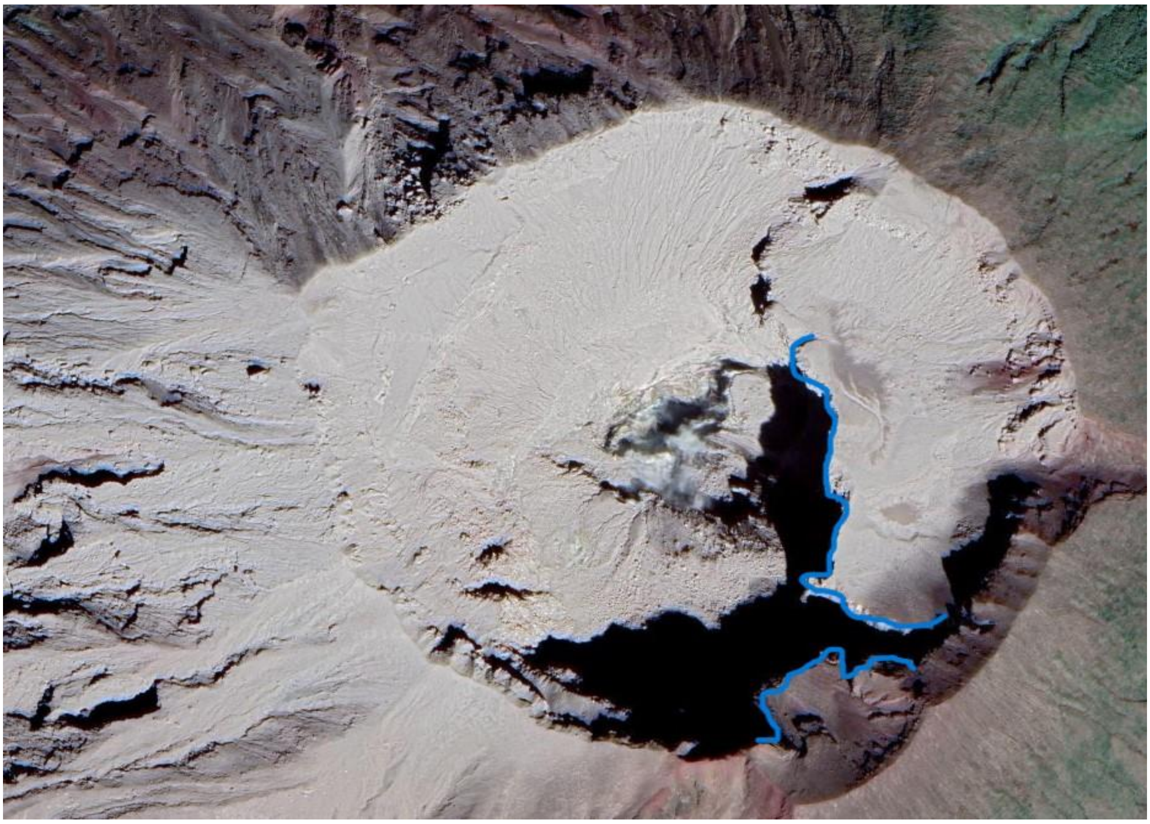

Figure 1.6. Image of interior crater view of San Miguel volcano.

The volcano is mainly composed of lava flows and interbedded scoria and ash fall deposits. Lavas are basalt to basaltic andesite (51-53 wt.% SiO_2), while tephra is slightly more silicic (50-59 wt.% SiO_2) (Carr et al., 1980; Chesner et al., 2004; Scarlato et al., 2016; Figure 1.7). Deposits from pyroclastic density flows and phreatomagmatic eruptions are rare due to rapid weathering and erosion from the wet tropical climate (Cole, 2015).

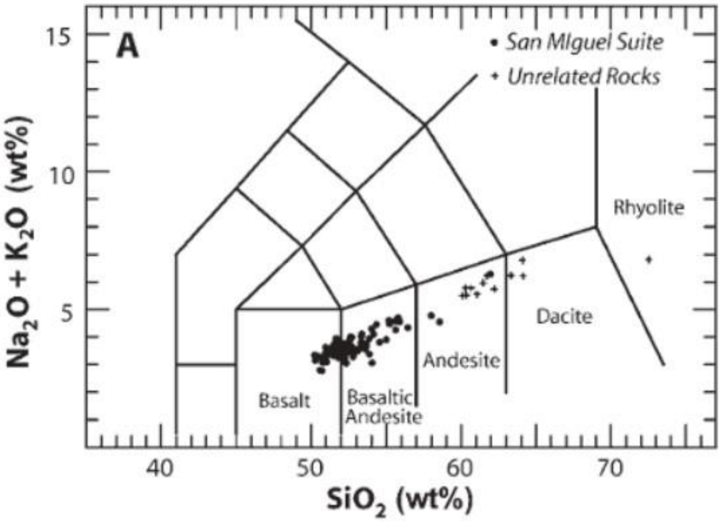

Figure 1.7. Volcanic rock classification diagram showing San Miguel rock sample geochemistry (145 samples) (Chesner et al,. 2004).

1.4 The December 29th, 2013, eruption of San Miguel volcano

After twelve years of inactivity, San Miguel erupted on December 29th, 2013. The eruption was captured on webcam footage taken from the extinct El Pacayal volcano, located to the northwest of San Miguel (Figure 1.8). The footage provides a glimpse of the early stages of the eruption and captures the main eruptive phases that occurred over approximately two hours.

The eruption was preceded by an increase in SO_2 outgassing beginning in November, 2013, with emissions doubling from December 27th until December 29th (Granieri et al., 2015). Other than this, the eruption of December 29th occurred with little warning (Brown et al., 2014).

Figure 1.8. Photographs and video stills of the eruption plume taken by observers on the ground (Brown et al., 2022).

The SO_2 emissions just prior to eruption suggest the migration of hot fluids (gas, water and magma) into the volcano's shallow plumbing system (Scarlato, 2016). Scarlato et al. (2016) and Brown et al. (2022) suggest that the eruption began with the intrusion of hot basaltic melt into a colder basaltic-andesite melt, and then by the explosive interaction of rising basaltic-andesite magma and groundwater in a shallow hydrothermal system.

The eruption began at 10:30 a.m. Central Standard Time with steam, gas and ash emissions, and then two powerful Vulcanian-type explosions (VEI 2) that culminated in a sustained eruption column (Scarlato et al., 2016). The resulting ash plume reached a height of 9-10 km (Scarlato et al., 2016; Brown et al., 2014). Approximately 5000 people were evacuated from a 3-km radius around the volcano (Martinez-Hackert et al., 2015). The eruption resulted in the downwind deposition of ash (Figures 1.9 and 1.10). The second explosion also resulted in a short-lived pyroclastic density current (PDC) that travelled ~500 m down the flanks of the volcano, entering high-elevation coffee plantations (Scarlato et al., 2016; Brown et al., 2014). Cole (2015) estimates that approximately 10^6 m^3 ash was ejected from the volcano. The eruption also formed a spatter cone in the central crater (Scarlato et al., 2016), but overall the eruption was different from historic eruptions from San Miguel in that no lava flows were produced (Brown et al., 2014).

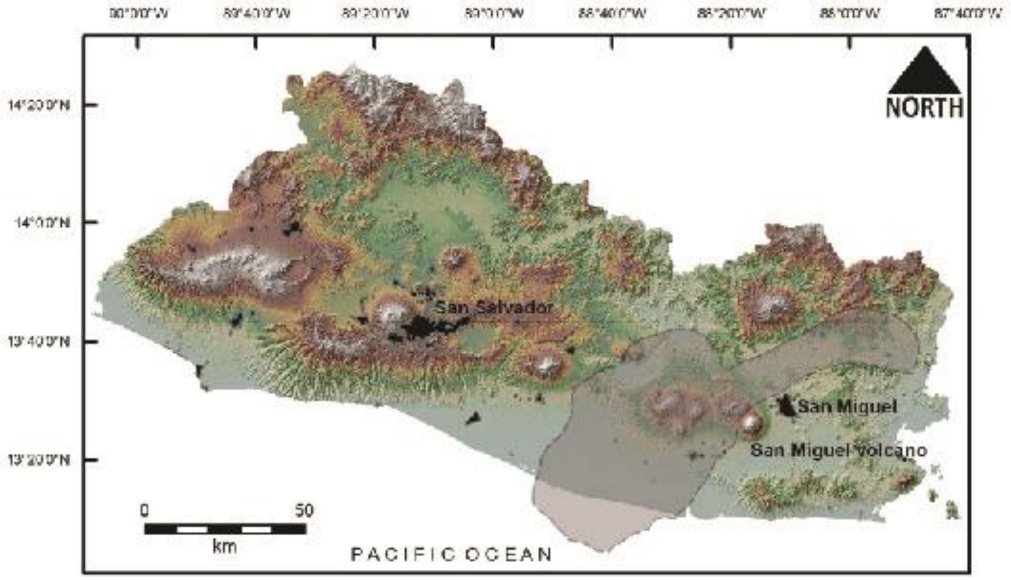

Figure 1.9. Digital elevation model of El Salvador showing location of San Miguel volcano, major urban areas (black), and extent of the ash cloud (grey) at approximately 18.45 UTC on the 29th December, 2013 when the ash cloud then drifted in Honduras (Brown et al., 2022).

Figure 1.10. Aerial view of the volcano just after the December 29 eruption, showing the extent of singed vegetation of the coffee plantation. (Brown, 2022).

Juvenile material ejected during the eruption is mostly scoriaceous in texture, and basalt to basaltic andesite (50-53 wt.% SiO_2) in composition (Scarlato et al., 2016). Phreatomagmatism would create the ash aggregates, ash-coated scoria clasts, and ash plastered to crater surfaces; a magma component is required to account for the presence of juvenile material in the PDC (Brown et al., 2022). Scarlato et al. (2016) observed distinct phenocryst populations and used mineral-melt equilibria to show how mixing between high-temperature basaltic magma and low-temperature basaltic andesite magma could result in the observed mineralogy. Mixing between two chemically distinct magmas is also evidenced by the presence of reverse zoned plagioclase phenocrysts with resorbed sodic cores and regrowth of sieve-textured calcic mantles.

Brown et al. (2022) reconstructed the eruption using video, photographs, and samples from pyroclastic deposits that were collected in the spring of 2014. Samples were taken from the crater walls and from the flanks of the volcano. Figure 1.11 is an isopach map showing the distribution of tephra fall deposits. Within the crater, the uppermost and lowermost beds were identified as tephra fall deposits, and the others were PDC deposits (Figure 1.12). The tephra fall deposits contained white ash-coated clasts and ash aggregates, fine grey ash and coarse ash/fine lapilli-grade scoria (Brown et al., 2022). Brown et al. (2014) estimated that the tephra fall deposits had an overall volume of 1.4 x 10^5 m^3, acknowledging that uncertainties in determining bed thickness and erosion of deposits would give the volume estimate a large potential error. Brown et al. (2022) classify the PDC deposits as proximal (within the crater) and distal (on the upper flanks of the volcano). Proximal PDC deposits consisted of poorly-sorted, diffusely-bedded, lithic-rich tephra, with median particle diameters of 0.5-2 mm. Distal PDC deposits consisted of moderately-sorted, massive- to weakly-stratified, lithic-rich

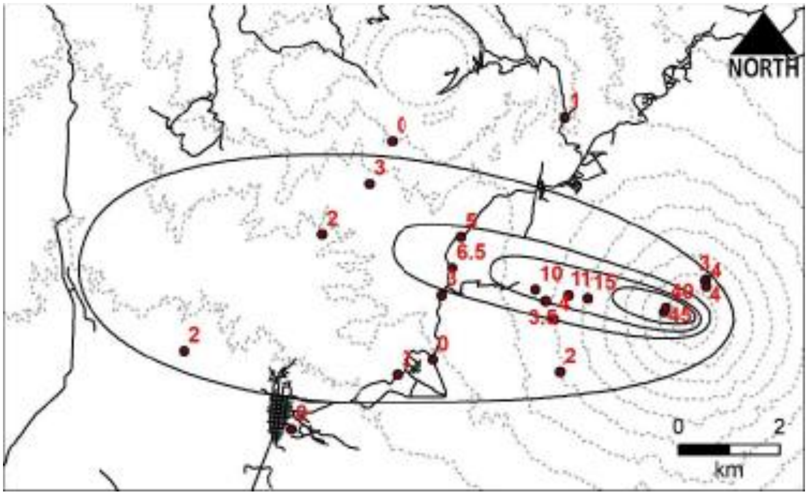

Figure 1.11. Isopach map of tephra fall deposits. Contours are for 20, 10, 5 and 2 mm thickness (Brown et al., 2022).

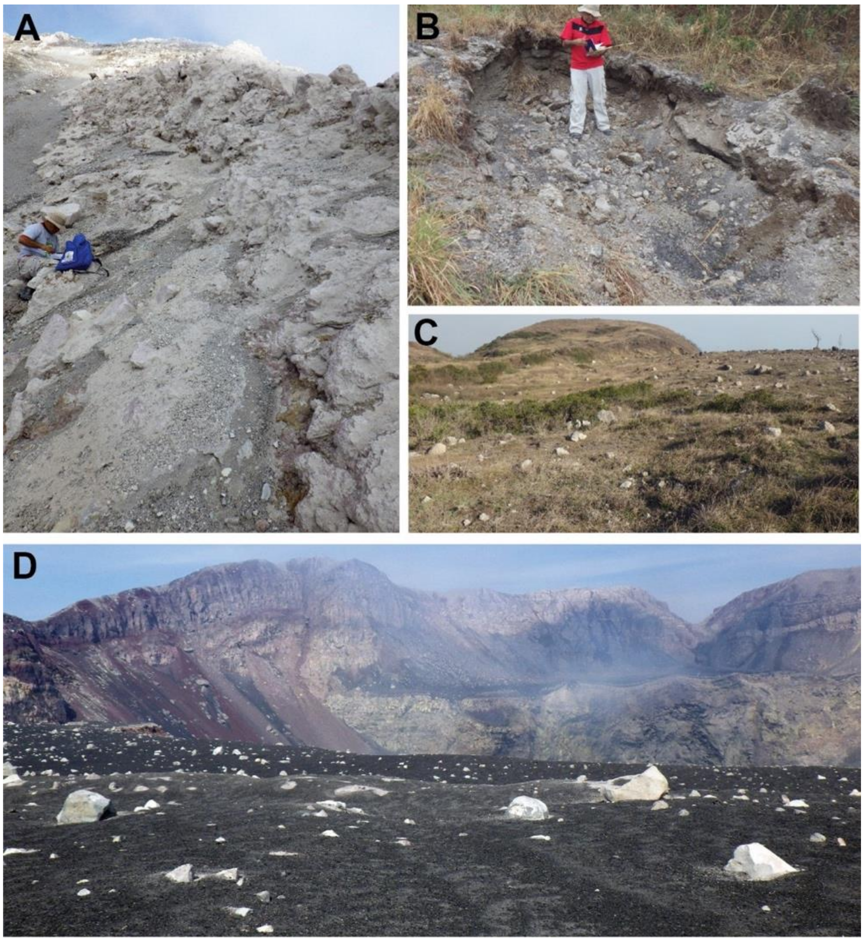

Figure 1.12. Proximal deposits of the 2013 eruption. A) Indurated, grey ash coating on rocks on western inner crater wall. B) Large ballistic impact crater at 1360 m altitude on western flank, 1.6 km from the vent. C) Ballistic lithic clasts littering shoulder of volcano on upper SE flank. D) View east over the western bench of the crater. Unit C scoria fall deposit and ballistic clasts in foreground. Crater in mid-ground. Eastern bench and crater wall in background (taken from Brown et al., 2022).

tephra, with median particle diameters of 0.25-0.5 mm. The PDC deposits were 15-50 cm thick in the crater, and 1.5-10 cm thick on the flanks. Brown et al. (2022) used average thicknesses in the crater and on the flanks to calculate a total PDC volume of approximately 2.7-3.7 x 10^5 m^3. This correlates to a dense rock equivalent of 2-5 x 10^4 m^3, based on estimates of deposit porosity, lithic content and vesicularity. The total deposit volume (including the tephra fall and PDC) is estimated to be 10^6 m^3, with a dense rock equivalent of 0.0003 km^3 (Brown et al., 2022).

1.5 Eruption Summary

Brown et al. (2022) used video analysis to divide the eruption into five phases. These are summarized as follows:

Phase 1 lasted approximately 50 minutes. It began with a few minutes of water vapor emissions followed by Vulcanian explosions that ejected a dark, ash-laden eruption column that quickly reached a height of approximately 1.5 km, followed by another eruption plume. The two separate plume heads rose at an estimated velocity of 70 m/s. Part of the second plume fountained back to the ground and formed a pyroclastic density current (PDC) which travelled approximately 1 km down the volcano's sides. It then lofted and merged with the vent-derived eruption plume. A spreading umbrella cloud appeared concurrently, shedding tephra over the northwest flank of the volcano. Phase 1 ended with a decrease in eruption intensity and a short (~8 minute) quiet period.

Phase 2 was marked by rapid explosions that created a dark, ash-laden eruption column rising at rates up to 50 m/s. By this time the ash plume had reached an elevation of approximately 9 km and was beginning to drift towards the northeast and into Honduras.

Phase 3 lasted 18 minutes and consisted of a diminution of ash eruption. The plume head spread laterally just below and into the umbrella cloud. The phase ended with a vapour-rich, ash-poor plume detaching from the umbrella cloud and drifting westward.

Phase 4 lasted 35 minutes and consisted of a brief increase in erupted ash, followed by more vapour-rich, ash-poor venting.

Phase 5 lasted 11 minutes and consisted of a brief increase in activity resulting in weak ash columns that ascended 3.5-4 km and then spread out, detached, and drifted westward.

The key stages of the first fifteen minutes of the eruption are shown schematically in Figure 1.13.

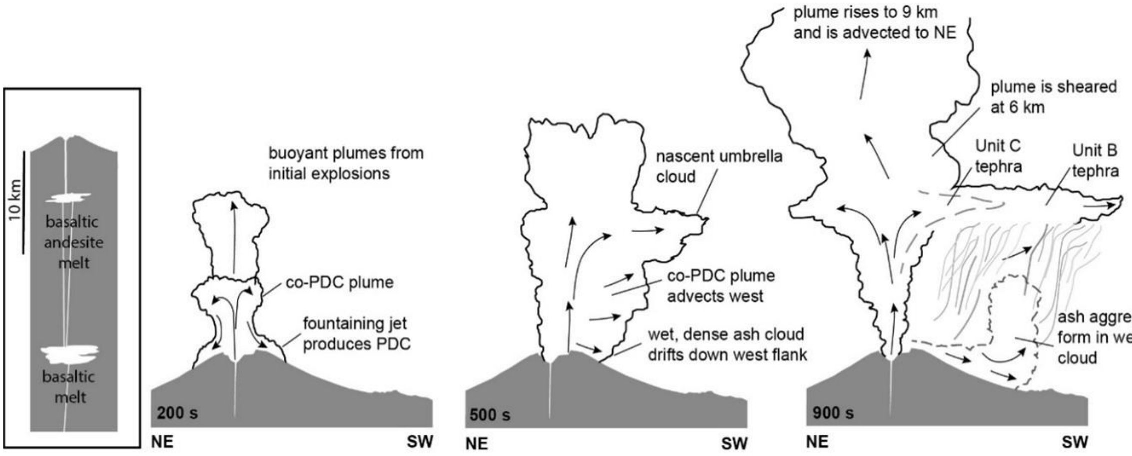

Figure 1.13. Schematic cartoons for the key stages during the first 15 minutes of the eruption. Approximate timings given in seconds. The inset on the left shows the inferred magmatic plumbing system beneath San Miguel; the eruption was triggered when hotter basaltic melt mixed with colder basaltic andesite melt in a shallow crustal magma reservoir (Brown et al., 2022).

All pyroclastic deposits on the ground are ascribed to Phase 1, including ballistic blocks and the transient PDC (Brown et al. 2022). The PDC generated a dilute, wet ash cloud that flowed down the western flanks of the volcano, depositing a thin layer of ash aggregates. At the same time, ash advected westward at altitudes of 5-6 km, and created a fall deposit. A scoria-rich fall deposit came from the main eruption column as it advected over the PDC. Since the December 29th, 2013, eruption, San Miguel has had short periods of increased minor activity (including degassing, crater landslides, steam explosions, ash emissions and elevated seismicity), but no substantial explosive eruptions (Scarlato et al., 2016; Brown eta al., 2022).

1.6 Aims and Objectives

The purpose of this study is to provide further insight and evidence into the nature of the December 29th, 2013 eruption of San Miguel volcano. Previous studies on this eruption have described and analysed the entirety of the eruption. This study aims to use additional detailed evidence from those studies and add to their findings with a comprehensive description of the tephra generated from the 2013 eruption.

Scoria, ash aggregates, and juvenile ash pyroclasts collected by R. Brown in 2014 were analyzed for morphological and textural parameters. Interpreting these parameters aids in the understanding of magma ascent and triggering mechanisms for the eruption, which may help develop a means of forecasting the onset of future potentially hazardous volcanic activity.

Each pyroclast type outlined in this study can provide the evidence needed to diagnose the 2013 eruption. Different glass types (tachylite and sideromelane) identified in scoria samples may indicate differential magma fragmentation and movement. Ash aggregates and lithic fragments can provide evidence of phreatomagmatic events. Juvenile ash particles can be used to interpret the eruptive styles. In addition to the previously noted transition in tephra deposits from lithic-rich to more juvenile-rich clasts indicating that the eruption transitioned from phreatomagmatic to magmatic.

Chapter 2: Methodology

2.1 Sample Collection

The samples used in this study were collected from San Miguel volcano between April 2-11, 2014. They represent 33 localities from on and around the volcano. Sample sites and sampling protocol are described in (Brown et al., 2022). Sampling was undertaken before the wet season to preserve both sample quality and quantity. Sample localities used for this study are depicted in Figure 2.1.

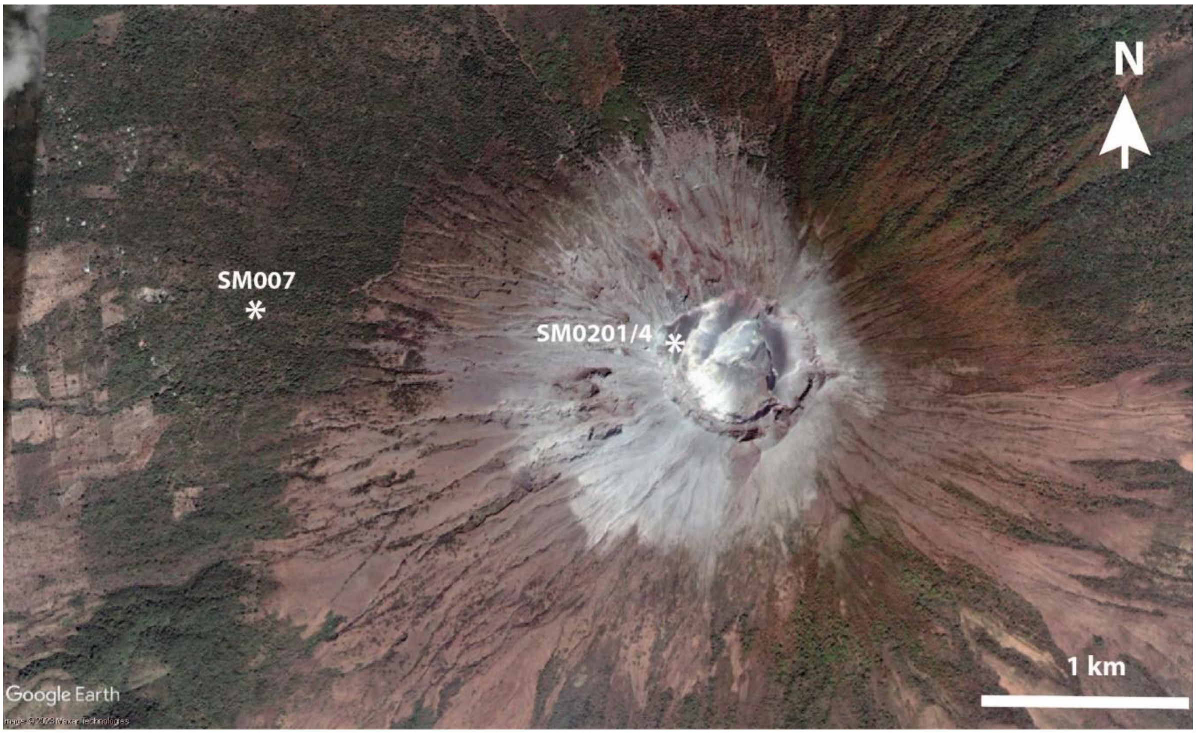

Figure 2.1. Sampled localities in and around San Miguel volcano. Image: Google Earth Pro.

2.2 Sample Selection

2.2.1 Scoria

Proximal scoria lapilli samples from the western bench in the crater (locality 020) were described macroscopically for size, shape and texture (0204, Fig. 2.2). Three representative scoria lapilli were selected for the purpose of analysing internal features such as groundmass,

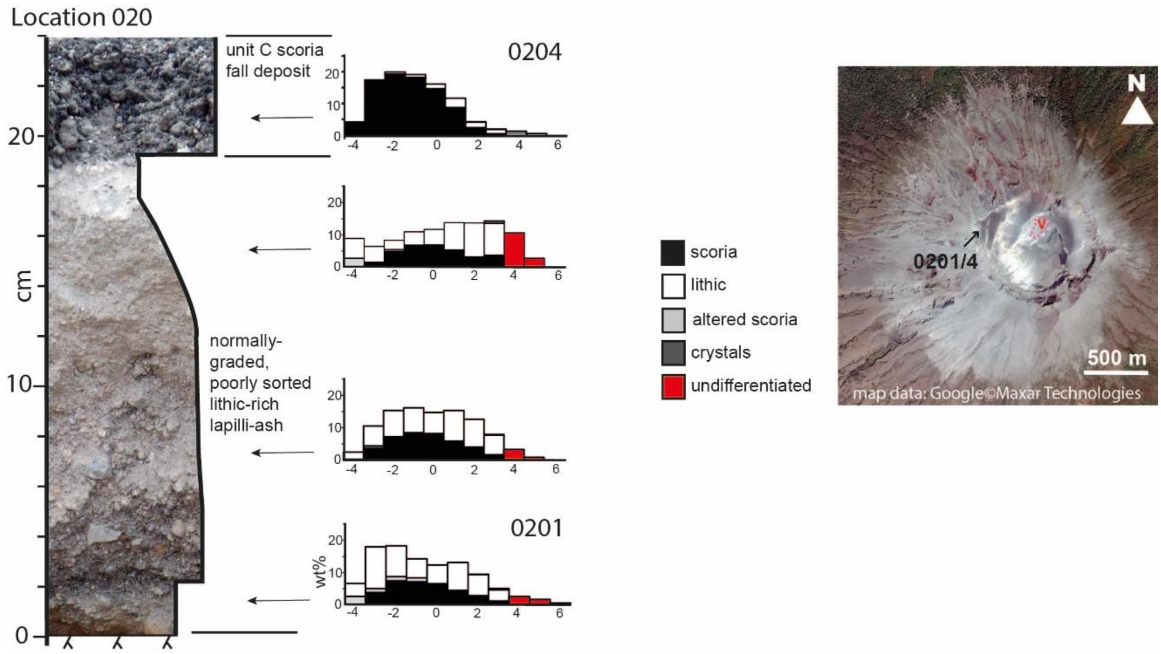

Figure 2.2 Sedimentary log and grainsize histograms showing stratigraphic position and compositional data for samples (020/1, 020/4). Modified from Brown et al., 2022.

crystals, and vesicles. Three platy scoria samples were also analysed. These samples were cleaned in distilled water in an ultrasonic bath, dried in a furnace, and made into polished thin sections for examination using backscatter SEM on a Hitachi SU-70 FEG SEM microscope located in the GJ Russell Electron Microscopy Facility at Durham University.

2.2.2 Ash Aggregates

Sixty ash aggregate samples from Unit A of the 2013 eruption (Fig. 2.3) were chosen for the purpose of analysing type, shape, internal structure and content using SEM. Twenty aggregates in each of the following sizes (1 mm, 2 mm, and 4 mm) were encased in resin and made into polished thin sections.

2.2.3 Juvenile Ash Particles

Morphometric characterisation of juvenile ash particles was undertaken on the 0.5-0.71

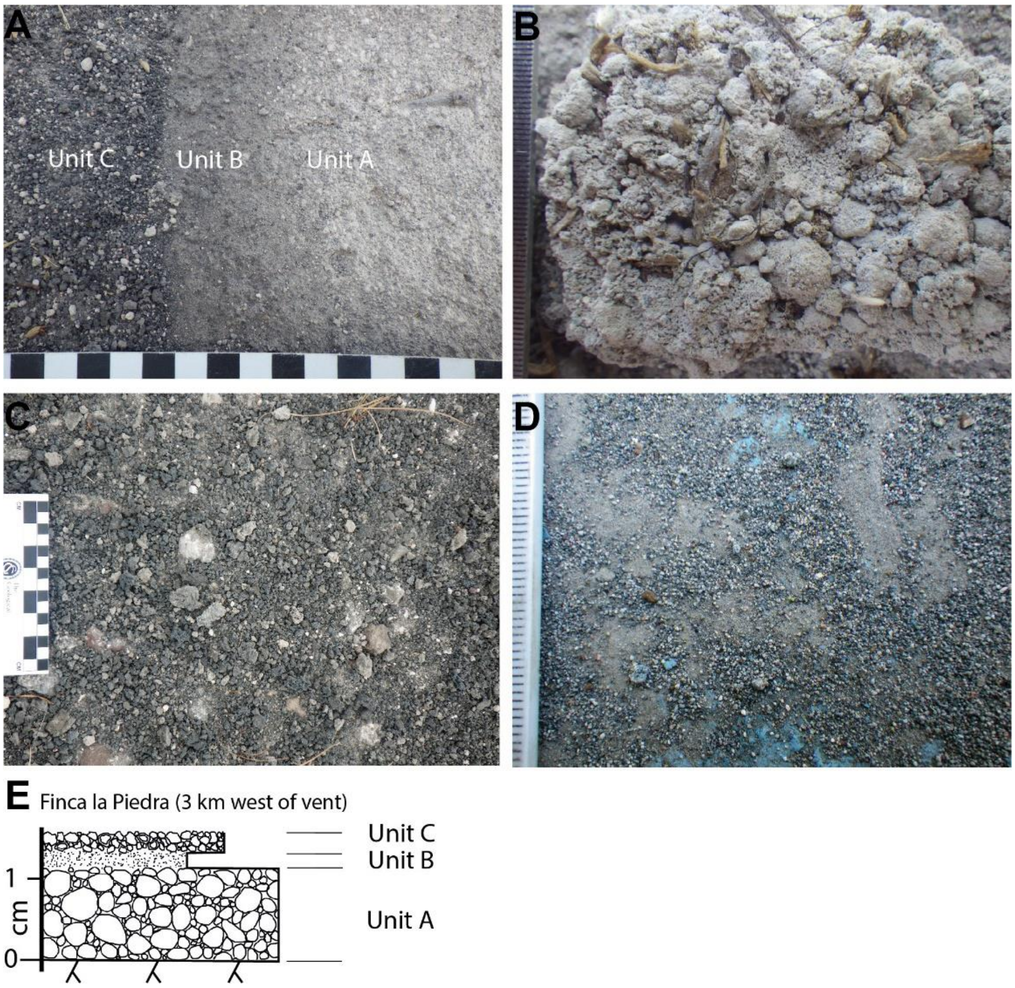

Figure 2.3. A Photo and stratigraphic log of fall deposits different layers. **B** Photo of Unit B ash aggregates, material samples are derived (from Brown et al., 2022).

mm fraction selected from tephra fall samples collected both in the crater (samples 0201 and 0204, Figure 2.3) and from a location 2.5 km west of the vent on the flanks of the volcano (SM007). This size fraction of coarse ash was concluded by Comida et al. (2021) and Ross et al. (2021) as to having the most representative textural and morphological characteristics of the erupted material. Samples 0201 and 0204 were analysed to explore variations in eruption processes during the eruption. Sample preparation followed that outlined for coarse ash by Comida et al. (2021) and Ross et al. (2021) and is outlined below (Fig. 2.4).

Samples were washed in an ultrasonic bath in distilled water 5 times at 5 minutes each to remove loose and adhering material. The water was then changed after each cycle. They were then dried in a furnace at 60 °C.

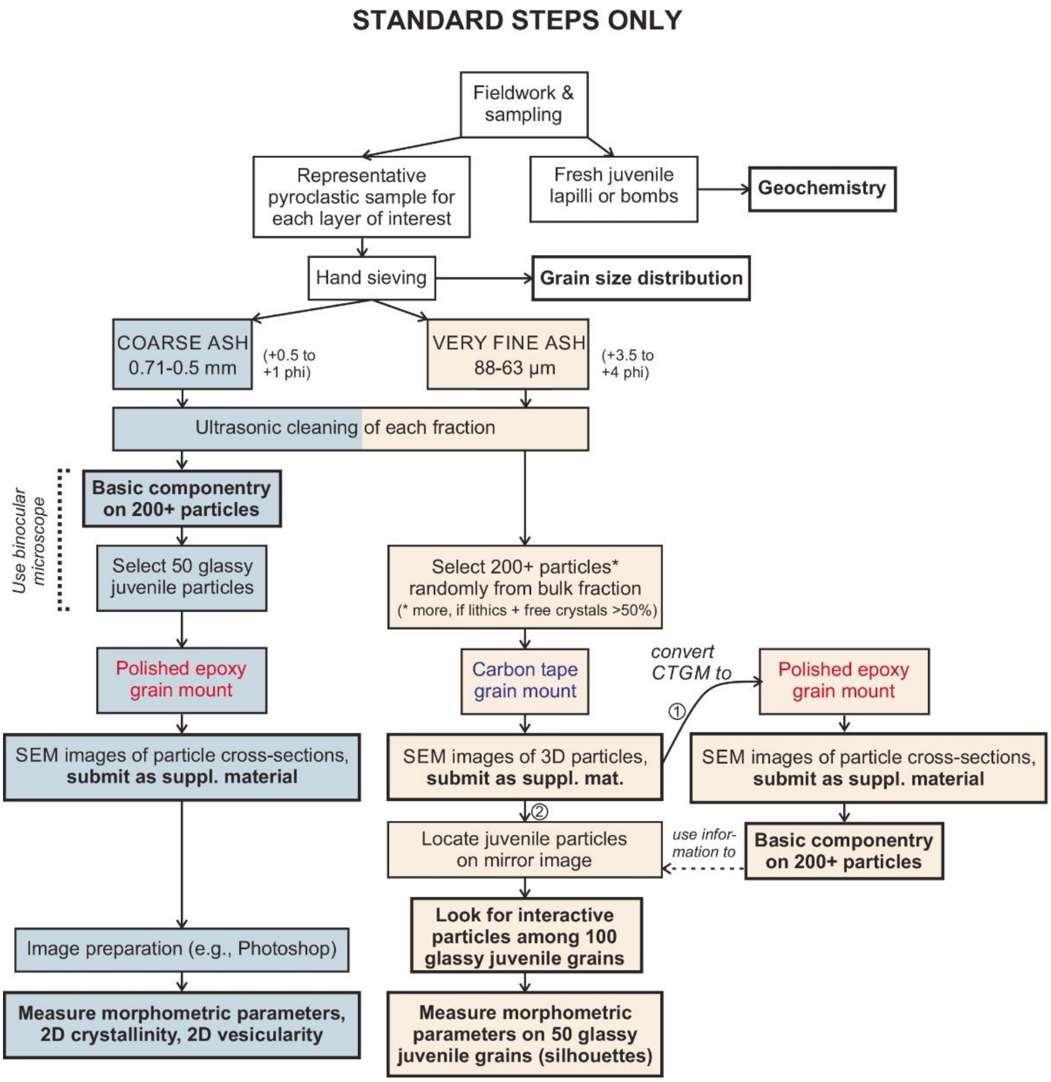

Figure 2.4. Standard steps for coarse ash characterisation (Ross et al., 2021).

Fifty glassy juvenile particles were selected under binocular microscope for each sample (Fig. 2.5). These were placed in a gridded pattern on double-sided tape. Polished epoxy grain mounts were then made for each sample, and these were polished by hand to intersect the mid-point of the selected grains. Each juvenile ash particle was imaged under the SEM. This typically resulted in 2 or more images at the magnification needed to capture the detail. Images of the juvenile ash particles were then stitched together (Fig. 2.6) and then edited and prepared in Adobe Photoshop to close open vesicles and cracks, removing debris on particle edges, trace outlines from the particle's projections, and in some instances, outline whole particles (Fig. 2.7). Particle outlines were then analysed in FIJI (Schindelin et al., 2022) using shape parameters collected by the Particle Shapes and Textures Analyzer (PASTA) plug-in developed by (Comida et al. (2021) and Ross et al. (2021).

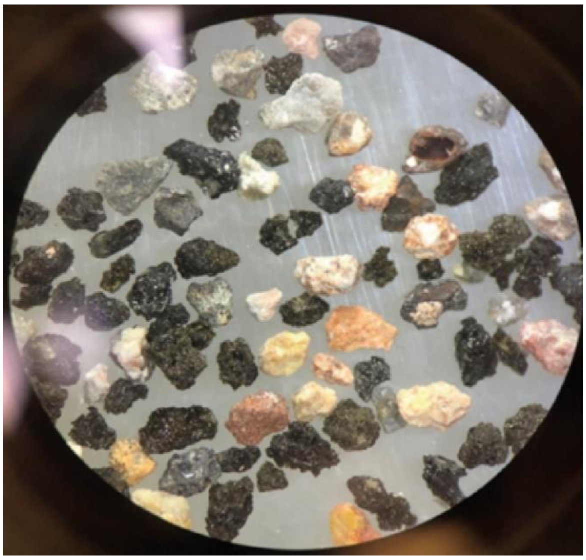

Figure 2.5. Sample 0201 under a binocular microscope showing black glassy juvenile ash particles and pale coloured lithic ash particles.

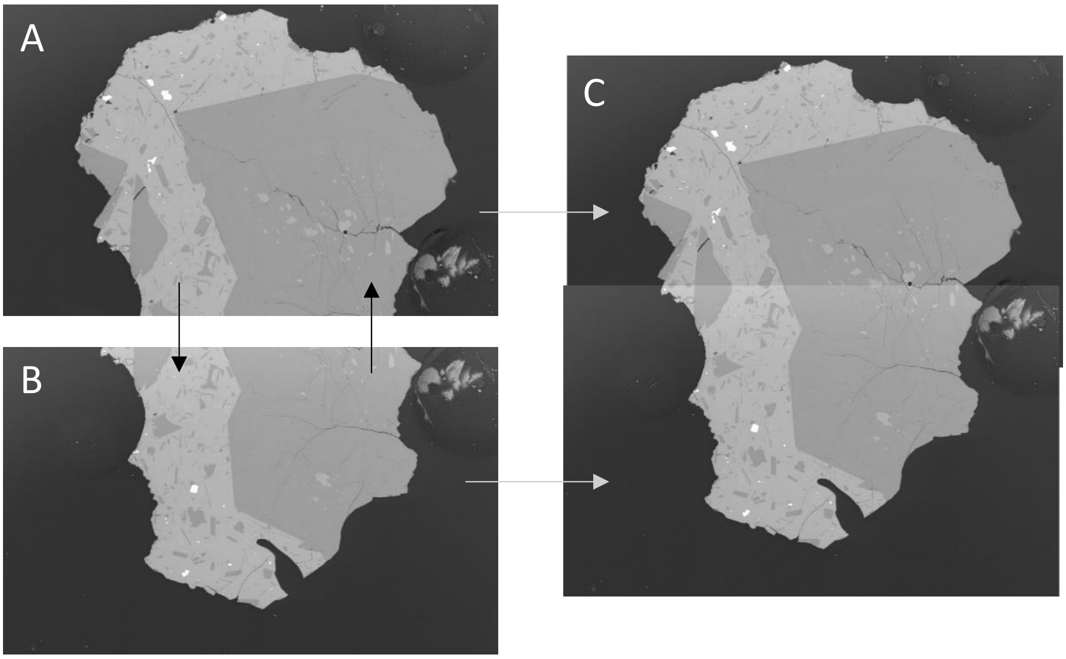

Figure 2.6 A, B Two separate SEM images of the same grain being manually stitched together for complete grain image. **C** Resulting single image of grain that was manually stitched tighter in Microsoft Photoshop.

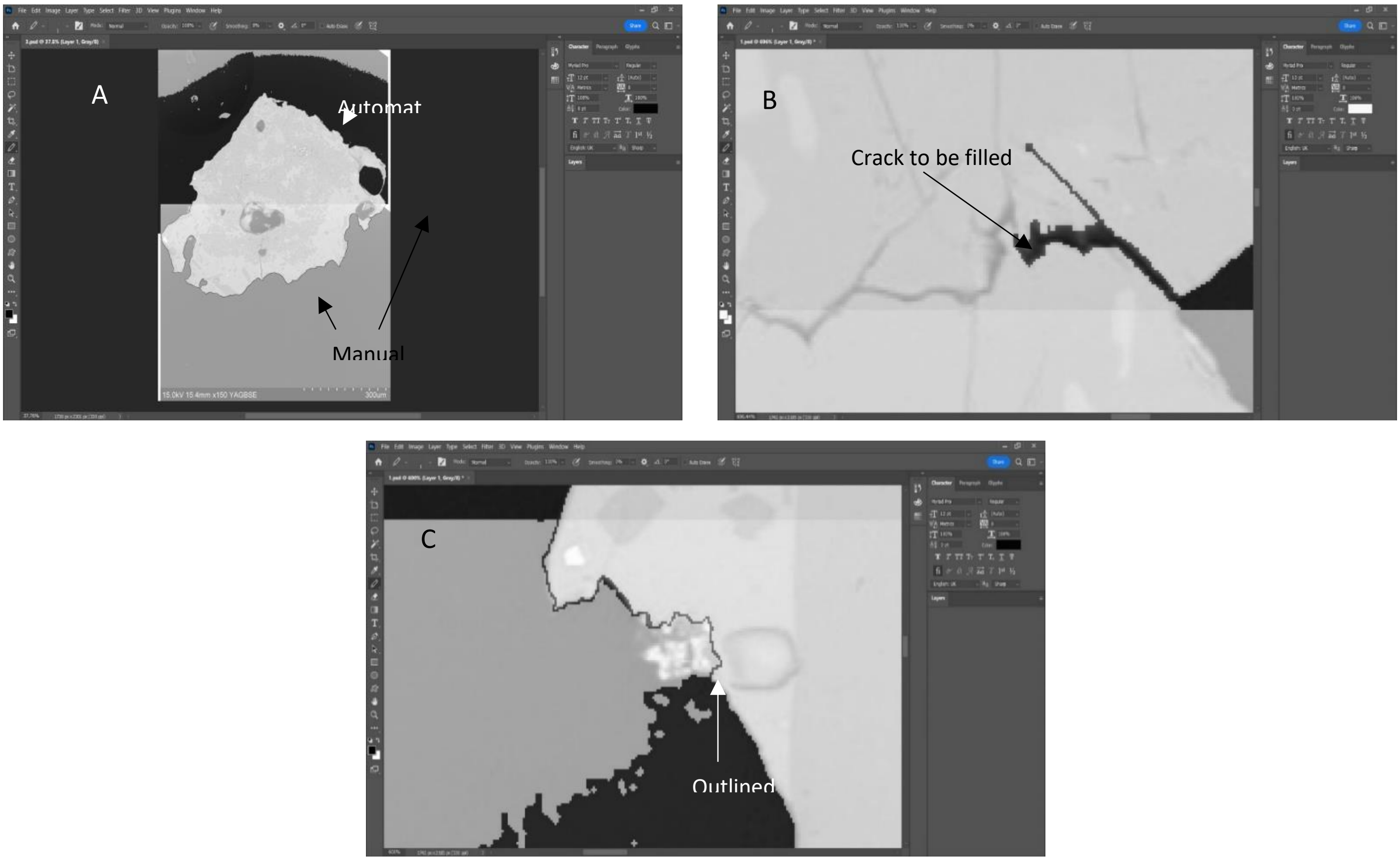

Figure 2.7. Imported images in Photoshop being manually edited after automated sequence was ran by FIJI. **A.** Image of automated outline (above) and manual outline (below). **B.** Identified crack within particle to be filled in to prevent skewed numerical results. **C.** Outline between particle and debris or projection.

These final edited images were then plugged into the PASTA plug-in. This system then generated numerical and visual shape data that were used for the comparative and diagnostic results (Figure 2.8).

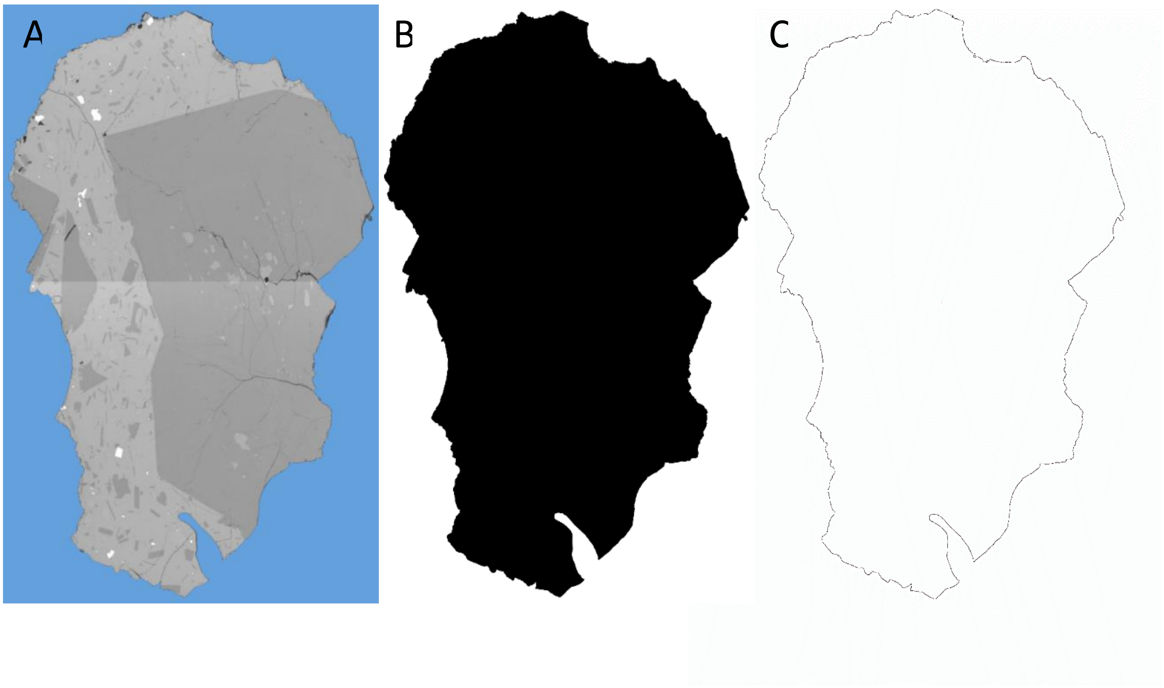

Figure 2.8. Resulting images produced from the (PASTA) program. **A.** RGB image of grain, **B.** silhouette of grain, and **C.** outline of particle.

From these results textural and morphologic features can be quantitatively observed as numeric values which include the particles morphology from its convexity, concavity, area, perimeter, axis lengths, etc. Representative 2-D shape parameter data for juvenile ash particles are as follows and are calculated from the particles outline (Figure 2.9):

A: Major axis of best-fit ellipse
B: Minor axis of best-fit ellipse
A_p: Area of the particle
A_{ch}: Area of the convex hull
P_p: Perimeter of the particle
P_{ch}: Perimeter of the convex hull

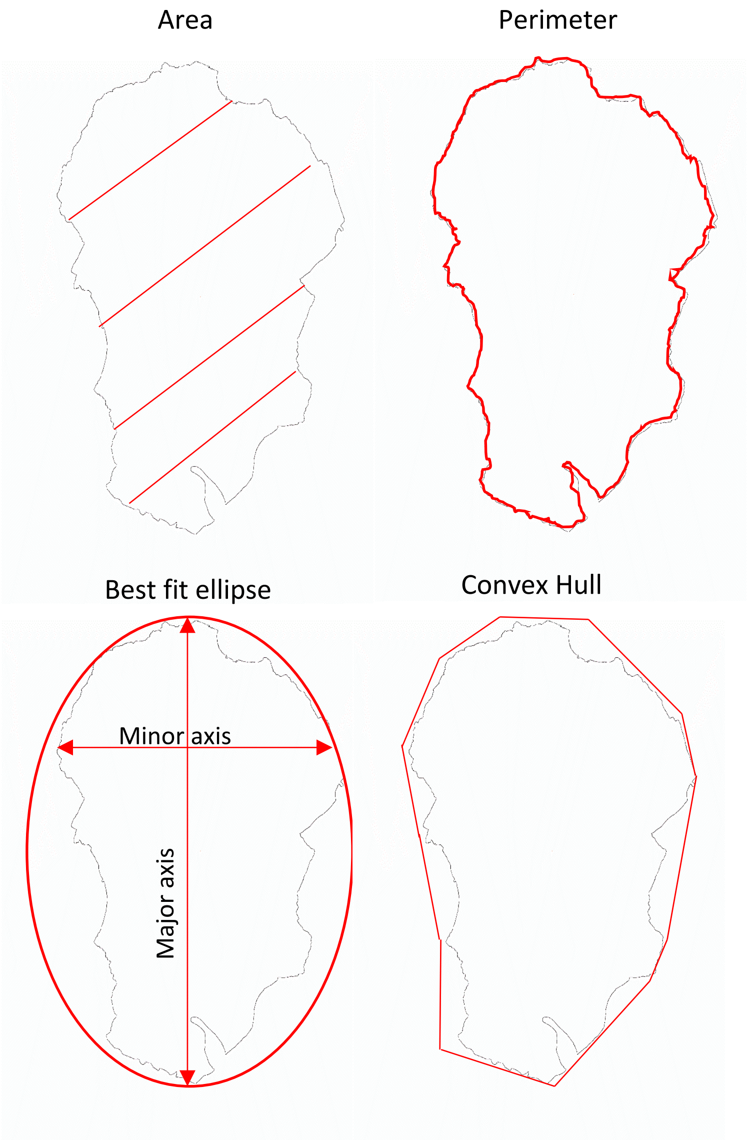

Figure 2.9. Illustration displaying how quantitative measurements are calculated from particle outlines created in PASTA.

Liu et al. (2015) used cluster analysis of ash morphological data to create equations for calculating form factor and axial ratio, which measure the particles' morphological form, and convexity and solidity, which measure the particles' morphological roughness. The equations are:

Axial ratio (AxlR): B/A
Form factor (FF): $4\pi A_p/P_p^2$
Convexity (CVX): P_{ch}/P_p
Solidity (SLD): A_p/A_{ch}

These parameters were then combined with textural and compositional information from backscattered SEM images to investigate the relationship between ash texture/composition and ash morphology for the juvenile ash particles.

Chapter 3: Results

3.1 Scoria

The dominant juvenile material produced during the 2013 San Miguel eruption was vesicular black scoria. Scoria clasts reached 10 cm in diameter, but most were in the lapilli size range. They have wrinkled and fractured surfaces and many are covered in a thin layer of white, beige or orange lithic ash and contain lithic lapilli and lithic ash particles embedded in their exteriors (Figure. 3.1 A). Scoria lapilli range in shape from equant to platy; ~ 5% exhibit extreme platy shapes (Figure. 3.1 B and C).

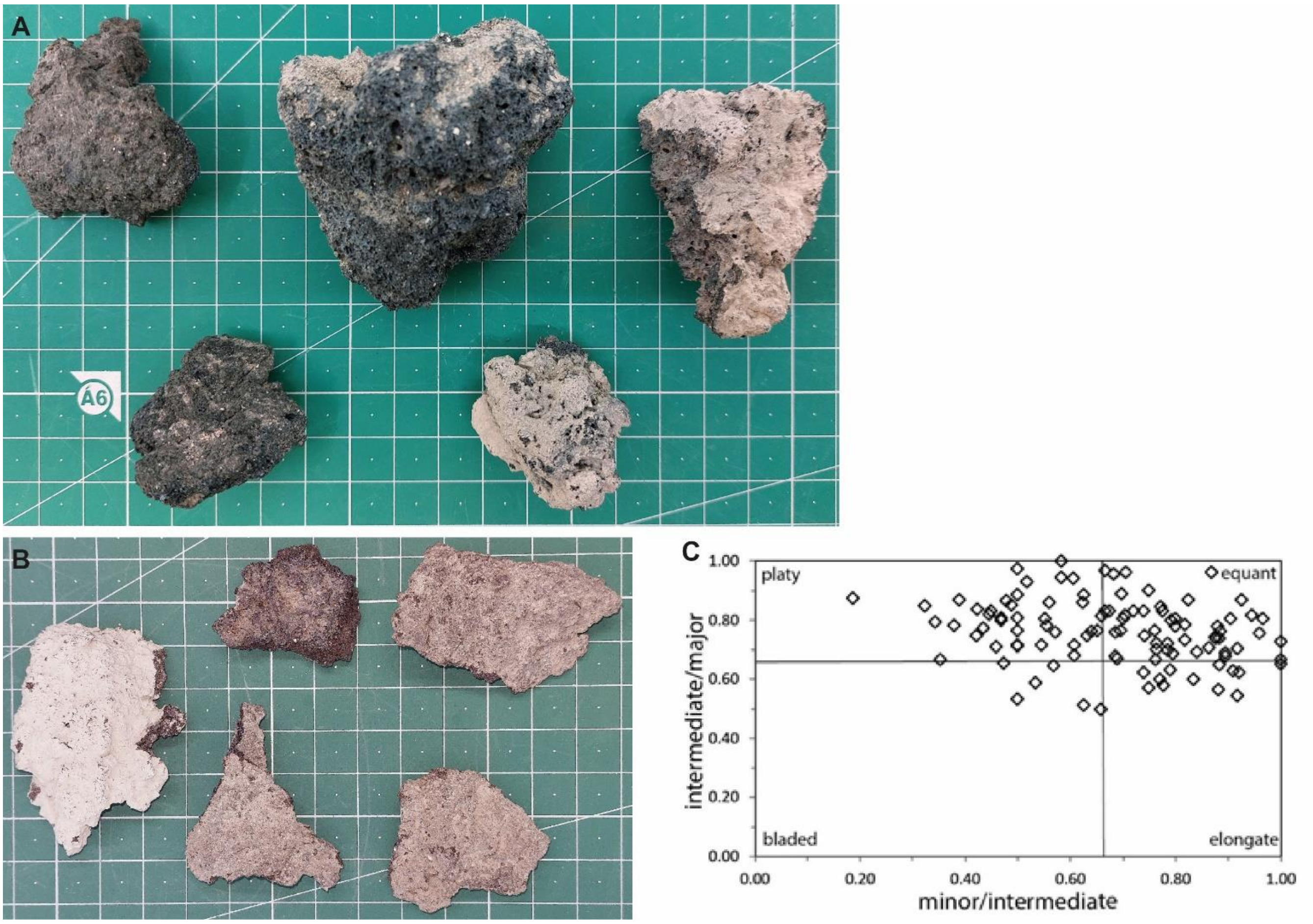

Figure 3.1. Scoria clasts. A) typical scoria lapilli showing generally equant shapes and partial lithic ash coating. B) Plate scoria with ash coating. C) Zingg plot showing 3D shapes calculated using the 3 clast axes. Most scoria clasts fall into the equant or platy fields.

Phenocrysts in the scoria samples include plagioclase (~55%), olivine (~25%), pyroxene (~15%), and oxides (<1%). Plagioclase phenocrysts are typically euhedral, 1–5 mm in length, and display zoning of cores and rims (Fig. 3.2) and some show sieve-textures in rims and slightly corroded cores. Plagioclase phenocryst shape varies with size: the smallest crystals are acicular, while larger phenocrysts exhibit more equant/tabular shapes. In addition, as size increases so does the prevalence of zoning and resorbed cores.

Olivine phenocrysts rarely display any internal structures or features. Phenocrysts are <1-3 mm in length and display euhedral to subhedral shapes (Figure. 3.2). Olivine crystals range

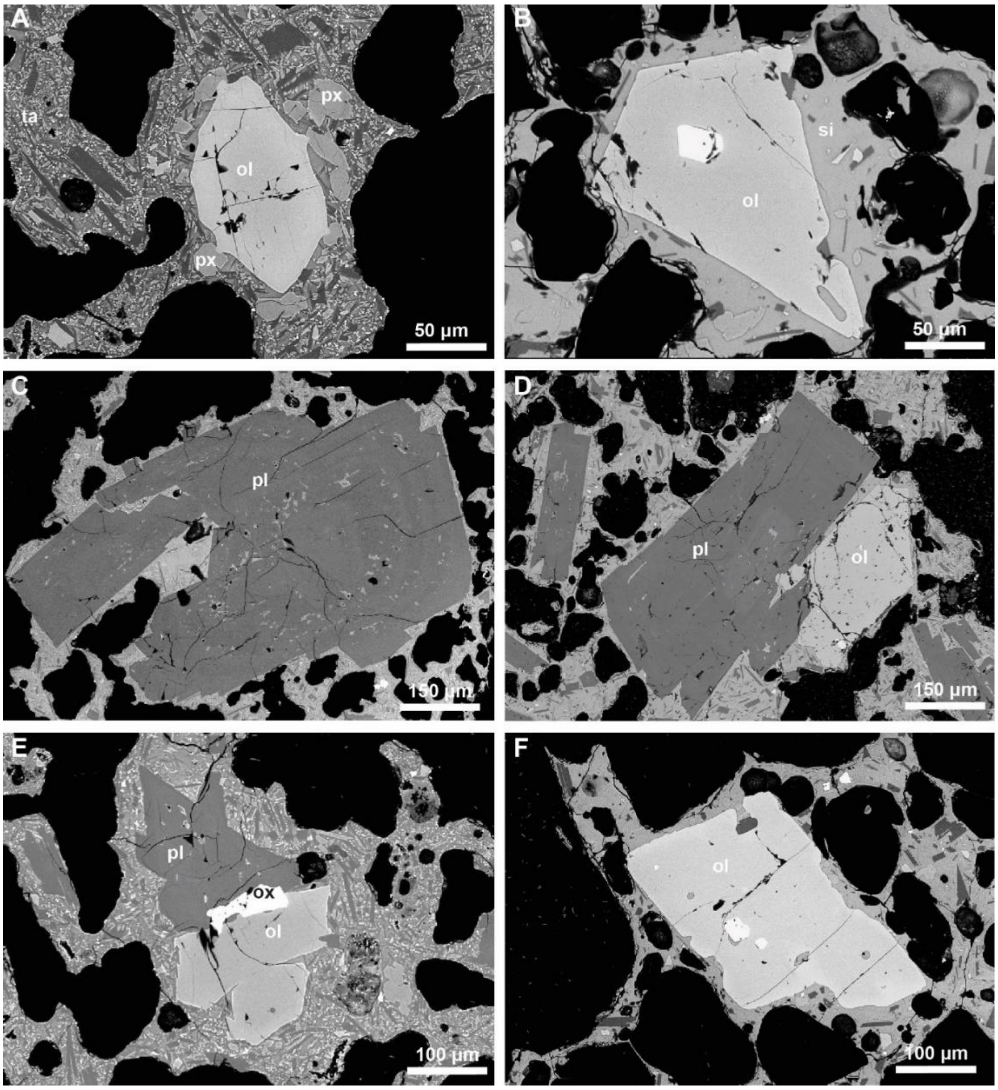

Figure 3.2. Mineral phases in the 2013 San Miguel scoria. A) olivine-pyroxene micro-glomerocryst. B) olivine micro-phenocryst with Fe-Ti oxide inclusion. C) weakly zoned plagioclase phenocryst. D and E) plagioclase-olivine glomerocryst. F) olivine phenocryst.

in size from 100–400 μm in diameter. Smaller pyroxene phenocrysts (<30 μm) are mostly anhedral, while larger, more developed phenocrysts (>30 μm) have more defined crystal boundaries.

Oxide crystals vary widely in shape from equant to angular and range in size from 5–100 μm. Oxides commonly appear in glomerocrysts and as inclusion within olivine phenocrysts. Rarely (<1% of all phenocrysts), oxides appear free of other crystals. Glomerocrysts of plagioclase, olivine, pyroxene and oxides are common and reach several millimetres in diameter (Figure. 3.2A and E).

All scoria samples are composed of domains of both hypocrystalline to holocrystalline tachylite and hypohyaline sideromelane glass (Figure. 3.3). Tachylite is characterized by abundant plagioclase, Fe oxide, olivine and pyroxene microlites. Plagioclase microlites comprise approximately 40–50% of the total groundmass. These plagioclase crystals are 1–20 μm in length. Oxide microlite crystals comprise approximately 15–20% of the total groundmass. Together, olivine and pyroxene microlites comprise 20–30% of the total groundmass. The remaining groundmass area (~5%) is glass. Vesicles in tachylite are irregular have complex shapes and many are coalesced (Figure. 3.3).

Sideromelane glass is distinguishable by a lower abundance of microlite crystals. Plagioclase microlites account for approximately 15–25% of the total sideromelane groundmass area and reach lengths of approximately 40–100 μm (Figure. 3.3). Oxide microlites comprise approximately 2–5% and tend to be larger than those in tachylite (approximately 30 μm). Olivine and pyroxene microlite crystals together comprise about 10–15%. Olivine microlites exhibit generally subhedral shapes, trending towards anhedral shapes as crystal size decreases. Pyroxene microlites are slightly larger than those in tachylite, with lengths averaging approximately 20 μm. The remaining groundmass area (about 60%) is glass. Vesicles in the sideromelane tend to be simpler and spherical to subspherical in shape

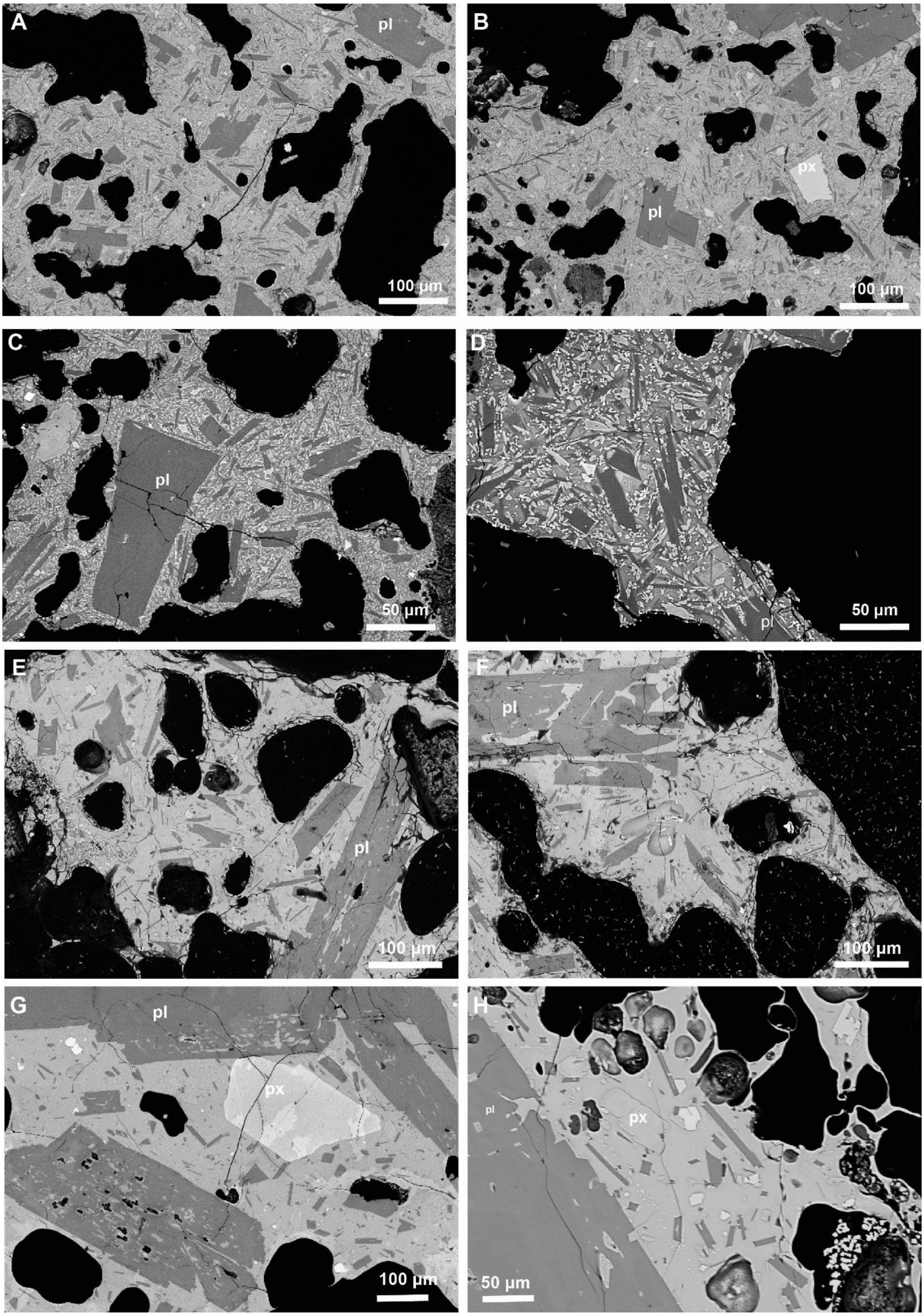

Figure 3.3. A-D) Tachylite glass in scoria clasts. Not generally irregular shape of vesicles when compared with those in sideromelane glass. E-G) Sideromelane glass in scoria clasts. Note presence of subspherical vesicles, some of which have coalesced.

and may be coalesced. Some exhibit very thin bubble walls. Many scoria clasts examined under SEM exhibit both tachylite and sideromelane groundmass. There is commonly a sharp contact between the two groundmass types (Figure. 3.4).

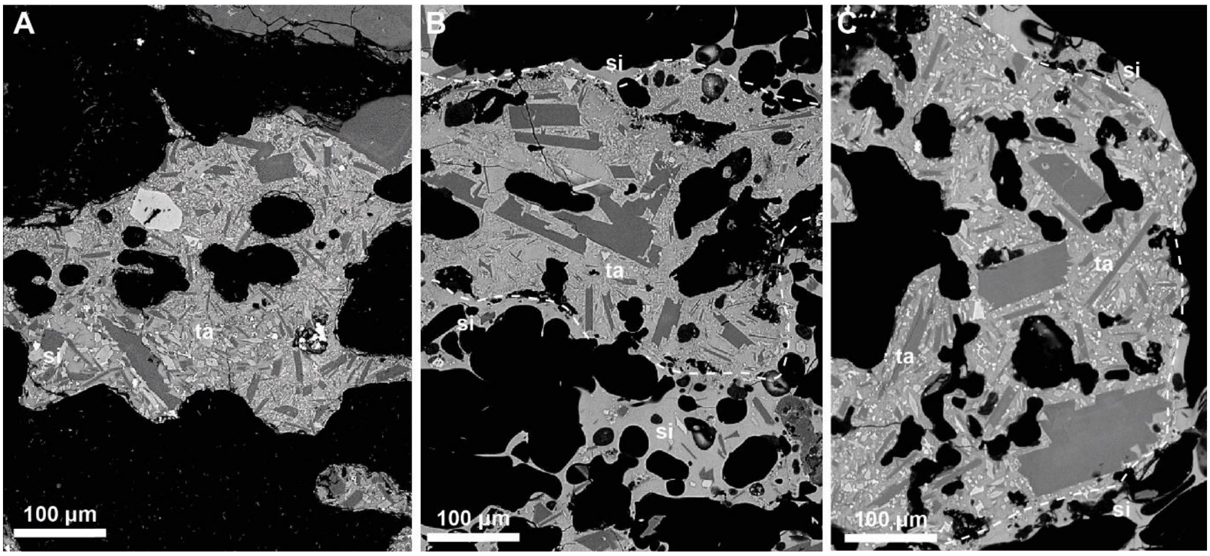

Figure 3.4. Contacts between sideromelane and tachylite glass in scoria clasts. A) Small domain of sideromelane (centre left) within tachylite. B) Irregular domain of tachylite within vesicular sideromelane. C) Sideromelane around tachylite with numerous complex-shaped vesicles.

3.1.1 Lithic Inclusions

Lithic material erupted from San Miguel includes variably altered lavas, scoria and pyroclastic rocks. Most lithic material has a white-grey colour as a result of hydrothermal alteration. Lithic material was ejected as lithic ballistic clasts (Brown et al., 2022) and composite bombs and cored bombs (Figure. 3.5). Composite bombs consisted of dense to moderately vesicular juvenile material containing 5–15 % lithic clasts, that range in size from ash to blocks (Figure. 3.5C). Cored bombs consist of a lithic block surrounded in a subspherical shell of juvenile material (Fig. 3.5A and B). In some cases, the juvenile material was broken off lithic blocks on impact (Figure. 3.5D).

Lithic material also occurs as white fine lapilli and ash particles within all scoria

Figure 3.5. Lithic-cored bombs collected in the field. A) spherical bomb with platy lithic block inside. Note the thinning of the juvenile coating around the lithic clast. B) Exterior of spherical bomb C) Composite bombs with abundant lithic clasts (white particles). D). Large lithic block with remnant juvenile rind. Photos: R Brown.

samples and accounts for about <1 % of total sample volume (Figure. 3.6). Lithic clasts range in size from 10–>1000 μm in diameter (Figure. 3.6). Lithic clasts in this study are mostly white- to tan-coloured (70–80%), with some of slightly darker shades of grey (10–15%). Fragments have a variety of shapes from angular to rounded, with the majority (60–70%) being angular to sub-angular.

Lithic ash particles are composed predominantly of altered, holo-crystalline lava and

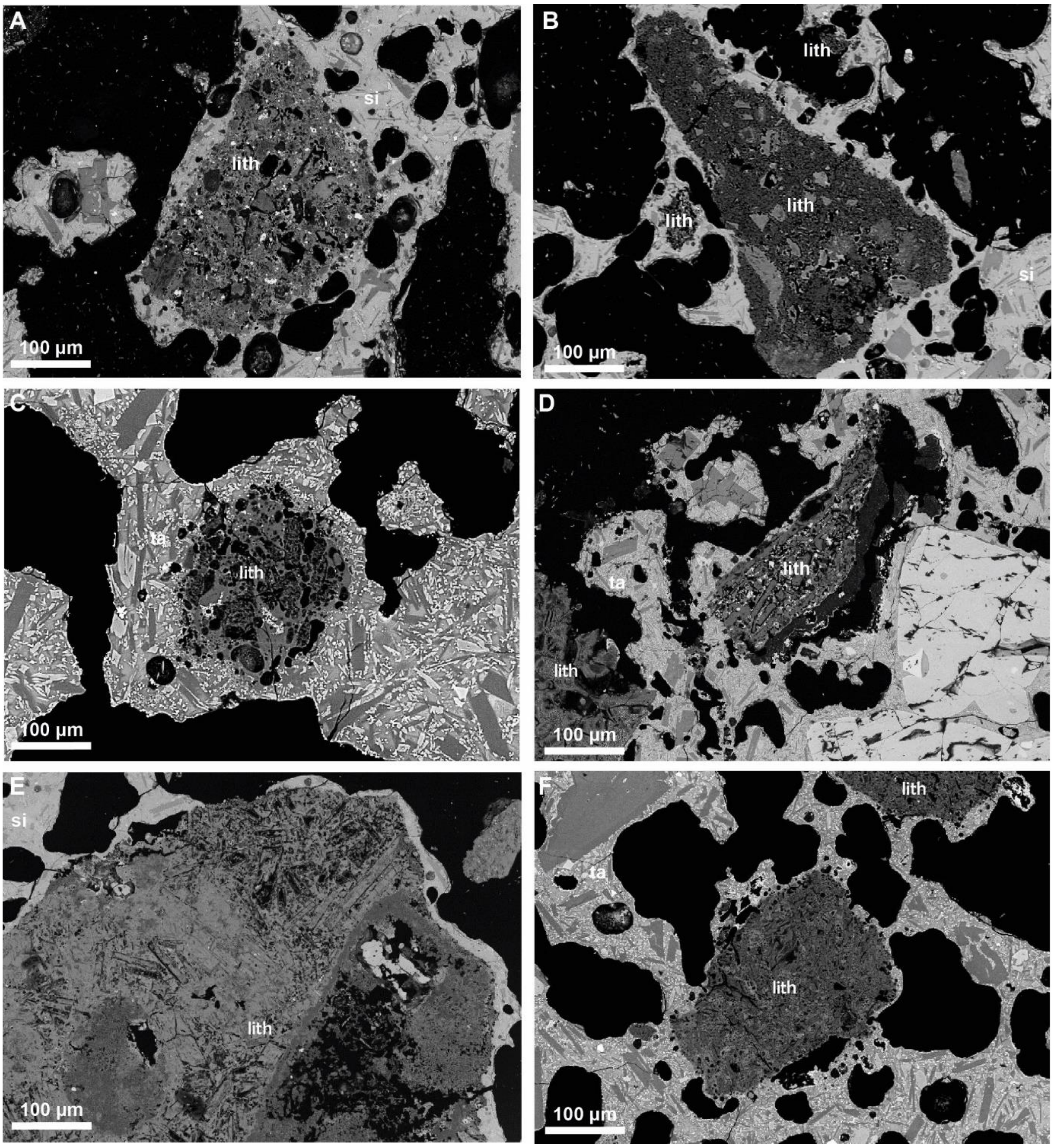

Figure 3.6. Lithic ash particles in scoria clasts. A, B) heavily altered ash particles of pyroclastic rock. C-F) heavily altered particles of crystalline lavas or scoria.

altered lithified tuff. Many are porous as a result of dissolution of crystal and glass phases. They occur within both tachylite and sideromelane glass. There is no correlation between preferred glass type and lithic abundance. Their mineralogy has not been explored.

3.2 Ash Aggregates

Ash aggregates are a common product in the tephra fall deposits of the 2013 San Miguel eruption (Brown et al., 2022). Most are present in Unit A: a narrowly-dispersed, thin layer of ash aggregates found to the west of the volcano. Unit A occurs in a number of ways in the field. In some locations it is a weakly indurated, porous, cm-thick layer of poorly sorted clast-supported aggregates (Figure. 3.7A). At other locations it is a thin layer consisting of larger aggregates in a matrix of poorly sorted ash or disaggregated aggregates (Figure, 3.7B). At locations on the margins of its dispersal it consists of loose aggregates (Figure. 3.7C). Aggregates are also present in in low abundances in the Unit C scoria fall deposit, alongside ash-coated scoria clasts (Figure. 3.7D).

Figure 3.7. Deposits of the 2013 eruption of San Miguel. A) Indurated aggregate-rich Unit A 2 km from the volcano. Deposit consists of poorly sorted aggregates and minor scoria and lithic ash particles. B) Loose aggregate rich Unit A. C) Matrix-rich Unit A with conspicuous large ash aggregates in a matrix of smaller aggregates and ash. D) distal tephra fall deposit composed of ash aggregates and scoria clasts. Photos: R Brown.

Ash aggregates are here classified using particle structure and internal lithofacies. Particle structure characterizes the particles based on major features (such as type of core and presence of concentric rims). The lithofacies describe the texture, grainsize, and porosity of the material that makes up the aggregate.

Ash aggregate bulk samples are shown in Figure 3.8. The ash aggregates can be categorized as particle clusters or accretionary pellets, following the descriptions of Brown et al. (2011) and Durant and Brown (2016). Particle clusters (PC) consist of a single clast or group clasts (where "clast" refers to one or more of either scoria or lithic clast fragments) that make up the entirety of the ash aggregate. Particle clusters are further subcategorized as ash clusters or coated particles. Ash clusters (PC1) consist of unstructured aggregates with little to no supporting matrix cementing clasts together.

Figure 3.8. Ash aggregate bulk samples. A) 2 mm size fraction of ash aggregates. B) 4 mm size fraction. C) 8 mm size fraction (with post-sieving broken fragments). D) ash-coated scoria lapilli. Note different types of aggregates in A-C. smooth surfaced, spheroidal ash pellets and irregular surfaced and more angular ash coated clasts.

Coated particles (PC2) consist of a single large clast or group of large clasts with one or more adhering rims of fine ash material. Accretionary pellets (AP) consist of a fine ash matrix (both structured and structureless) cemented together. Accretionary pellets are subcategorized as poorly structured pellets and pellets with concentric structure. Poorly structured pellets (AP1) display a fine ash matrix with no adhering rim of fine ash material. Pellets with concentric structure (AP2) display one or more adhering fine ash rims around a fine ash matrix core.

A total of 60 ash aggregates from the 2013 eruption with sizes ranging from 1-4 mm diameter were examined using a SEM. The aggregates broadly fall into three categories. 46 are classified as AP1, 6 as AP2, 8 as PC2 (3 with lithic clast cores and 5 with scoria clast cores). Smaller aggregates are varieties of AP1, AP2 and PC2, but the 4 mm aggregates examined under the SEM are almost exclusively AP1 aggregates.

3.2.1 Ash Lithofacies

The ash aggregate lithofacies were compared and classified with the aid of previous lithofacies work from (Hoult et al. 2022) who used three characteristics: porosity, grain size and particle fabric. In their study, ash particles are typically composed of fine to very fine ash. Some ash aggregates are composed of accretions of smaller ash pellets. Most are characterized by concentric layers (rims) of ash, of varying grain size, porosity, and thickness. In contrast, aggregates from the 2013 San Miguel eruption overall are less developed but do present more heterogeneous particles (Table 3.1).

The ash aggregates are composed of volcanic ash particles composed of mostly lithic clasts and juvenile clasts. Lithic ash particles present a range of igneous and volcanic textures and are inferred to be fragments of pre-existing lavas, crystals, pyroclasts and pyroclastic rocks. Many appear strongly altered and are difficult to identify. Most lithic ash particles are angular to sub-angular.

Lithofacies image	**Name**	**Description**	**Occurrence**
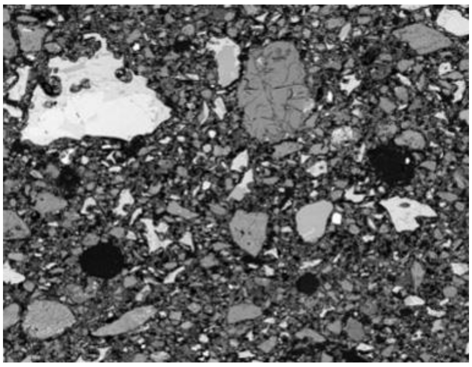	Massive, vesicular, poorly-sorted ash (MvA)	Massive, poorly sorted ash with particles up to 400 μm in diameter. Low inter-particle porosity (<10 %); isolated and sparse sub-spherical pores 30–70 μm in diameter. Exhibits little systematic variation in grainsize and no evidence for particle alignment. Grades into lithofacies mpA.	Forms the cores of some AP1 and 2 aggregates.
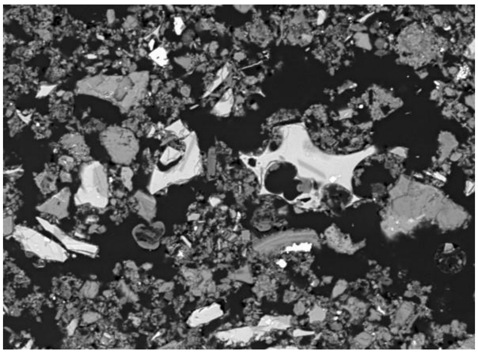	Massive, porous, poorly sorted ash (MpA)	Massive, poorly sorted ash with particles up to 400 μm in diameter. Pore space varies from 30–40 %. Pore space occurs as irregular voids, some of which are connected. Where porosity > 30 %, ash can present as PC1 clusters each 10s μm in diameter separated by irregular void space. This lithofacies may enclose <500 μm diameter PC2 aggregates (Fig. X).	Forms the cores of AP2 aggregates or as a thin rim around PC2 aggregates and lacking the large particles.
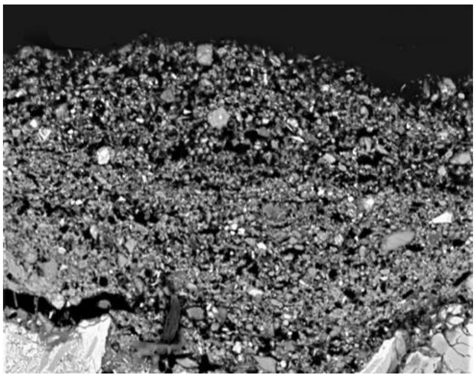	laminated fine ash (lfA)	Laminated, poorly sorted ash, composed of ash particles <50 μm in diameter. Layers, 20–100 μm thick defined by slight variations in grainsize. Porosity values of 20–30 % and most voids appear unconnected.	Presents as both the dominant internal matrix in AP1 aggregates and as <100 μm-thick rim on AP2 and PC2 aggregates.
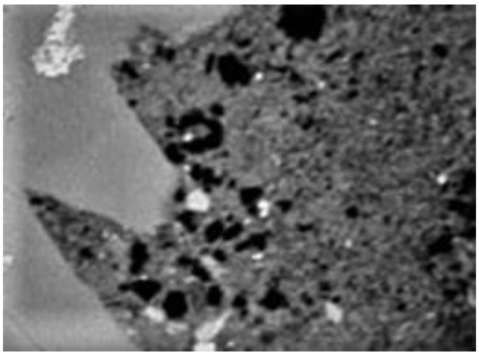	extremely fine ash (efA)	Composed of low porosity, extremely fine ash. Patchy distribution of voids and larger particles.	Occurs as a continuous to discontinuous layer around lithic or juvenile particles in PC2 aggregates.

Table 3.1. Ash lithofacies in the San Miguel ash aggregates.

Juvenile ash particles are glassy, vesicular and texturally similar to the scoria described in section 3.1. They are easily distinguished in the SEM image by their bright grey colour. The volcanic ash is composed of predominantly particles that are tens of µm in diameter. Larger clasts up to 300-400 µm are scarce. The grainsize of the ash is here classified as: extremely fine ash (E): (<5 mm); fine fine ash (M): (5 mm-30 mm); and medium fine ash (>30 mm).

Four ash lithofacies have been recognised in the 2013 ash aggregates, based on variations in porosity, texture, and grainsize, although there appears to be a gradation between the lithofacies.

3.2.2 Aggregate Types

Four main types of ash aggregates have been recognised in the deposits of the 2013 San Miguel eruption:

3.2.2.1 Particle Clusters (PC1)

Particle clusters have not been recognised as separate aggregates in the deposits, but occur within the massive porous poorly sorted ash (lithofacies MpA, Table 3.1). They are typically 10s - < 150 µm in diameter, are irregular in shape and consist of either clumps of very fine ash, or larger ash particles irregularly coated in fine ash surrounded by irregular-shaped pore space (Figure. 3.9). They are easiest to see where pore space is great and coalesce to form low porosity poorly sorted ash.

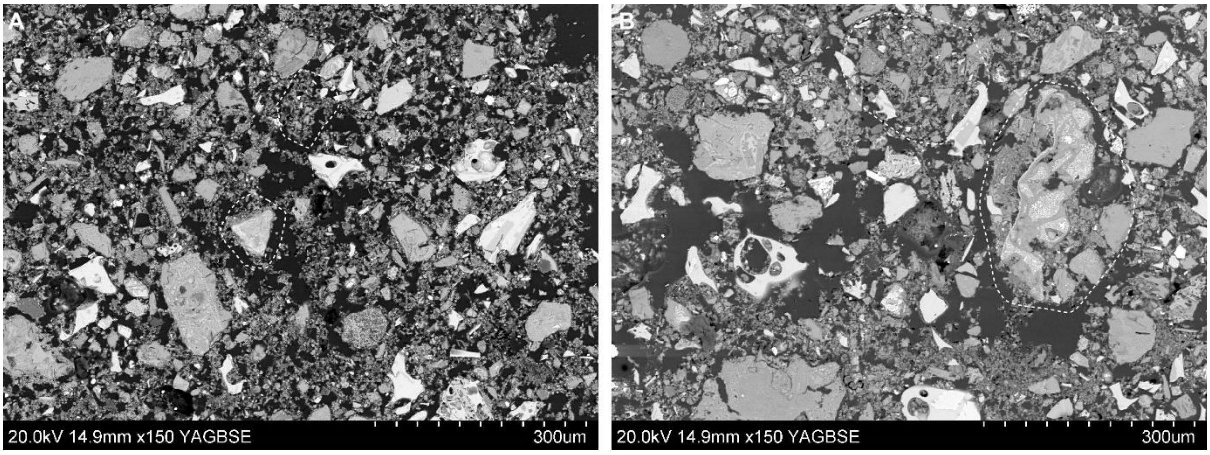

Fig. 3.9. Examples of particle clusters (PC1) in massive, vesicular, poorly sorted ash (lithofacies MvA) in the core of a AP2 aggregate. Pore space defines irregular-shaped small PC1 aggregates.

3.2.2.2 Coated Particles (PC2)

Coated particles occur as individual aggregates and within the cores of larger aggregates. They are composed of an outsized lithic or juvenile ash or fine lapilli core partially to wholly encased in a layer of finer ash particles (Figures 3.10 and 3.11). These cores typically account for >85 % of the area of the aggregate in 2D sections. Smaller coated particles (1-2 mm) typically display a single discontinuous rim of intermediate medium fine ash, whereas larger coated particles display a series of layers. Layers closest to the core are discontinuous and fill in the embayments or edges of particle’s cores. These are made up of extremely fine ash. Discontinuously around these are rims of rounded intermediate extremely fine ash.

Coated particles with a juvenile scoria clast in their centre typically show vesicles filled with ash (Figure 3.12). Vesicles that were not open to the surface of the clast lack ash filling (Figure. 3.12A and B).

One large coated particle displays two distinct rims. Similar to other (PC2) particles (e.g., Figures 3.11A and 3.11B), the outermost rim consists of an intermediate extremely fine ash facies (IE). This is preceded by a compact extremely fine ash rim (CE) that fills in the embayment of the scoria core boundary.

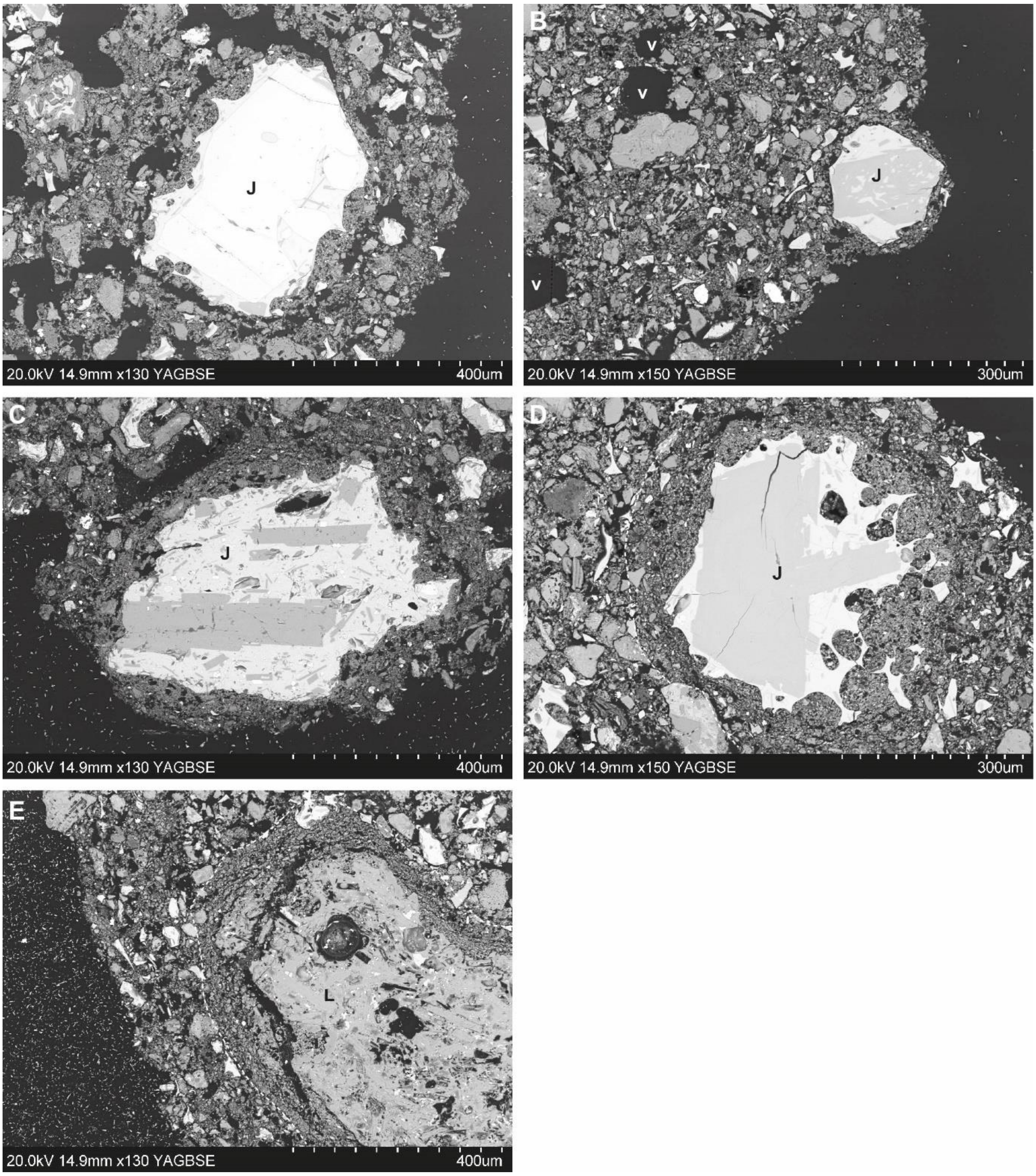

Figure 3.10. Small coated particles (PC2) within (AP1) and (AP2) aggregates. A-D) Juvenile particles surrounded by a thin layer of fine ash. PC2 in B accreted at a late stage and sticks out from the edge of the aggregate. E) lithic particle with fine ash coating within core of AP2 aggregate.

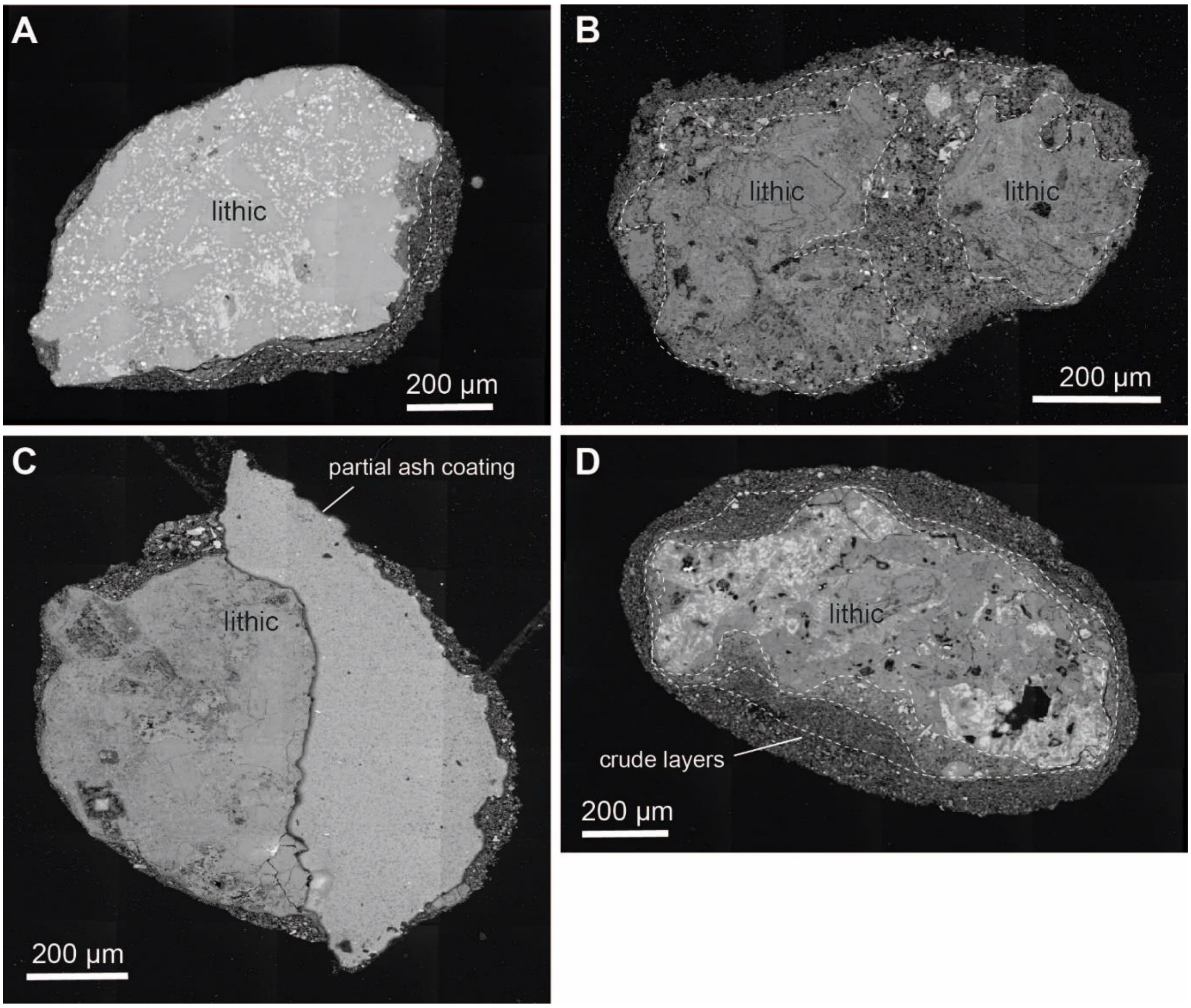

Figure 3.11. (PC2) coated particles. A) lava fragment partially surrounded in layers of ash. B) hydrothermally altered lithic particle(s) with irregular coating of ash. C) Lithic particle composed of two crystals with partial ash coating. D) hydrothermally altered lithic clast enclosed within several layers of ash.

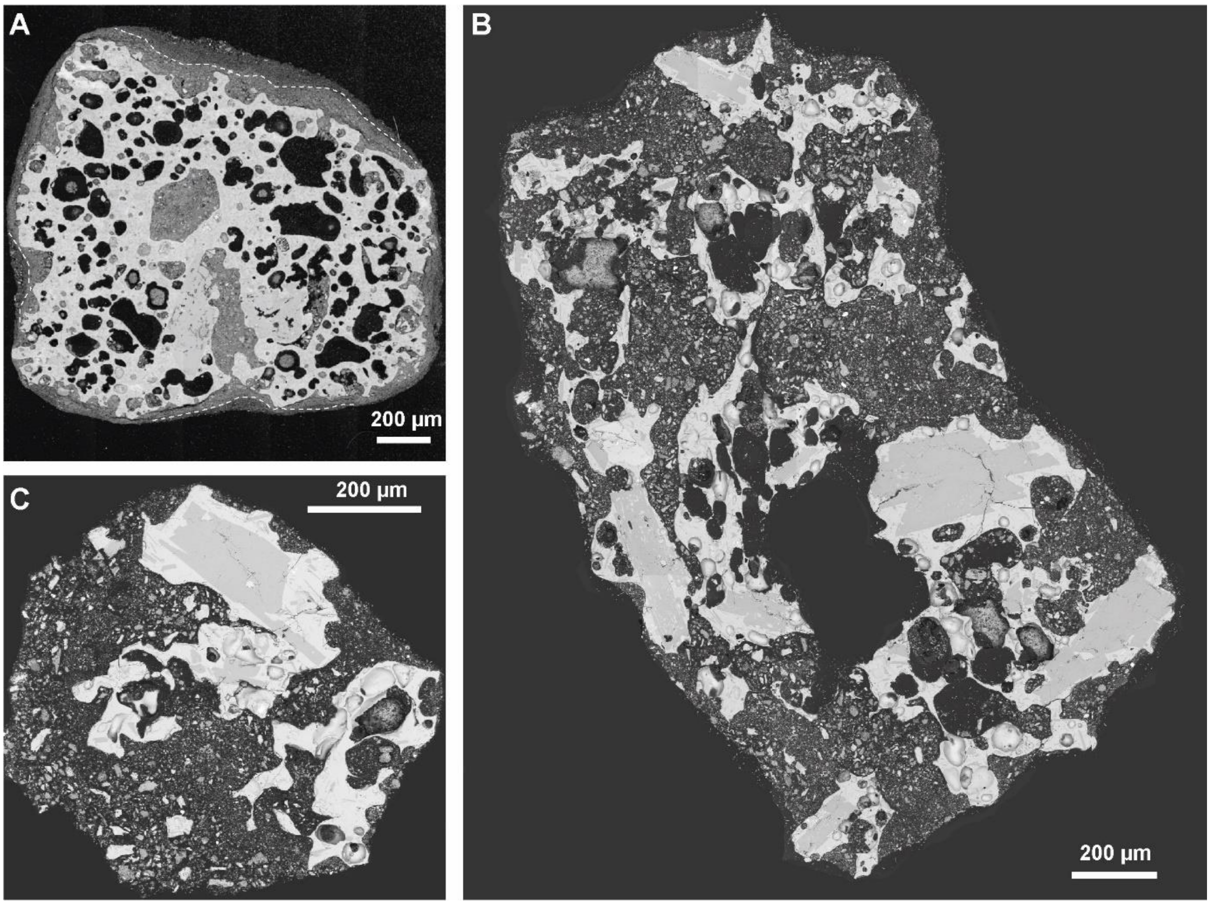

Figure 3.12. (PC2) coated juvenile particles. A). Poorly vesicular juvenile scoria particle enclosed in several layers of ash. B) Highly vesicular scoria particle with most vesicles open to the clast's exterior filled with ash. Closed vesicles in centre of clast remained empty. C). Juvenile clast enclosed in ash to form a spherical aggregate.

3.2.2.3 Ash Pellets (AP1)

Ash pellets range in size from 1-3 mm and are spherical to subspherical and are composed of massive unstructured ash (Figure. 3.13). Some contain lithic or juvenile particles up to 500 μm in diameter. Their surfaces are slightly bumpy and in some larger particles poke out from the interior. Ash pellets are composed of massive, vesicular, poorly sorted ash lithofacies (MvA, Table 3.1) or massive, porous, poorly sorted ash (MpA, Table 3.1). Vesicles are common in the ash (Figure. 3.14). These lithofacies in the AP1 aggregates commonly show weak variations in grainsize or porosity, manifested as texturally different domains 10s to 100s of μm in diameter, in which the abundance of larger ash particles varies (Figure. 3.13B).

There is a continuum between unstructured AP1 ash pellets and AP2 accretionary pellets with distinct finer-grained rims.

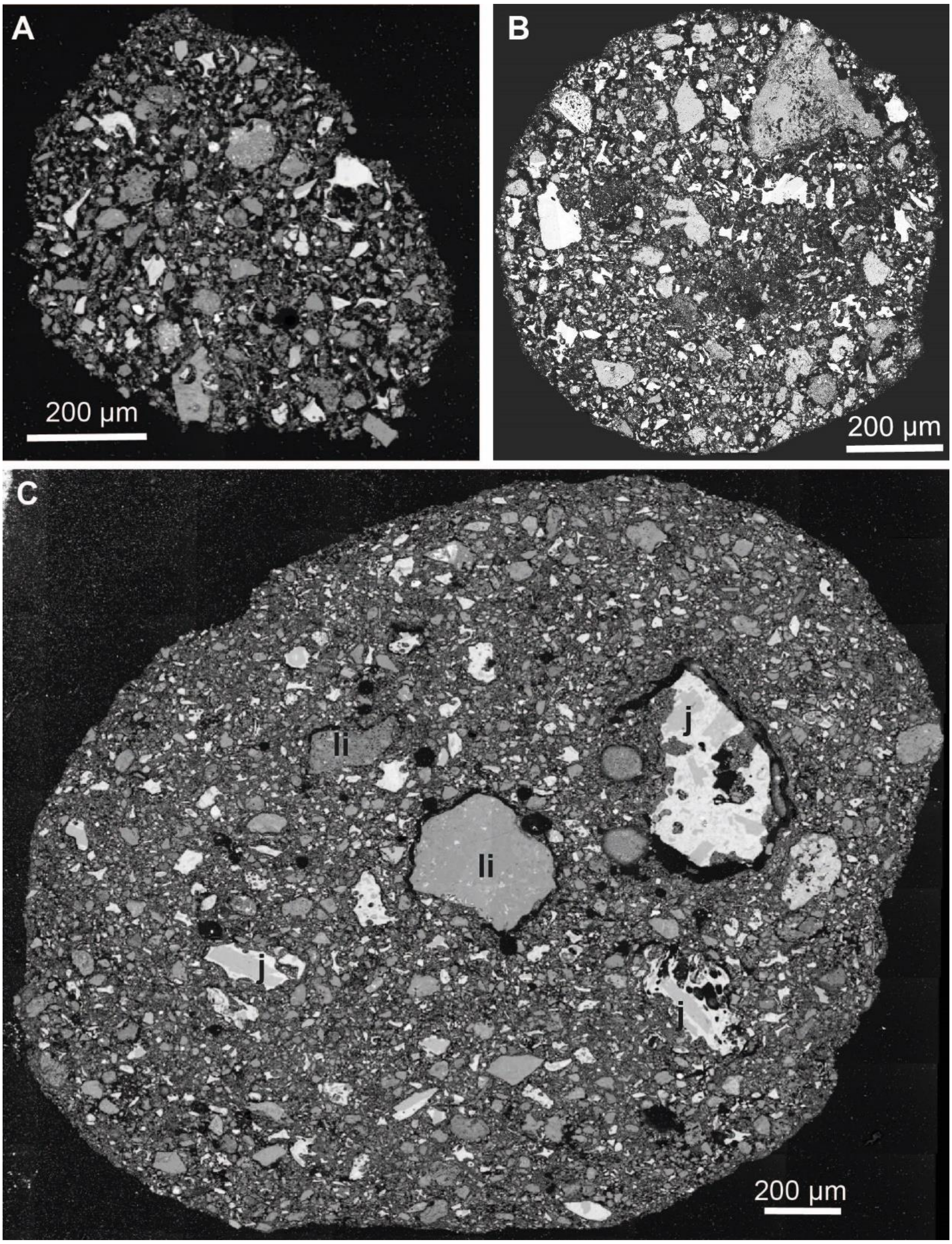

Figure 3.13. (AP1) ash pellet aggregates. A, B) small subspherical pellets. C) larger pellet with several outsized ash particles.

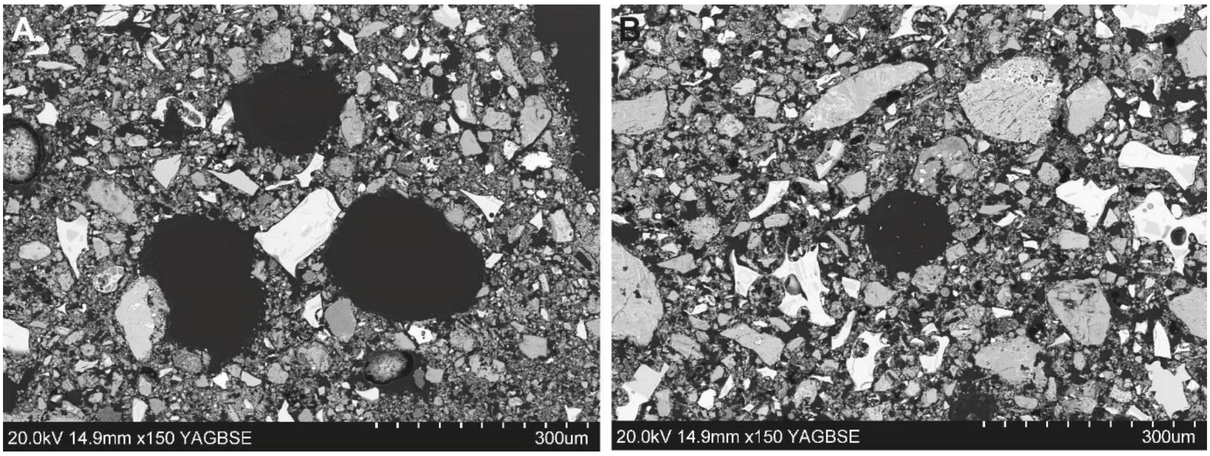

Figure 3.14. Subspherical vesicles in massive, vesicular, poorly sorted ash (MvA) in AP1 aggregates.

3.2.2.4 Accretionary Pellets (AP2)

Accretionary pellets are distinguished from ash pellets by the presence of one or more outer concentric rims of finer-grained ash (Figure. 3.15). Core lithofacies from the samples are mostly massive, vesicular, poorly sorted ash (MvA) or massive, porous, poorly sorted ash (MpA, Table 3.1). Rim lithofacies are composed of laminated, porous fine ash (lfA, Table 3.1). The cores may display a heterogeneous distribution of coarser particles and vesicles, and typically account for 90 % of the area of an aggregate in 2D. The rims are typically < 100 μm thick and thicken and thin around the aggregate. In most aggregates there is a sharp boundary between the core and the rim, but in a few the boundary is gradational and marked by normal outward grading. Platy particles in the rims show a weak concentric alignment.

3.3 Ash Particle Characterisation

3.3.1 Particle Texture and Composition

One hundred and fifty particles in the size range 0.5-0.71 mm were taken from three samples (50 particles each from the initial explosion deposit 0201, scoria fall deposit 0204, and distal ash SM007C) and analysed for particle morphology. Juvenile ash particles were classified based on texture and composition as melt-coated crystals or glassy particles.

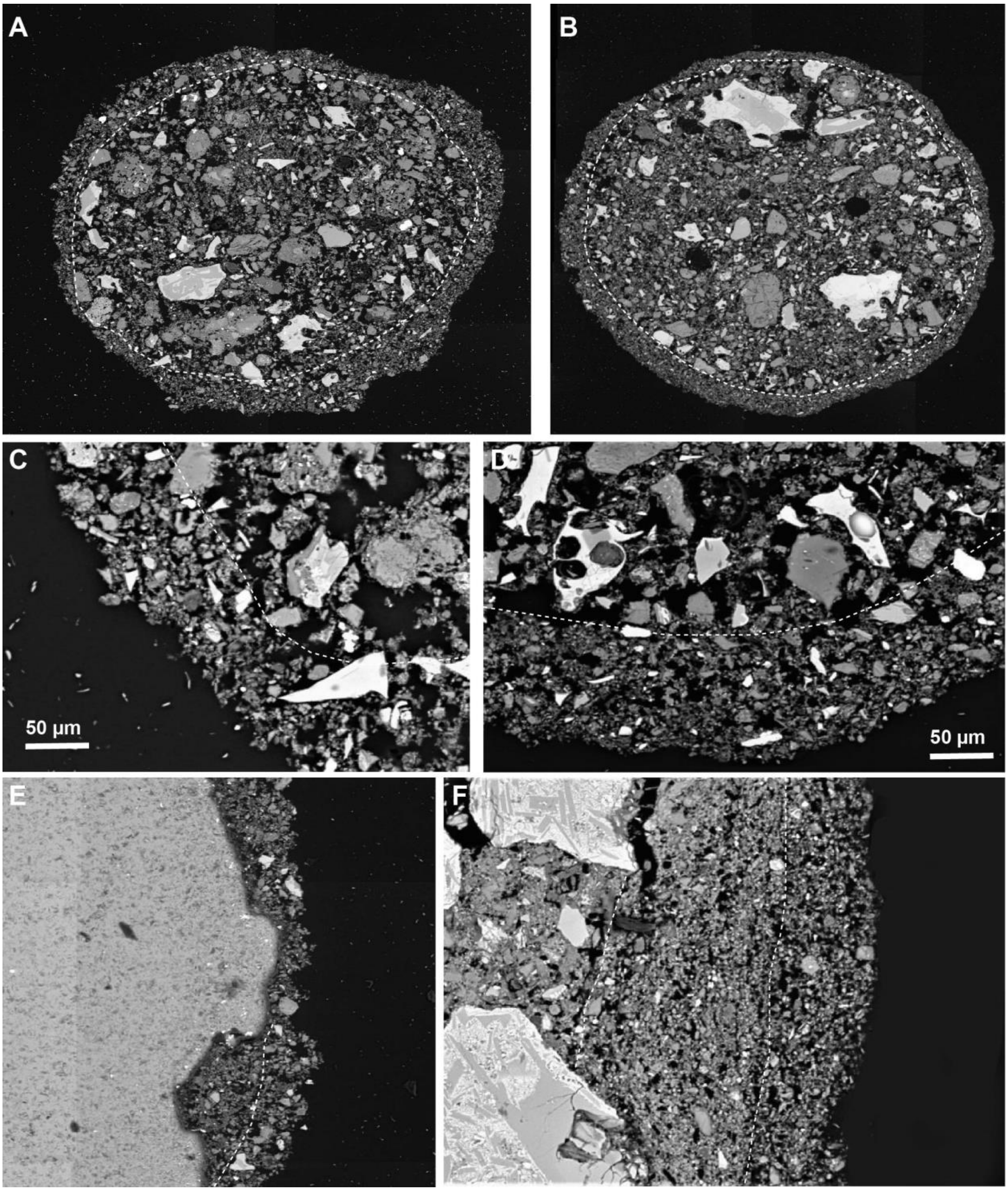

Figure 3.15. AP2 accretionary pellets. A, B) small accretionary pellets with one well developed finer-grained rim. C, D) details of rims in A, B. E) poorly developed rims on a coated particle. F) well developed rims around a coated particle.

This classification is based on the approximate overall percentage of the dominant composition and texture. In the case of melt coated crystal particles, a single crystal (rather than the sum of all crystals) had to be the majority feature (Figure 3.16).

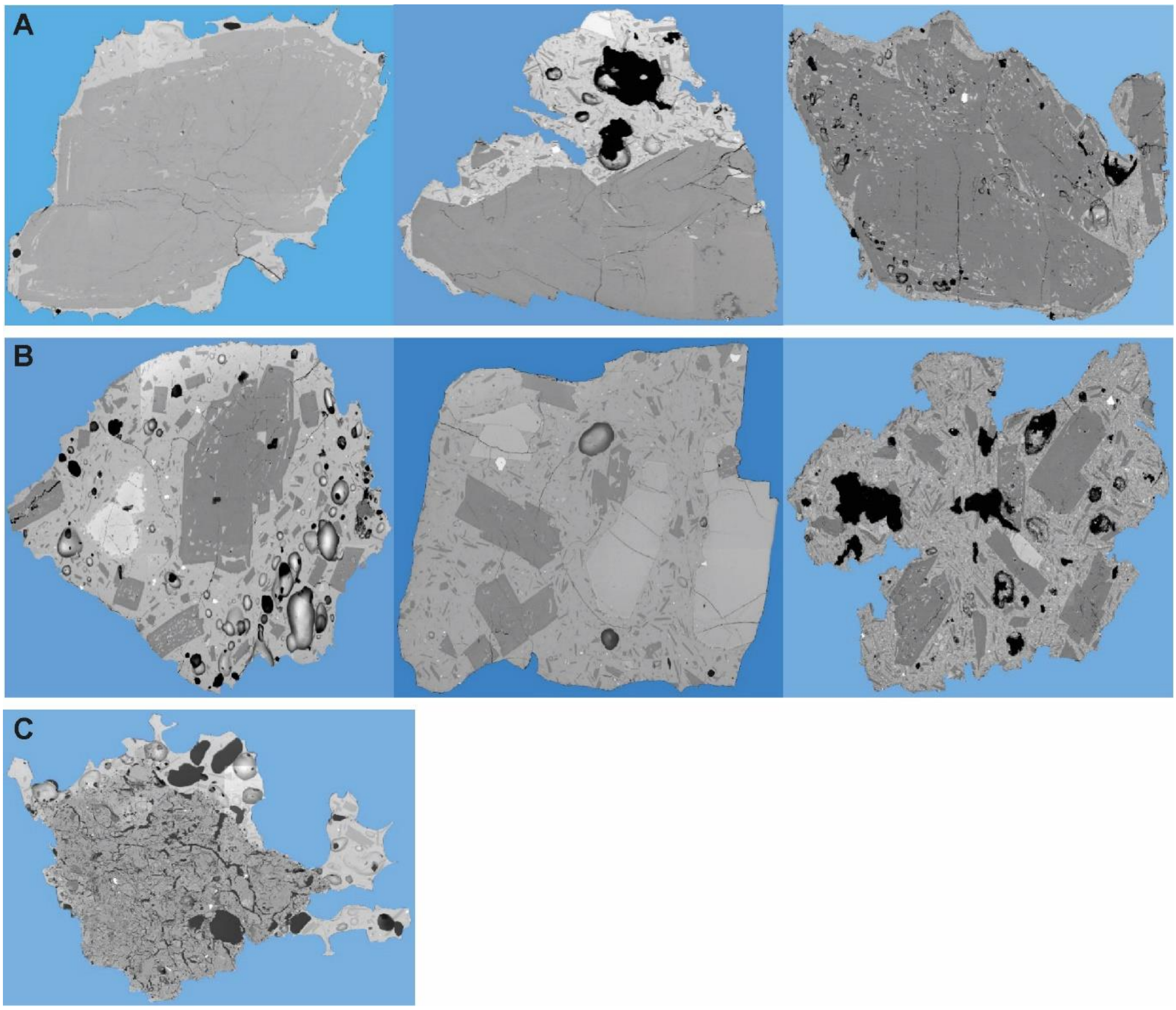

Figure 3.16. Images of particle types; A: melt-coated crystals, B: glassy particle and C: melt coated lithic.

The ash particles are classified into the following categories. Sample 0201 contained 32% melt-coated crystals and 68% glassy. Sample 0204 contained 28% melt-coated crystals and 72% glassy particles. Sample SM007C contained 26% melt coated crystals particles and 74% glassy particles. Sample 0201 had one particle that was the exception; this particle was classified as a lithic dominate particle (Fig. 16C). This particle is not a lithic particle, but rather a lithic clast set in glass. Therefore, this can be ignored for representative data.

The juvenile ash particle exhibit both sideromelane and tachylite glass (Figure. 3.17 A and B). Vesicles in the tachylite glass are irregular and exhibit a wide size range. In some tachylite glass the texture approaches diktytaxitic with numerous small irregular vesicles in a crystal-

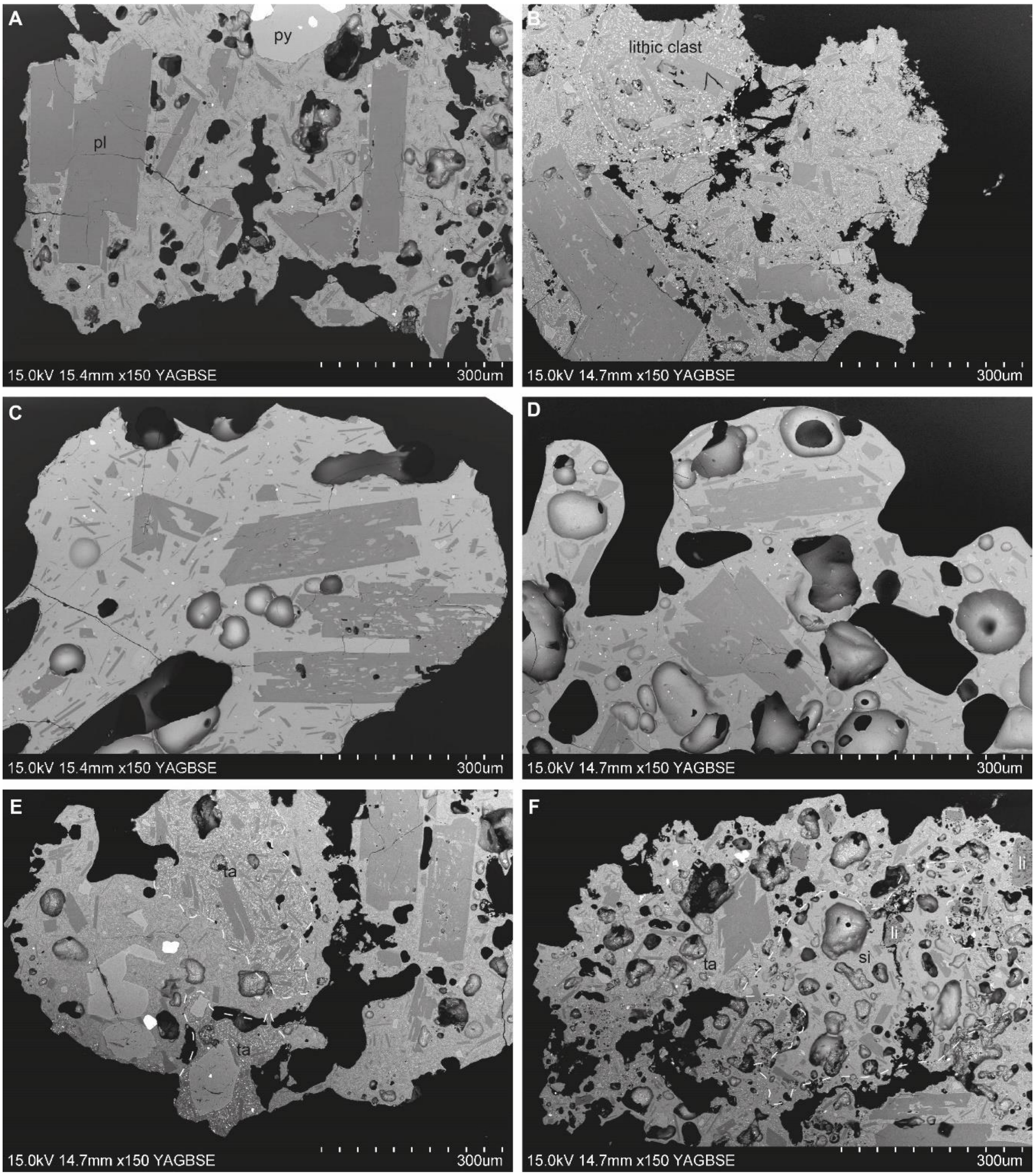

Figure 3.17. Groundmass textures in juvenile ash particles. A, B) tachylite glass with irregular vesicles and diktytaxitic voids (B). Note lithic clast in upper half of B. C,D) Sideromelane glass with relatively low microlite contents.

rich groundmass. Sideromelane glass is relatively crystal poor (see section on scoria clasts) and vesicles are subspherical to equant and have a narrower size range than those in tachylite groundmass. A few volcanic ash particles exhibit irregular domains of tachylite and sideromelane groundmass (Figure. 3.17 E and F), or notable variations in groundmass crystallinity on the order of 100s of μm (Figure. 3.17 C and D).

Angular lithic ash particles < 200 μm in diameter are present embedded within some juvenile ash particles (Figure. 3.17 B an F).

The edges of the juvenile ash particles show evidence for brittle (fractured) and plastic deformation during fragmentation (Figure. 3.18). Fractured surfaces vary from straight to curvi-planar and irregular and cut across crystals and vesicles. Surfaces that underwent plastic deformation are smooth and do not cut across crystals or vesicles. Instead, they show smooth bulbous exteriors and evidence for fluid retraction of bubble walls and surface tension effects around crystals (Figure. 3.19). Some juvenile ash particles show evidence for both brittle and plastic deformation on fragmentation (Figure. 3.18 A and D).

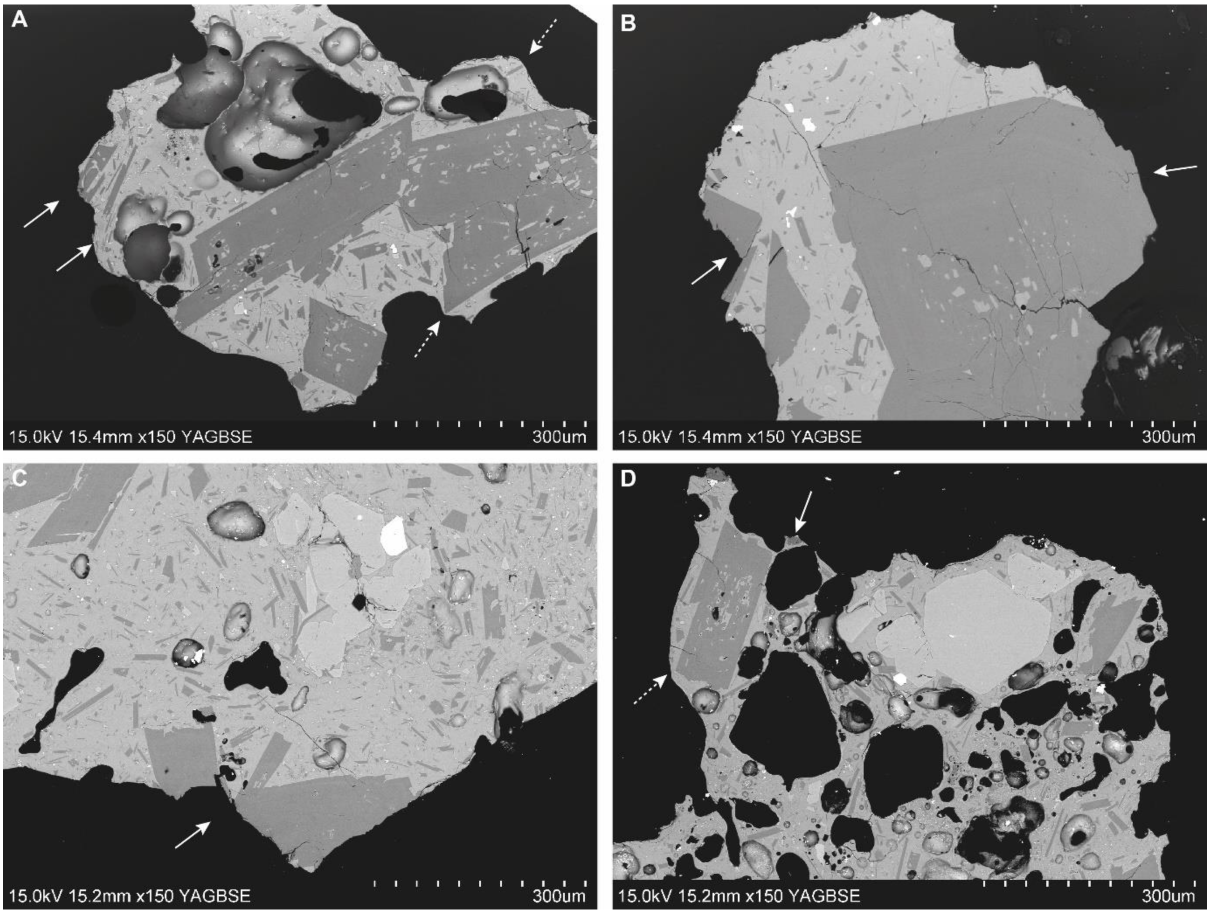

Figure 3.18. Examples of fractured surfaces to volcanic ash particles. Solid arrows indicate crystals broken by fractures. Dotted arrows point to exteriors that have undergone plastic deformation (B, D).

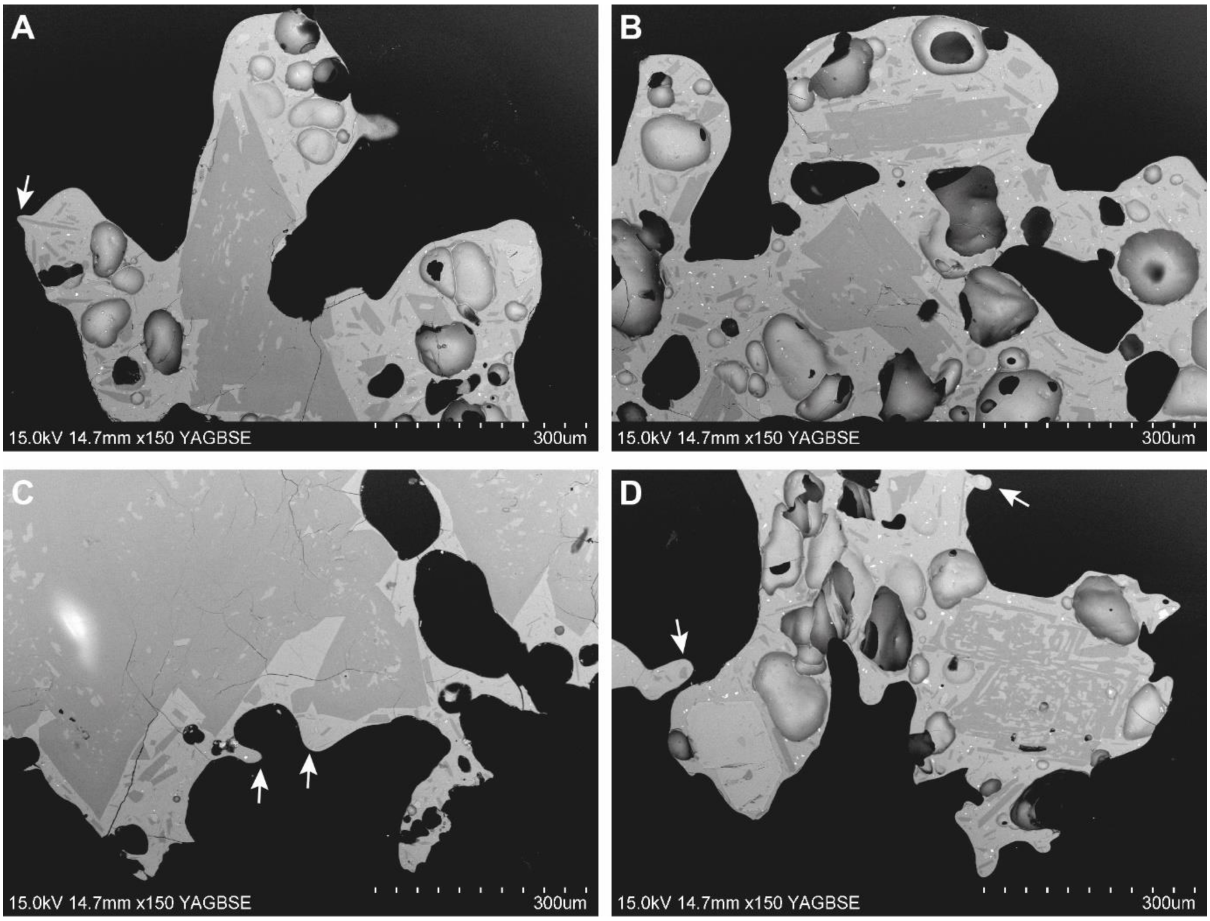

Figure 3.19. Evidence for plastic deformation of juvenile ash particles, including retraction of filaments and vesicle walls and smooth bulbous exteriors.

3.3.2 Particle Morphological Form

The mean axial ratio and form factor of each sample is given in Table 3.2. The higher the values, the more equant the particle; the lower the value, the more elongated the particle (Figures 3.20 and 3.21). The axial ratio in sample 0201 ranges from 0.087 - 0.582, the axial ratio in sample 0204 ranges from .084 - .458, the axial ratio in sample SM007C ranges from 0.053 - 0.483. The form factor in sample 0201 ranges from 0.292 - 0.958, the form factor in sample 0204 ranges from 0.375 - 0.958, the form factor in sample SM007C ranges from 0.298 - .0964.

Sample	Mean axial ratio	Mean form factor
0201	0.63	0.25
0204	0.66	0.22
SM007C	0.62	0.21
mean	0.63	0.23

Table 3.2. Mean axial ratio and form factor values of juvenile ash particles.

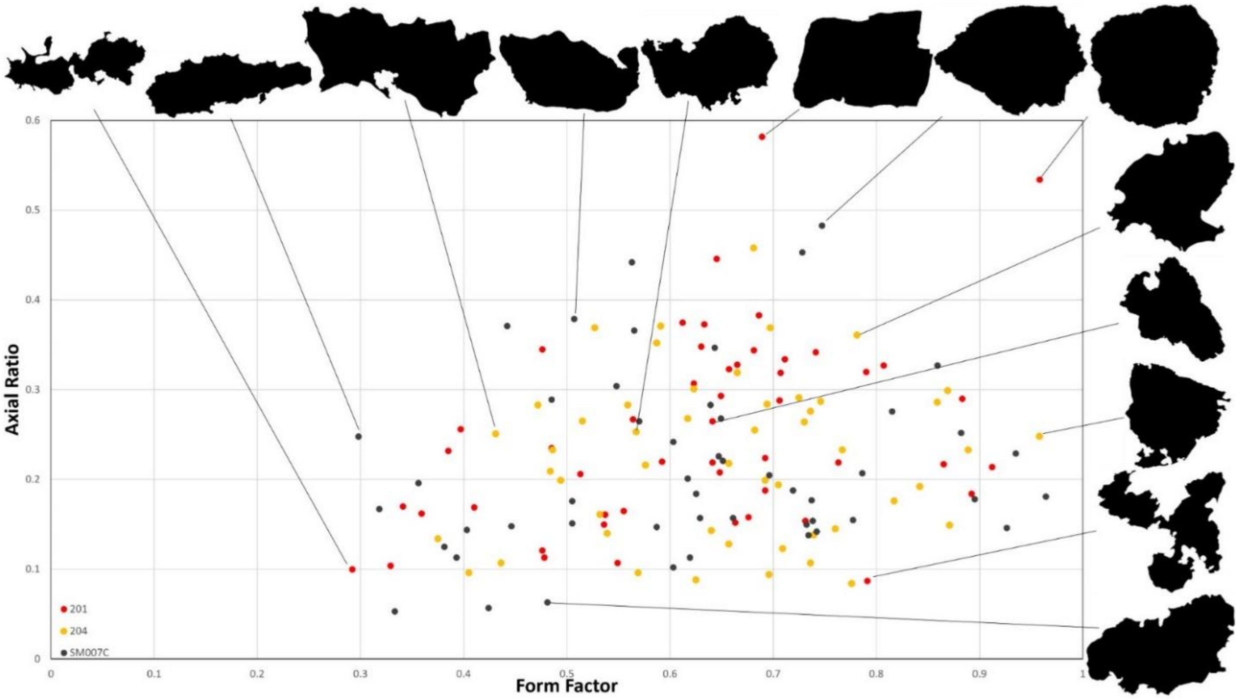

Figure 3.20. Axial ratio vs. form factor is plotted in comparing the three separate deposits. Silhouettes of representative particles are shown along the edge of the graph, tied to their sample dots on the graph.

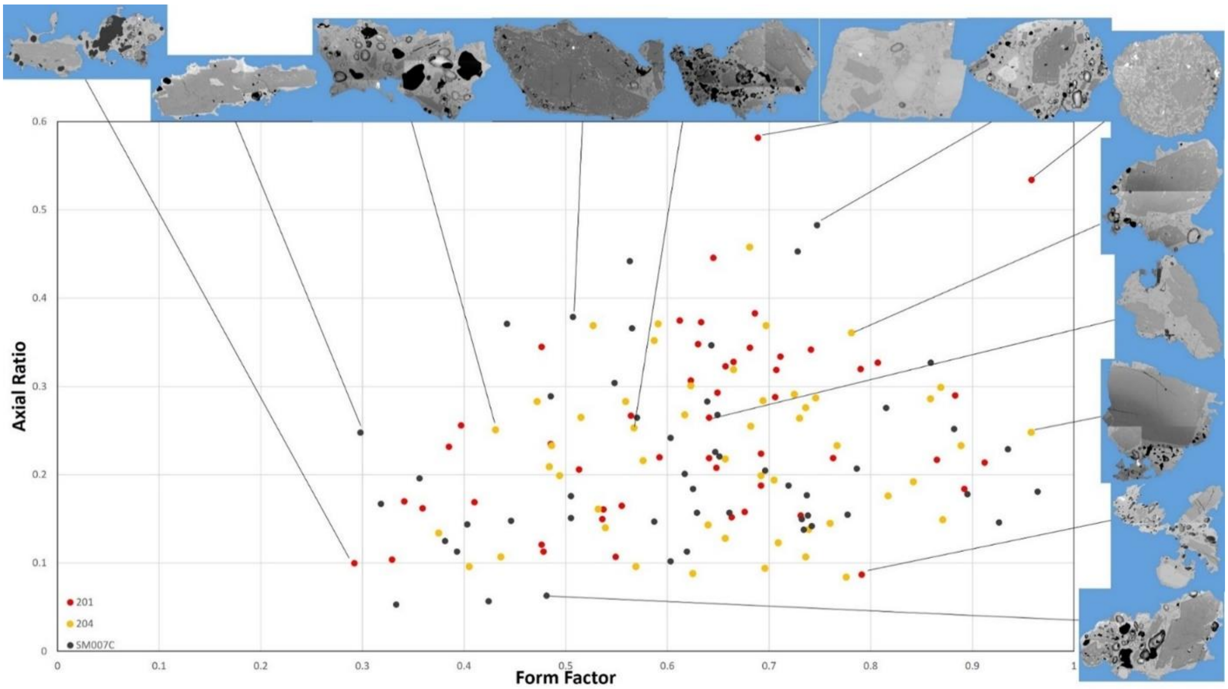

Figure 3.21. Plots the same data as Figure 3.20, only now with the backscattered SEM images of the particles previously shown as silhouette images. Displaying the relationship between particle texture/composition and morphological form.

3.3.3 Morphological Roughness

The mean convexity and solidity particles in each sample is given in Table 3.3. The higher the values, the more rounded the juvenile ash particle; the lower the values the more irregular the particle edges (Figures 3.22 and 3.23). The convexity in sample 0201 ranges from 0.428 - 0.859, the convexity in sample 0204 ranges from 0.370 - 0.746, the convexity in sample SM007C ranges from 0.315 -0.773. The solidity in sample 0201 ranges from 0.466 - 0.951, the solidity in sample 0204 ranges from 0.615 - 0.895, the solidity in sample SM007C ranges from 0.556 - 0.932.

Sample	Mean convexity value	Mean solidity value
0201	0.60	0.77
0204	0.56	0.78
SM007C	0.55	0.79
mean	0.57	0.78

Table 3.3. Mean convexity and solidity values of juvenile ash particles.

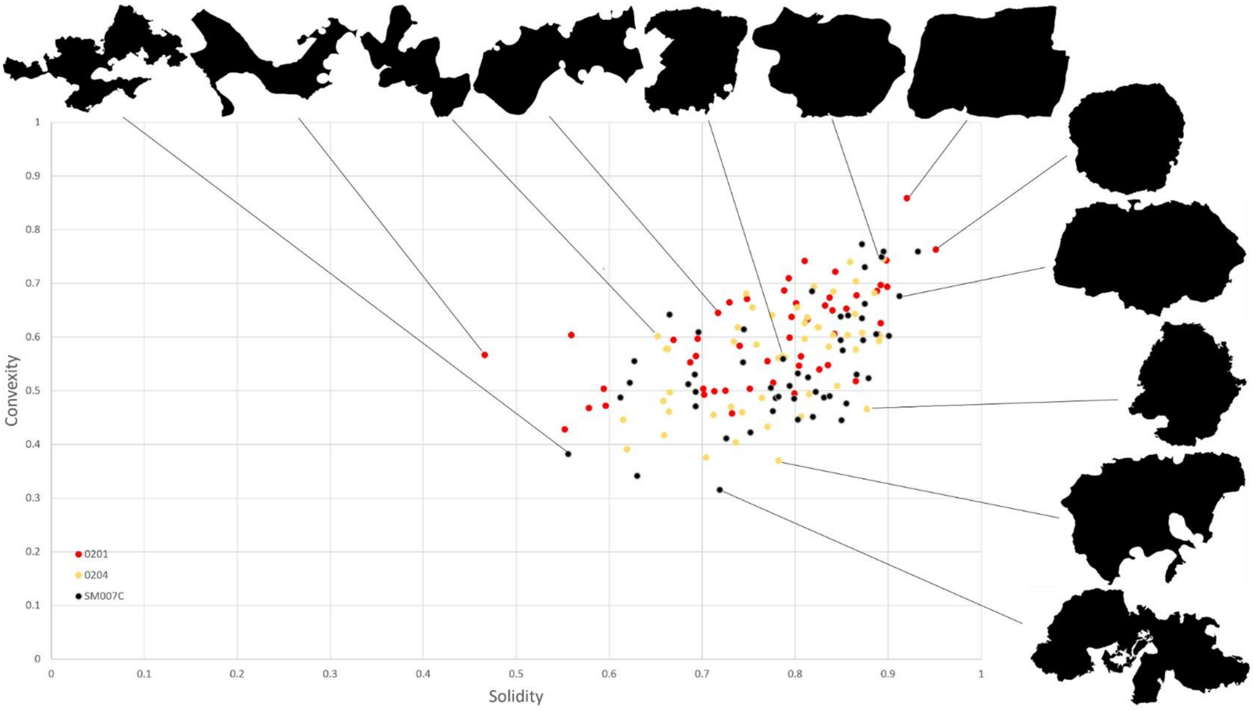

Figure 3.22. Convexity vs solidity is plotted in comparing the three separate deposits. Silhouettes of representative particles are shown along the edge of the graph, tied to their sample dots on the graph.

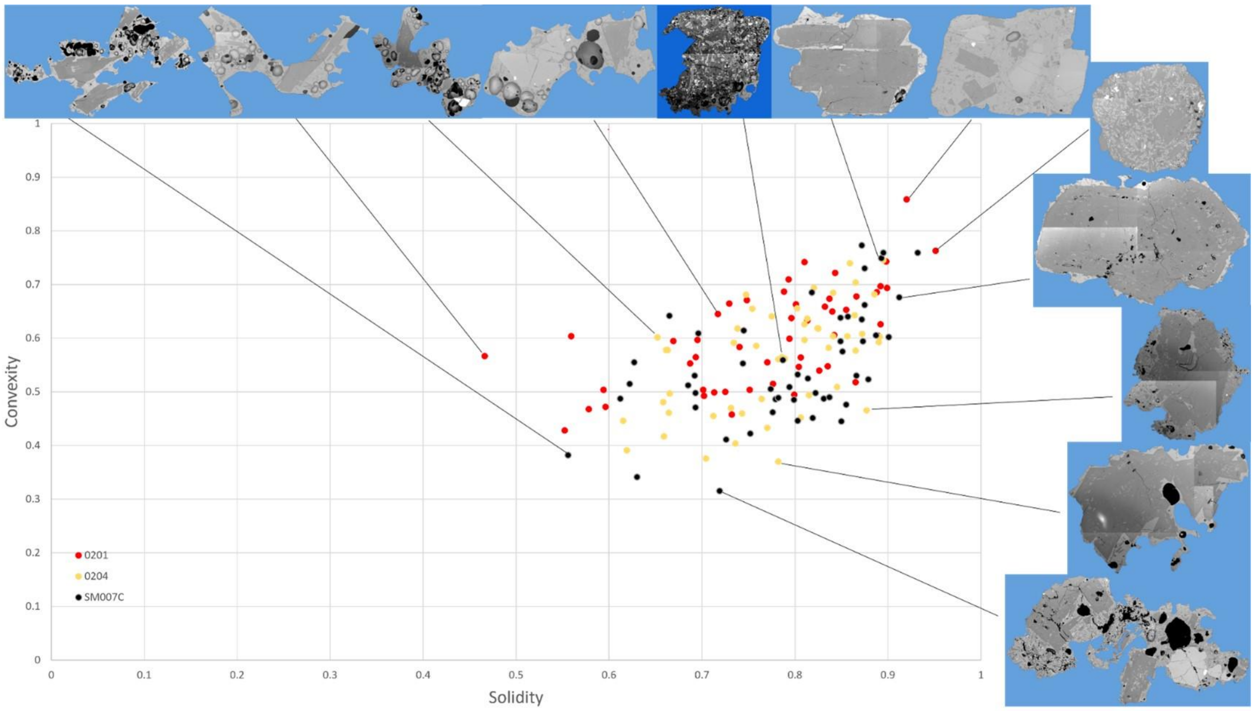

Figure 3.23. Plots the same data as Figure 3.22., only now with the backscattered SEM images of the particles previously shown as silhouette images. Displaying the relationship between particle texture/composition and morphological roughness.

There is no apparent correlation between particle type and axial ratio, form factor, convexity, or solidity. Some melt-coated crystal particles can show a shape that roughly outlines the crystal. However, they can also contain a glass coating or projection of other structures which can skew any correlation between shape and particles type. All three samples exhibit very comparable mean values for form axial ratio, factor, convexity, and solidity.

Chapter 4: Interpretation

4.1 Scoria

The composition and texture of scoria can provide information on the nature and dynamics of Strombolian eruptions, such as magma ascent velocity, mingling of new and previously erupted materials, and volatile content, and can aid in predicting the nature of future eruptions (e.g. Lautze and Houghton, 2005; Taddeucci et al., 2007; Cimarelli et al., 2010).

4.1.1 Phenocrysts

Observations of scoria samples agree with results from previous studies conducted on the 2013 eruption of San Miguel (Scarlato et al., 2016). Phenocrysts consist of plagioclase, olivine, pyroxene, and oxides, indicating a basaltic andesite magma. Plagioclase phenocrysts are inversely zoned, with partly resorbed cores surrounded by sieve-textured rims. Scarlato et al. (2016) interprets reverse zoned plagioclase phenocrysts with resorbed sodic cores and re-growth of sieve-textured calcic rims as being evidence of mixing of two distinct magmas. Mineral-melt equilibria and bulk rock modelling indicate that the eruption was triggered by the intrusion of high-temperature (~1130–1150°C) basaltic magma into a low-temperature (~1060–1080°C) shallow crustal basaltic andesite reservoir (Scarlato et al., 2016). The increase in anorthite content for the plagioclase rims suggests that the new magma was compositionally more primitive and possibly hotter and/or wetter. High-temperature gradients between the two magmas led to relatively rapid crystallization of sieve-textured, more calcic mantles (see also Hibbard, 1981; Shcherbakov et al., 2010). The final growth of plagioclase was controlled by the effect of undercooling due to rapid decompression during magma ascent to the surface (Scarlato et al., 2016). The textures of the plagioclase phenocrysts of this study correlate well with these conclusions.

Scarlato et al (2016) state that early-formed cores of olivine phenocrysts are expected to be in equilibrium with the original magma. The olivine phenocrysts of this study display little internal structure; this may indicate that all the olivine crystallized from the initial high-temperature magma. They also suggest that oxides within olivine cores indicate different variable melt conditions. The oxides observed in this study are not associated with any particular phenocryst composition; it can therefore be concluded that the oxides crystallized from a homogenous melt (Putirka et al., 2008)

4.1.2 Groundmass

Two types of volcanic glass are tachylite and sideromelane. Tachylite is largely opaque in transmitted light due to the inclusion of microlites, and sideromelane is microlite-poor or microlite-free and is therefore largely transparent (Fisher and Schmincke, 1984). The type that occurs is a function of cooling rate and conditions. Faster cooling results in fewer/no microlites (i.e., sideromelane). The rate of cooling is controlled by a number of factors, including flow rate and residence time in the conduit (e.g., Cimarelli et al., 2010; Murch and Cole, 2019) and cooling at a lava-water interface (with sideromelane being an indicator of quenching by external water (Fisher and Schmincke, 1984)).

The discovery of both tachylite and sideromelane glass in the groundmass of scoria ejected from San Miguel 2013 is new to this study. A homogeneous magma experiencing varying ascension rates within the conduit will result in different glass types: microlite-rich (i.e. tachylite) scoria from regions of the conduit where magma flowed more slowly, and microlite-poor (i.e. sideromelane) scoria where magma was flowing faster (Cimarelli et al., 2010). Additionally, the presence of sideromelane and tachylite glass may indicate different temperature zones within the eruptive conduit (Taddeucci et al., 2004). The higher percentage of tachylite glass in the scoria samples may suggest a longer residence time for the ascending magma. The 2013 San Miguel eruption is characterized as having rapid and brief explosive episodes (Scarlato et al., 2016; Brown et al., 2022), which could indicate a brief residence time for the ascending magma, dampening the effect of differential velocity. Tachylite results from a more complex crystallization history than sideromelane (Taddeucci et al., 2004), so a temperature differential is likely also required to explain the presence of both types of glass. It is therefore hypothesized that the ascending magma was likely cooled along the conduit margins by the presence of lower-temperature hydrated wall rock.

4.1.3 Lithic Material

Lithic clasts result from fragmentation of the walls of the magma chamber, conduit or vent, and become entrained in the eruptive column (Cas and Wright, 1987; Houghton and Smith, 1993). Explosive water-rock interaction, such as due to the presence of a pre-existing hydrothermal system, can enhance the process of lithic clast formation and entrainment (Brown et al., 2008; Valentine and Groves, 1996; Macedonio et al., 1994). Lithic clast shape is an indicator of the extent of the lithic material's exposure to magma prior to eruption. If lithic material was embedded in the magma deeper within the chamber or conduit, time for reshaping could be available. This would be exhibited by rounding, altered concentric rings around the lithic clast, and gradual transition from lithic clast to surrounding juvenile material; small and shallow-sourced accessory clasts have substantially reduced residence times and therefore less opportunity for reshaping (Campbell et al., 2013). Lithic clast colour can be indicative of hydrothermal alteration: the formation of clay minerals and precipitates give rise to lighter colours such as white and tan (Valentine and Groves, 1996; Salaun et al., 2010)

Lithic clasts account for approximately 1 vol % of sampled scoria from San Miguel. The lithic clasts found in the San Miguel scoria are mostly angular to sub-angular, indicating little to no time for entrainment and reshaping within the ascending magma. This supports the interpretation of rapid eruption of this material from a shallow depth. A melt coating on lithic clasts indicates prolonged exposure of the clasts to a melt prior to eruption (e.g. Porritt et al., 2012). Because San Miguel lithic clasts do not display this sort of secondary feature, it is likely that the fragments had a shallow source and brief interaction with the magma.

Lithic clast colour ranges from white to tan, grey and black. Darker-coloured lithic clasts (grey and black) exhibit a crystalline structure, while the lighter-coloured lithic clasts (white, grey and tan) do not appear to have any crystalline structure. In contrast to fresh juvenile material, lithic clasts are mostly dimmer in appearance in SEM images and contain cracks running throughout the clasts. The light colour and dim appearance both point to hydrothermal alteration of these lithic clasts, as clays are light-coloured with a dull luster. The darker-coloured lithic clasts may be from deeper in the conduit (below the hydrothermally-altered cap).

Cole (2015) describes lithic clasts from her study of San Miguel as having a generally dark grey to black groundmass with a light-coloured coating which she interprets to be hydrothermal alteration products. Brown et al. (2022) conclude that all 2013 pyroclastic deposits from San Miguel come from the initial phase of the eruption, due to explosive interaction between rising basaltic-andesite magma and groundwater in a hydrothermal system at the vent.

4.1.4 Plate Tephra

Scoria particles identified as plate tephra are found in the 2013 San Miguel samples. Ruth and Calder (2013) describe plate tephra as flattened, curved, and oblate to bladed in shape, with aligned phenocrysts and microlites. They interpret them as resulting from ductile thinning due to expansion shear of the walls of large erupting gas slugs, followed by brittle fragmentation of these bubble walls. The shearing causes the alignment of crystals and smaller entrained bubbles. They conclude that the presence of plate tephra is characteristic of highly unsteady and violent Strombolian eruptions, where large bursting gas slugs alternate with more sustained fire fountaining. Pioli et al. (2008) also link the formation of plate tephra to unsteady, violent Strombolian eruptions that include lava fountaining and tephra formation. Maicher and White (2001) and Schipper and White (2010) suggest that sideromelane plates form during hydrovolcanic eruptions, due to rapid water quenching of the walls of large bubbles.

The San Miguel plate tephra particles are curved and flattened (with a larger major axis, a shorter intermediate axis, and a very short minor axis.

4.2 Ash Aggregates

4.2.1 Aggregate Summary and Comparison

The aggregation of airborne volcanic ash particles during eruptions is an important control on the dispersal of ash through the atmosphere (Brown et al., 2011). Aggregation depends on the energy of the collision and the presence of a sticking mechanism such as electrostatic forces, hydrostatic bonds, and ice sintering (Brown et al., 2011). Ash aggregation occurs within vent-derived eruption plumes, umbrella clouds, and plumes rising above pyroclastic density currents (PDCs). Ash aggregates formed in volcanic ash clouds display a range of shapes, sizes, textures, structures, and particle size distributions. Larger, more complex aggregates occur proximally, and smaller aggregates dominate distal regions.

The type and structure of ash aggregates can help inform on the nature of deposition (Schumacher and Schmincke, 1991; Brown et al., 2010; Brown et al., 2012; Van Eaton et al., 2012; Burns et al., 2017; Hoult et al., 2022). For example, Brown et al. (2010) recognised that on Tenerife (AP1) aggregates were restricted to co-ignimbrite ash fall deposits while AP2 aggregates where restricted to PDC deposits. Ash clusters are fragile and are typically only found in ash fall deposits (Brown et al., 2012). The texture of ash-aggregate-bearing deposits can also help in the interpretation of the mode of deposition. (AP1) aggregates in ash fall deposits are commonly clast-supported and may have open pore space (Brown et al., 2013). (AP1) aggregates in PDC deposits are commonly matrix-supported and fragments of their rims may be distributed throughout the matrix (Brown et al., 2010; 2012; Van Eaton et al., 2012; Hoult et al., 2022).

The ash aggregates in the 2013 San Miguel eruption include particle clusters or accretionary pellets, following the classifications of Brown et al. (2012) and Durant and Brown (2016). Particle clusters (PC) include ash clusters (PC1) or coated particles (PC2). Accretionary pellets (AP) are subcategorized as poorly structured pellets (AP1) or pellets with concentric structure (AP2). Unit A, where most ash aggregates were found, is at its thickest a clast-supported layer composed of coated particles, ash clusters and (AP1) accretionary pellets. This evidence is consistent with it being a tephra fall deposit. The presence of (AP2) aggregates in pyroclastic deposits elsewhere has been attributed to passage of a PDC. However, the (AP2) aggregates in the 2013 eruption differ from those elsewhere: the layering is distinct (cf. Brown et al. 2012; Van Eaton et al., 2012; Hoult et al. 2022), and they lack the well-developed extremely fine-grained rims. The concentric layering in the 2013 aggregates may have developed in part through interaction between the eruption plume and the co-PDC ash cloud, but it remains uncertain.

Little work has been done with the aim of identifying internal lithofacies of ash aggregates. The only other study is that of Hoult et al. (2022), who conducted textural studies on the internal structure of (AP2) aggregates from the AD 436 TBJ eruption of Ilopango caldera. They recognised three distinct lithofacies that made up the cores and rims of the aggregates.

Core lithofacies from the San Miguel ash aggregate samples are mostly characterized as massive, vesicular, poorly sorted ash (MvA) in poorly structured pellets (AP1) and in pellets with concentric structure (AP2), similar to the massive fine ash (mA) described by Hoult et al. (2022). Core lithofacies also can exhibit massive, porous, poorly sorted ash (MpA) in (AP1) particles and in (AP2) particles, similar to the porous clustered fine ash (pcA) described by Hoult et al. (2022). Rims in the San Miguel 2013 (AP1) ash aggregates samples are predominantly (MvA) facies, slightly finer than the (MpA) facies which are found in their cores. (AP2) particles can also display rims of (MpA) or (pcA) facies, with coarser cores or in some cases coarser preceding rims.

Coated particles (PC2) display a series of rims. Rims closest to the core are discontinuous and fill in the indenting portions or edges of particle's cores. These are made up of extremely fine ash (efA), similar to the laminated ultrafine ash (lufA) described by Hoult et al. (2022). Discontinuously around these rims are rims of slightly finer or coarser (efA) facies.

Hoult et al. (2022) concludes that changes in aggregation conditions during the growth of aggregates accounts for variations in lithofacies and texturally distinct layers. The amount of water available in the ash cloud appears to control the range of possible particle sizes as well as the maximum aggregate size. The overall layering forms as particle descend from high-level ash clouds (vent-derived or co-PDC plumes) and encounter regions of varying water content, temperature, and ash size and concentration.

This study's aggregates differ from those found in Hoult et al. (2022) mainly in size and number of lithofacies present within a single ash aggregate. This would align with their findings as well as those from Brown et al. (2022). San Miguel 2013 was a relatively short and small eruption in comparison with the TBJ aggregates. Therefore, the observation of smaller and fewer lithofacies found within San Miguel 2013 aggregates confirms the standing models.

The analysis of the 2013 aggregates reveals that increases in aggregate size do not correlate to increases in the number or thickness of finer-grained rims. Therefore, an increase in aggregate size does not correlate to aggregate maturity or airborne time. Rather, is it more likely that the amount of moisture and availability of airborne particles are responsible for more complex ash aggregates. The thin nature of the Unit A deposit suggests that the conditions that led to aggregate formation were short lived. Given that aggregates fell within 1 km of the volcano, the airborne time for these aggregates is considered short (of the order of minutes).

The presence of smaller aggregates (PC1 and PC2) within larger aggregates, either as discrete particles (PC2 coated particles) or multiple aggregates (PC1 ash clusters) indicates that the larger aggregates are at least in part composed of numerous smaller aggregates. This is similar to observations made by Hoult et al. (2022). It suggests that the aggregation process is composed of a series of stages that may occur in different environments, or under different ambient conditions.

Hoult et al. (2022) summarize the results of various laboratory experiments and field observations to explain ash aggregate growth. In general, large complex aggregates tend to be characterized by a general increase in particle size from core to rim, a variety of overall morphologies, layering that is defined by both texture and grain size variation, and rims of very fine-grained ash. Hoult et al. (2022) concludes that the Ilopango aggregates began to form when fine ash particles at the edges of a vent-derived or co-PDC plume formed loose particle clusters. The presence of pumice clasts in the cores of some aggregates indicates that these particles were in the plume, either in turbulent suspension or just coincidentally passing through the ash cloud. As these particles descended, they collided with other clusters and increased in size through growth. They continued to descend and became saturated, accreting a thick, poorly-sorted, massive layer of fine ash. Further descent through a dilute, ultrafine co-PDC cloud caused the formation of the outermost ultra-fine rim.

While Hoult et al. (2022) studies depict far greater complexity within their studies aggregates as opposed to those of San Miguel, the process it the same. Instead of a pumice clast core, San Miguel 2013 aggregates display a scoria core derived from their associating basaltic-andesitic magmatic source. San Miguel 2013 aggregates also display particles clusters that cemented together to create (AP1) and (AP2) aggregates. Lastly San Miguel 2013 aggregates also display outermost fine as rims resulting from the turbulent churning within a co-PDC.

4.2.2 Evidence for Phreatomagmatism

Ash aggregation is a common process during explosive volcanic eruptions, and is particularly common, but is not unique, to phreatomagmatic eruptions (White et al., 2016). Simple ash aggregates (AP1) can form during magmatic eruptions through the ingestion of atmospheric moisture (Gilbert and Lane 1994). Brown et al. (2022) interpreted the early vent clearing explosion from the 2013 eruption as a result of explosions between magma and groundwater or a hydrothermal system, based primarily on the low apparent temperature of the PDC and the abundant ash aggregates in Unit A which they attributed to the PDC.

This research has revealed that the volcanic ash that makes up the ash aggregates is rich in lithic particles, an observation consistent with explosions driven by subsurface phreatomagmatism. The lithic ash particles display a range of igneous and volcanic textures and are inferred to be fragments of pre-existing lavas, crystals, pyroclasts and pyroclastic rocks. Many appear strongly altered and are difficult to identify, suggesting the presence of a long-live active hydrothermal system in the volcano. Contributions to aggregation from atmospheric clouds can be ruled out, because although clouds were ingested by the eruption column during the eruption, this did not occur until later, and atmospheric conditions at the start of the eruption were clear (see Brown et al., 2022). Additional evidence for phreatomagmatic activity includes the presence of lithic lapilli and ash particles intimately mixed with the scoria erupted later in the eruption (Unit C). This suggests that although the eruption appeared primarily magmatic, and erupted predominantly vesicular scoria, ongoing phreatomagmatic explosions may have occurred, generated lithic debris that was then incorporated into juvenile tephra in the conduit or in the eruption jet.

4.3 Juvenile Ash Particles

4.3.1 Particle Texture and Morphology

The physical properties of erupted pyroclasts record the magmatic conditions prior to and during fragmentation; if particles are not changed by post-eruption processes, particle morphology will preserve information about how fragmentation occurred (i.e. brittle vs. ductile), and internal vesicle and crystal textures will preserve information on the conditions of magma ascent (Büttner et al., 2002; Liu et al., 2015).

There is no definitive corelation between particle texture/composition and the morphology of a particle’s edge in this study. Previous studies discuss melt fragmentation or melt-coated crystals resulting in brittle deformation in post fragmentation events which are hydrated, while glassy particles displaying ductile deformation (Liu, et al., 2017). Particles in this study display brittle deformation, ductile deformation, or both, no matter what the internal texture is. Therefore, it cannot be concluded from this study that deformation style and fragmentation style are associated.

The internal textures/composition of the juvenile ash particles erupted from San Miguel 2013 do not display any discernible differences among samples aside from the percentage of melt coated crystals vs. glassy particles. These textures are all in agreement with those found in the scoria samples.

Evidence of both brittle and ductile deformation in particles (see Figures 3.18 and 3.19) suggest they could have experienced several fragmentation events, first by magmatic fragmentation in a ductile state followed by cooling, and then potentially brittle fragmentation during an explosive collision. The 2013 San Miguel event erupted juvenile ash particles displaying broken edges and vesicles indicating brittle deformation, and juvenile ash particles displaying rounded edges and vesicles indicating ductile deformation. Ash particles with blocky and rounded morphologies are often associated with hydromagmatic-magmatic eruptions, while ash particles with angular morphologies are often associated with rapidly quenching phreatomagmatic eruptions (Liu et al., 2017).

4.3.2 Sample Comparisons

As shown in Tables 3.2 and 3.3, San Miguel juvenile ash deposits of samples 0201, 0204, and SM007C all display comparable values in terms of mean values for axial ratio, form factor, convexity, and solidity (Figure 4.3.1)(also located in Appendix). However, each displays a few outlying values for each morphological measurement. For sample 0201, these outlying values are as follows: convexity = 0.859, solidity = 0.466 and 0.951, axial ratio = 0.582, and form factor = 0 .958. For sample 0204, outlying values are as follows: convexity = 0.446, solidity = 0.859, axial ratio = 0.458, and form factor= 0 .958. For sample SM007C, outlying values are as follows: convexity = 0.315, solidity = 0.556, axial ratio = 0.747, and form factor = 0.298. This could be the indicators to different/separate short lived eruptive events that occurred closely together or simultaneously. The mean values of these samples along with the internal texture/

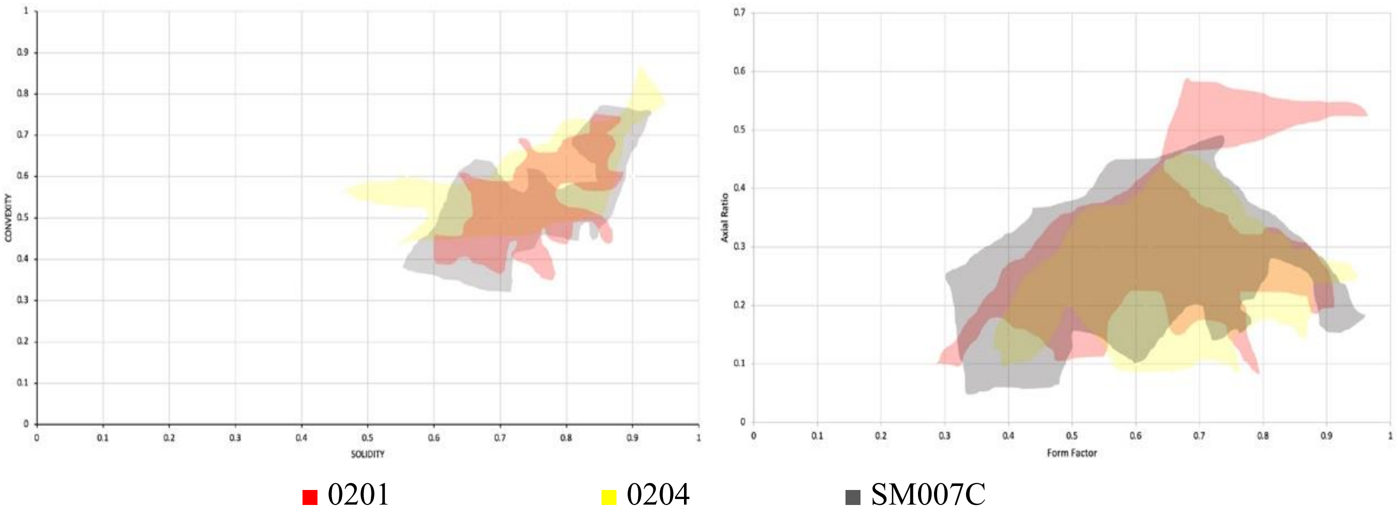

Figure 4.3.1. San Miguel samples 0201 (red), 0204 (yellow) and SM007C (grey): Comparison of convexity, solidity, axial ratio and form factor (also located in Appendix).

composition suggests that all of the material experienced comparable fragmentation processes. Given that this study only looks at the juvenile ash particles it is more likely that the addition other ash particles are better indicators of eruptive processes (i.e., lithic ash particles). This notably being the transition from more lithic dominate ash deposits to more juvenile ash deposits previously mentioned. From this study it is hypothesized that it was not until post initial fragmentation that there was a difference in sample characteristics. Brown et al. (2022) suggest five eruptive phases, with the first two phases being the most important in differentiating eruptive explosions.

4.3.3 Eruption Comparison

San Miguel mean values of axial ratio, form factor, convexity, and solidity were compared to historic eruptions of Grímsvötn in 2011, Eyjafjallajökull in 2010, Surtsey in 1963, Tambora in 1815, and Mount St Helens in 1980 (supplemental data provided by Emma Liu). Comparisons between eruption style and mean values are shown in Figures 4.3.2 and

4.3.3(also located in Appendix). Hydromagmatic fall deposits are associated with higher particle convexity and solidity values or roundness and lower axial ratio and form factor values or particle roughness. Magmatic fall deposits are associated with even higher particle convexity and solidity values/roundness and higher axial ratio and form factor values or particle roughness.

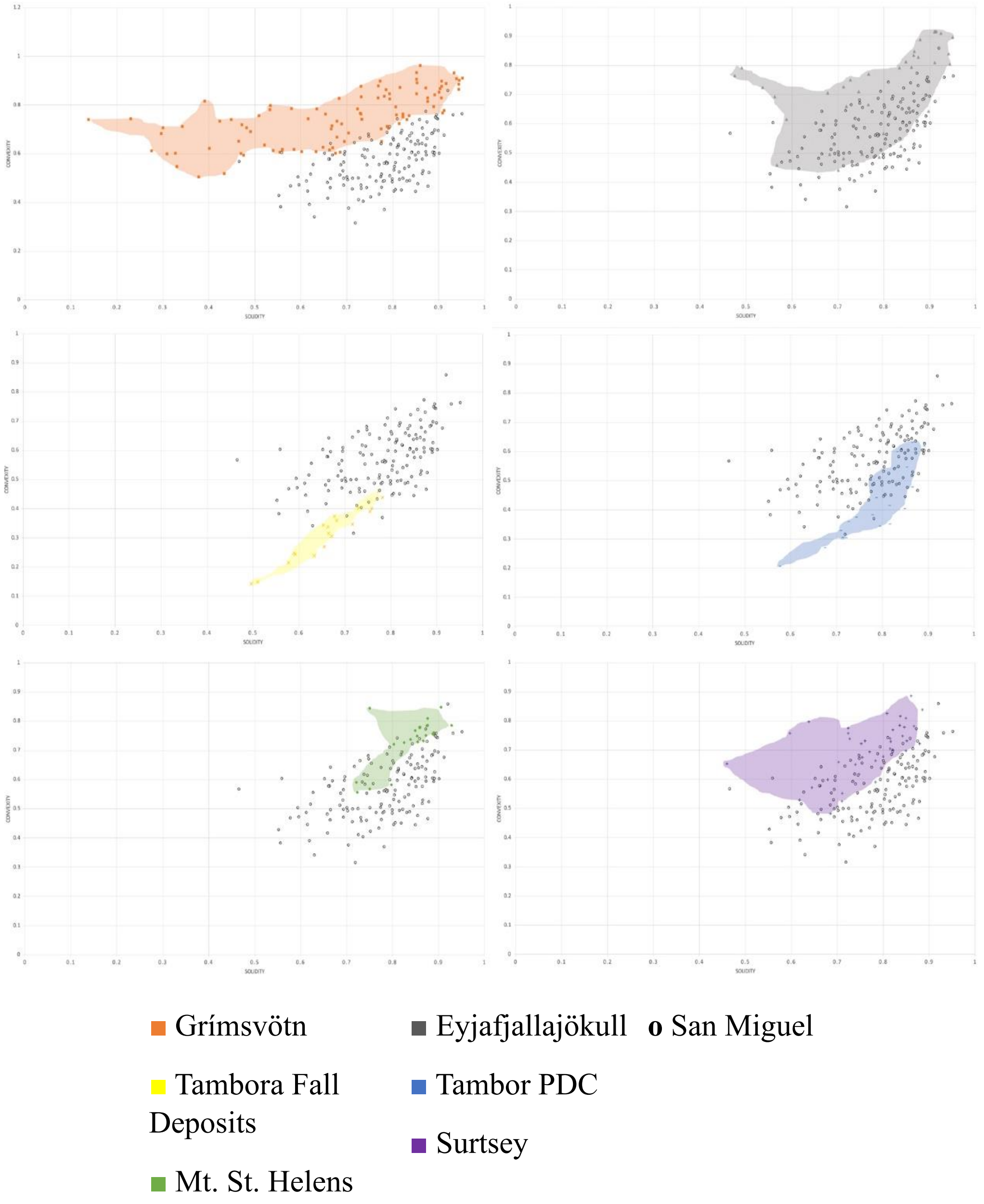

Figure 4.3.2. Comparison of convexity and solidity for San Miguel and selected historic eruptions (Liu et al., 2015) (also located in Appendix).

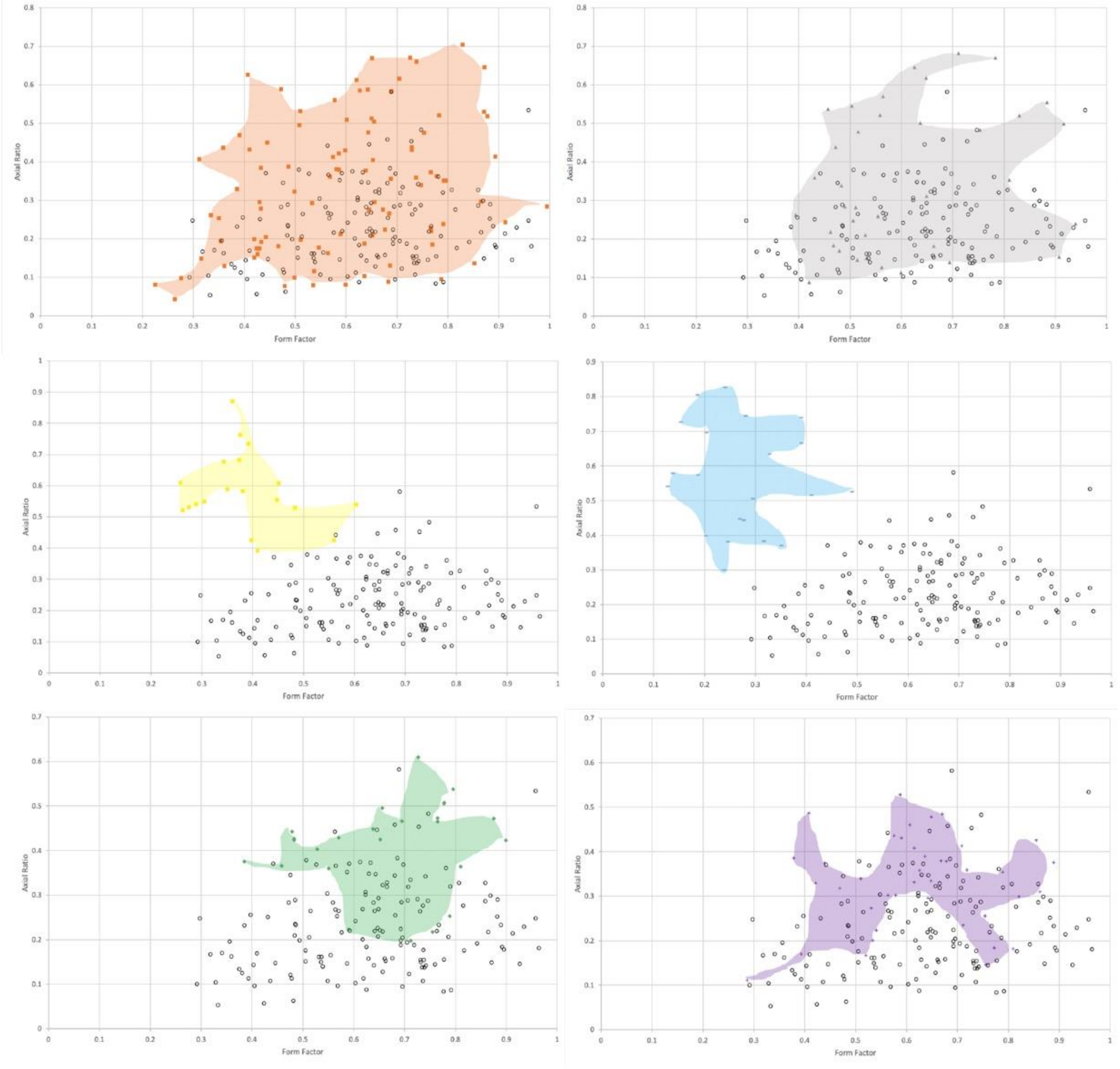

🟧 Grímsvötn

🟨 Tambora Fall Deposits

🟩 Mt. St. Helens

⬛ Eyjafjallajökull

🟦 Tambor PDC

🟪 Surtsey

o San Miguel

Figure 4.3.3. Comparison of axial ratio and form factor for San Miguel and selected historic eruptions (Liu et al., 2015) (also located in Appendix).

Mean values for axial ratio and form factor of San Miguel 2013 samples closely resemble eruptions highlighted in Table 4.3.1. Both the axial ratio mean value and form factor mean value compare closely to that of the Surtsey (1963) hydromagmatic fall deposit.

Mean values for convexity and solidity of San Miguel 2013 samples closely resemble eruptions highlighted in Table 4.3.1. The convexity mean value is closest to that of the Tambora, 1815 (magmatic PDC deposit), while the solidity mean values are closest to the Eyjafjallajokull 2010 hydromagmatic fall deposit, but not very different from the solidity value for the Tambora 1815 magmatic PDC deposit.

Eruption	Axial Ratio Mean Value	Form Factor Mean Value	Convexity Mean Value	Solidity Mean Value
San Miguel 2013	0.6349	0.2306	0.5712	0.7804
Grimsvotn 2011 (hydromagmatic fall deposit)	0.5967	0.3344	0.7505	0.6790
Eyjafjallajokull 2010 (hydromagmatic fall deposit)	0.6068	0.3536	0.7144	0.7749
Surtsey 1963 (hydromagmatic fall deposit)	0.6206	0.3303	0.7045	0.7656
Tambora 1815 (magmatic fall deposit)	0.3848	0.5855	0.3151	0.6618
Tambora 1815 (magmatic PDC deposit)	0.2725	0.5621	0.4291	0.7870
Mt. St. Helens 1980 (magmatic fall deposit)	0.6646	0.4124	0.7375	0.8439

Table 4.3.1. San Miguel’s mean values of convexity, solidity, axial ratio, and form factor compared to other eruptions studied by (Liu et al. 2015). Highlighted values of different eruptions show those closest to the values of San Miguel 2013.

Based on these comparisons of juvenile ash particle morphologies, the San Miguel 2013 eruptive style is comparable to historic eruptions of hydromagmatic and magmatic PDC deposits. From these observations two conclusions can be drawn: the 2013 eruption experienced different eruptive phases during its total eruption, and an interaction with water occurred at some point. This interpretation, along with the differences in morphology illustrated by both brittle and ductile deformation of ash particles, support the conclusion that the San Miguel 2013 eruption was a multiphased magmatic and phreatomagmatic event.

4.4 Eruption Summary

Scarlato et al. (2016) concluded, on the basis of mineral-melt equilibria and bulk rock chemical modelling that the 2013 eruption was triggered by the input of hotter, basaltic magma from depth into a colder, basaltic andesitic reservoir residing at shallow crustal levels. Magma mixing is supported by the textural and compositional characteristics of mainly olivine and titanomagnetite reflecting different crystallization histories and by the occurrence of inversely zoned plagioclase showing partly resorbed cores surrounded by sieve-textured mantles. The final growth of plagioclase was controlled by the effect of undercooling due to rapid decompression during magma ascent to the surface.

The discovery in this study of tachylite and sideromelane glass indicates that the ascending magma may have undergone a complex ascent history, with batches of magma experiencing moving faster or slower in the conduit, or erupting at different temperatures (e.g., Cimarelli et al., 2010; Taddeucci et al., 2004). This study proposes that as the magma quickly ascended the conduit, crystallization of tachylite glass began to occur along the cool hydrated conduit walls. Sideromelane glass which began to crystalize in the center of the conduit was unexposed to the margins thus left to ascend and crystalize later. The discovery of plate tephra suggests the bursting of large slugs during violent Strombolian eruptions characterised by fountains and plumes.

Brown et al. (2022) notes visible eruptive activity in the crater started with increasing water vapour emissions rising to heights of a few hundred metres above the crater. Initial phreatomagmatic activity, driven by interaction of the rising magma with a hydrothermal system is partly confirmed by this study by the presence of lithic clasts, many of which are strongly hydrothermally altered, throughout the scoria clasts. Many of the lithic clasts are hydrothermally altered implying the existence of active hydrothermal system prior to an explosive eruption (e.g., Pittari et al., 2008). This marks the first major eruptive phase and the phreatomagmatic explosion cleared the vent. Hydrothermally altered material sized from ash to bombs litter the upper cone and some sections of the volcano’s slopes.

This is followed by the second main phase of the eruption which marked by a two-part explosion. The first being a magmatic explosion, indicated by the dark ash cloud on webcam footage. Occurring at the same time as another phreatomagmatic explosion that generated a cool PDC that entered plantations but did not incinerate surrounding vegetation (Brown et al., 2022). The high moisture content within this eruptive phase produced lithic coated juvenile clasts and plastered crater walls and vegetation with ash (Brown et al., 2022).

The presence of ash-coated scoria clasts, ash-aggregates, and ash plastered to surfaces in the crater are consistent with phreatomagmatic explosions being driven by rising magma and groundwater (Brown et al., 2022). This study indicates that the ash particles in the aggregates are predominantly lithic clasts, while juvenile ash particles in the aggregates rules out a purely phreatic explosion (Búttner et al., 1999; Doubik and Hill, 1999). The San Miguel 2013 ash aggregates are not well developed which supports their formation in a co-PDC cloud (e.g., Durant and Brown, 2014). The under development of the aggregates is also consistent with a short-lived, small-volume PDC. The textual and morphologic analysis of the juvenile ash particles provide further evidence of magma–water interaction when compared to historical eruptions. Matching characteristics with those of Surtsey 1963 (hydromagmatic fall deposit), Eyjafjallajokull 2010 (hydromagmatic fall deposit), and Tambora 1815 (magmatic PDC deposit) eruptions. Providing further evidence for a phreatomagmatic explosion, a magmatic explosion, and an accompanying PDC

Conclusions

New analysis and interpretation of scoria samples from the 2013 San Miguel eruption in El Salvador include the discovery of tachylite and sideromelane glass, and lithic clasts in scoria samples. These suggest separate fragmentation events. One was magmatic, with different cooling mechanisms producing different glass types. The other was the explosion of a pre-existing hydrothermal system, producing the lithic clasts. Additionally, the observation of plate tephra suggests a violent Strombolian component. Ash aggregates from the San Miguel 2013 eruption are lithic-rich and poorly developed. This is consistent with the aggregates generated by a co-PDC cloud formed from a short-lived, small volume PDC. This co-PDC was generated by a phreatomagmatic explosion. Textural and morphological analysis of juvenile ash particles correlate with studies of other eruptions; values of convexity, solidity, axial ratio, and form factor resemble those of eruptions that are characterized as magmatic/hydromagmatic.

“The copyright of this thesis rests with the author. No quotation from it should be published without the author's prior written consent and information derived from it should be acknowledged.”

Acknowledgements

I would first and foremost like to thank Dr. Richard Brown and his family for the opportunity to join this project and all the help and supervision that he provided throughout. Thank you to Dr. Emma (Liu) Nicholson of the University College London for her assistance in providing information associated with the project. I would also like to express my gratitude and appreciation for the entire Earth Sciences faculty from top to bottom for their part in the project. No matter how small it truly made all the difference.

A sincere and heartfelt thank you to Dr. Helen Mango of Castleton University. Without whom I would not be in the position that I am in, and I couldn’t be more grateful for her presence in my life. Additionally, a thank you to Dr. Christine Palmer of Castleton University for her unwavering emotional support.

Lastly, I would like to thank all the connections and friendships I have made throughout this journey and in my time at Durham. Academics is rewarding but the people you meet in between are just as important.

References

Büttner, R., Zimanowski, B., & Röder, H. (2000). Short-time electrical effects during volcanic eruption: Experiments and field measurements. Journal of Geophysical Research: Solid Earth, 105(B2), 2819-2827

Büttner, R., Zimanowski, B., Wohletz, K., Dellino, P. (2002). The volcanic ash problem. Journal of Volcanology and Geothermal Research, 122(1-2), 1-5.

Brown R, Hernandez W, Escobar D, Crummy J, Cole R, Tournigand P (2022) Reconstruction of the 29th December 2013 Eruption of San Miguel Volcano, El Salvador, using Video, Photographs and Pyroclastic Deposits

Brown RJ, Buse B, Sparks RSJ, Field M (2008) On the welding of pyroclasts from very low-viscosity magmas: examples from kimberlite volcanoes. Jour Geol 116(4):354-374

Brown RJ, Branney MJ, Davila-Harris P, Maher C (2010) Origin of accretionary lapilli within ground-hugging density currents: Evidence from pyroclastic couplets on Tenerife. Geol Soc Amer Bull 122(1):305-320

Brown RJ, Bonadonna C, Durant AJ (2011) A review of volcanic ash aggregation. Phys Chem Earth, Parts A/B/C, 45–46:65-78 https://doi.org/10.1016/j.pce.2011.11.001

Brown, R. J., Civetta, L., Arienzo, I., D'Antonio, M., Moretti, R., Orsi, G., ... & Menzies, M. A. (2014). Geochemical and isotopic insights into the assembly, evolution and disruption of a magmatic plumbing system before and after a cataclysmic caldera-collapse eruption at Ischia volcano (Italy). Contributions to Mineralogy and Petrology, 168, 1-23.

Brown, R. J., Hernandez, W., Loughlin, S., Crummy, J., (2014), Deposits of the 29th December 2013 Eruption of Volcán San Miguel, El Salvador, Abstract, Cities on

Volcanoes, Yogyakarta, 9-13 September 2014

Burns, A. J., Kavanagh, J. L., Hazim, S. H., Wood, E. P., Martin, S. A., Hignett, S., & Dennis, D. J. (2017). Challenging dyke ascent models using novel laboratory experiments: Implications for reinterpreting evidence of magma ascent and volcanism. Journal of Volcanology and Geothermal Research, 354, 87-101.

Durant AJ, Brown RJ (2016) Ash Aggregation in Volcanic Clouds (Chapter 3). In: Mackie S, Cashman K, Ricketts H, Rust A, Watson M (Eds), Volcanic Ash, Elsevier, 53-65 https://doi.org/10.1016/B978-0-08-100405-0.00006-9

Campbell ME, Russell J, Porritt LA (2013) Thermomechanical milling of accessory lithics in volcanic conduits. Earth Planet Sci Let, 377:276-286

Carr, M. J., Mayfield, D. G., & Walker, J. A. (1981). Relation of lava compositions to volcano size and structure in El Salvador. Journal of Volcanology and Geothermal Research, 10(1-3), 35-48.

Cas, R. A. F., & Wright, J. V. (1987). Volcanic successions, modern and ancient: a geological approach to processes, products and successions. London: Allen and Arnold.

Chesner CA, Pullinger CR, Escobar CD (2004) Physical and chemical evolution of San Miguel volcano, El Salvador. In: Rose WI, Bommer JJ, López DL, Carr MJ (Eds) Natural hazards in El Salvador. GSA Spec Paper 375, Geol Soc Amer 213-226

Cimarelli C, Van Eaton AR, Muirhead JD, Wilson CJN (2010) Growth of volcanic ash aggregates in the presence of liquid water and ice: an experimental approach. Bull Volc 74:1963–1984

Cole R (2015) Nature and significance of pyroclastic deposits from 29th December 2013 San Miguel eruption, El Salvador. MSci Thesis Durham University 33 pp

Comida PP, Ross P-S, Durig T, White JDL, Lefebvre N (2021) Standardized analysis of juvenile pyroclasts in comparative studies of primary magma fragmentation; 2. Choice of size fractions and method optimization. Bull Volc 84:1-32 https://doi.org/10.1007/s00445-021-01517-5

Doubik, P., & Hill, B. E. (1999). Magmatic and hydromagmatic conduit development during the 1975 Tolbachik eruption, Kamchatka, with implications for hazards assessment at Yucca Mountain, NV. Journal of Volcanology and Geothermal Research, 91(1), 43-64.

Dzierma Y, Wehrmann H (2014) Probabilities of future VEI ≥ 2 eruptions at the Central American Volcanic Arc: a statistical perspective based on the past centuries' eruption record. Int Jour Earth Sci 103:2029-2042

Escobar CD (2003) San Miguel Volcano and its Volcanic Hazards. MS Thesis Michigan Technological University 163 pp

Fisher R, Schmincke H-U (1984) Pyroclastic Rocks Springer-Verlag 472 pp
Gilbert, Jennie S., and S. J. Lane. "The origin of accretionary lapilli." Bulletin of Volcanology 56 (1994): 398-411.

Global Volcanism Program (Smithsonian Institution)
https://volcano.si.edu/volcanolist_countries.cfm?country=El%20Salvador

Granieri, D., Salerno, G., Liuzzo, M., La Spina, A., Giuffrida, G., Caltabiano, T., ... & Papale, P. (2015). Emission of gas and atmospheric dispersion of SO2 during the December 2013 eruption at San Miguel volcano (El Salvador, Central America). Geophysical Research Letters, 42(14), 5847-5854.

Gutiérrez E, Carcamo RAC, (2021) Volcanic monitoring and hazard assessment in El Salvador. Volcanica 4(S1):183-201

Hibbard, M. J. (1981). The magma mixing origin of mantled feldspars. Contributions to Mineralogy and Petrology, 76(2), 158-170.

Houghton BF, Smith RT (1993) Recycling of magmatic clasts during explosive eruptions: Estimating the true juvenile content of phreatomagmatic volcanic deposits. Bull Volc 55:414-420

Hoult H, Brown R, Van Eaton A, Hernandez W, Dobson K, Woodward R (2022) Growth of complex volcanic ash aggregates—Insights from the Tierra Blanca Joven eruption of Ilopango Caldera, El Salvador. Jour Volc Geotherm Res 431:107670

Jiménez, D., Becerril, L., Bartolini, S., Escobar, D., Martí, J., 2020, Making a qualitative volcanic-hazards map by combining simulated scenarios: An example for San Miguel Volcano (El Salvador), Jour. Volc. Geotherm. Res., 395, 106837

Lautze, N. C., & Houghton, B. F. (2005). Physical mingling of magma and complex eruption dynamics in the shallow conduit at Stromboli volcano, Italy. Geology, 33(5), 425-428.

Leeman, W. P., Gerlach, D. C., Garcia, M. O., & West, H. B. (1994). Geochemical variations in lavas from Kahoolawe volcano, Hawaii: evidence for open system evolution of plume-derived magmas. Contributions to Mineralogy and Petrology, 116, 62-77.

Lexa J, Sebesta J, Chávez JA, Hernández W, Pecskay Z (2011) Geology and volcanic evolution in the southern part of the San Salvador Metropolitan Area. Jour of Geosci 56:106-40

Liu EJ, Cashman KV, Rust AC (2015) Optimising shape analysis to quantify volcanic ash morphology. Geo Res J 8:14-30

Liu EJ, Cashman KV, Rust A, Höskuldsson, A (2017) Contrasting mechanisms of magma fragmentation during coeval magmatic and hydromagmatic activity: the Hverfjall Fires fissure eruption, Iceland. Bull Volc 79:68

Macedonio G, Dobran F, Neri A (1994) Erosion processes in volcanic conduits and application to the AD 79 eruption of Vesuvius. Earth Plan Sci Let 121:137-152

MacMillan, I., Gans, P. B., & Alvarado, G. (2004). Middle Miocene to present plate tectonic history of the southern Central American Volcanic Arc. Tectonophysics, 392(1-4), 325-348.

Maicher M, White JD (2001) The formation of deep-sea limu o Pele. Bull Volc 63:482-496

Major JJ, Schilling SP, Sofield DJ, Escobar CD, Pullinger CR (2001) Volcano hazards in the San Salvador Region, El Salvador. U.S.G.S. Open-File Report 01-366 doi.org/10.3133/ofr01366

Martinez-Hackert, B., Bajo, J. V., Escobar, D., & Gutierrez, E. (2015, December). Chaparrastique (San Mighel) Volcano Eruptions since Dec. 29th, 2013, El Salvador. In AGU Fall Meeting Abstracts (Vol. 2015, pp. V23A-3087).

Murch, A. P., & Cole, P. D. (2019). Using microlites to gain insights into ascent conditions of differing styles of volcanism at Soufrière Hills Volcano. Journal of Volcanology and Geothermal Research, 384, 221-231.

Pioli L, Erlund E, Johnson E, Cashman K, Wallace P, Rosi M, Delgado Granados H (2008) Explosive dynamics of violent Strombolian eruptions: the eruption of Parícutin Volcano 1943–1952 (Mexico). Earth Planet Sci Let 271:359-368

Pittari A, Cas RAF, Wolff JA, Nichols HJ, Larson PB, Martí J (2008) The use of lithic clast distributions in pyroclastic deposits to understand pre-and syn-caldera collapse processes: a case study of the Abrigo Ignimbrite, Tenerife, Canary Islands (Ch. 3). Devel Volcan 10:97-142

Porritt LA, Campbell ME, Russell J, (2012) Thermomechanical milling of accessory lithics in volcanic conduits. Earth Planet Sci Let, 377:276-286

Protti, M., Gïendel, F., & McNally, K. (1995). Correlation between the age of the subducting Cocos plate and the geometry of the Wadati-Benioff zone under Nicaragua and Costa Rica.

Putirka K (2008) Thermometers and barometers for volcanic systems. In: Putirka KD, Tepley F (Eds.) Minerals: Inclusions and Volcanic Processes. Rev Min Geochem 69:61–120

Ross P-S, Durig T, Comida PP, Lefebvre NS, White JDL, Andronico D, Thivet S, Eychenne J, Gurioli L (2021) Standardized analysis of juvenile pyroclasts in comparative studies of primary magma fragmentation; 1. Overview and workflow. Bull Volc doi.org/ 10. 1007/ s00445- 021- 01516-6

Ruth DCS, Calder ES (2013) Plate tephra: Preserved bubble walls from large slug bursts during violent Strombolian eruptions. Geology 42:11-14

Scarlato P, Mollo S, Del Bello E, von Quadt A, Brown RJ, Gutierrez E, Martinez-Hackert B, Papale P (2016) The 2013 eruption of Chaparrastique volcano (El Salvador): Effects of magma storage, mixing, and decompression. Chemi Geol 448:110-22

Salaün, A., Villemant, B., Gérard, M., Komorowski, J. C., & Michel, A. (2010). Hydrothermal alteration in andesitic volcanoes: trace element redistribution in active and ancient hydrothermal systems of Guadeloupe (Lesser Antilles). Journal of Geochemical Exploration, 111(3), 59-83.

Schipper CI, White JDL (2010) No depth limit to hydrovolcanic limu o Pele: Analysis of limu from Lo'ihi Seamount, Hawai'i: Bull Volc v. 72:149–164 doi:10.1007/s00445-009-0315-5.

Schumacher R, Schmincke HU (1991) Internal structure and occurrence of accretionary lapilli: A case study at Laacher See volcano. Bull Volc 53:612-634

Shcherbakov, V. D., Plechov, P. Y., Izbekov, P. E., & Shipman, J. S. (2011). Plagioclase zoning as an indicator of magma processes at Bezymianny Volcano, Kamchatka. Contributions to Mineralogy and Petrology, 162, 83-99.

Stoiber, R., & Carr, M. (1973). Quaternary volcanic and tectonic segmentation of Central America. Bulletin Volcanologique, 37, 304-325.

Syracuse, E. M., & Abers, G. A. (2006). Global compilation of variations in slab depth beneath arc volcanoes and implications. Geochemistry, Geophysics, Geosystems, 7(5).

Taddeucci J, Pompilio M, Scarlato P (2004) Conduit processes during the July–August 2001 explosive activity of Mt. Etna (Italy): inferences from glass chemistry and crystal size distribution of ash particles. Jour Volc Geother Res 137:33-54

Taddeucci J, Pompilio M, Scarlato P (2007) Monitoring the explosive activity of the July–August 2001 eruption of Mt. Etna (Italy) by ash characterization. Geophys Res Lett 29:71-1

Valentine GA, Groves KR (1996) Entrainment of country rock during basaltic eruptions of the Lucero volcanic field, New Mexico. Jour Geol 104:71-90

Van Eaton AR, Muirhead JD, Wilson CJN, Cimarelli C (2012) Growth of volcanic ash aggregates in the presence of liquid water and ice: an experimental approach. Bull Volc 74:1963–1984

White, James DL, and Greg A. Valentine. "Magmatic versus phreatomagmatic fragmentation: absence of evidence is not evidence of absence." Geosphere 12.5 (2016): 1478-1488.

Webcam eruption footage from El Pacayal volcano:
http://www.marn.gob.sv. (https://www.youtube.com/watch?v=x5NOqUajIkk)

Map showing location of Volcan de San Miguel, San Miguel, El Salvador:
Google Earth, earth.google.com/web/.

Appendix

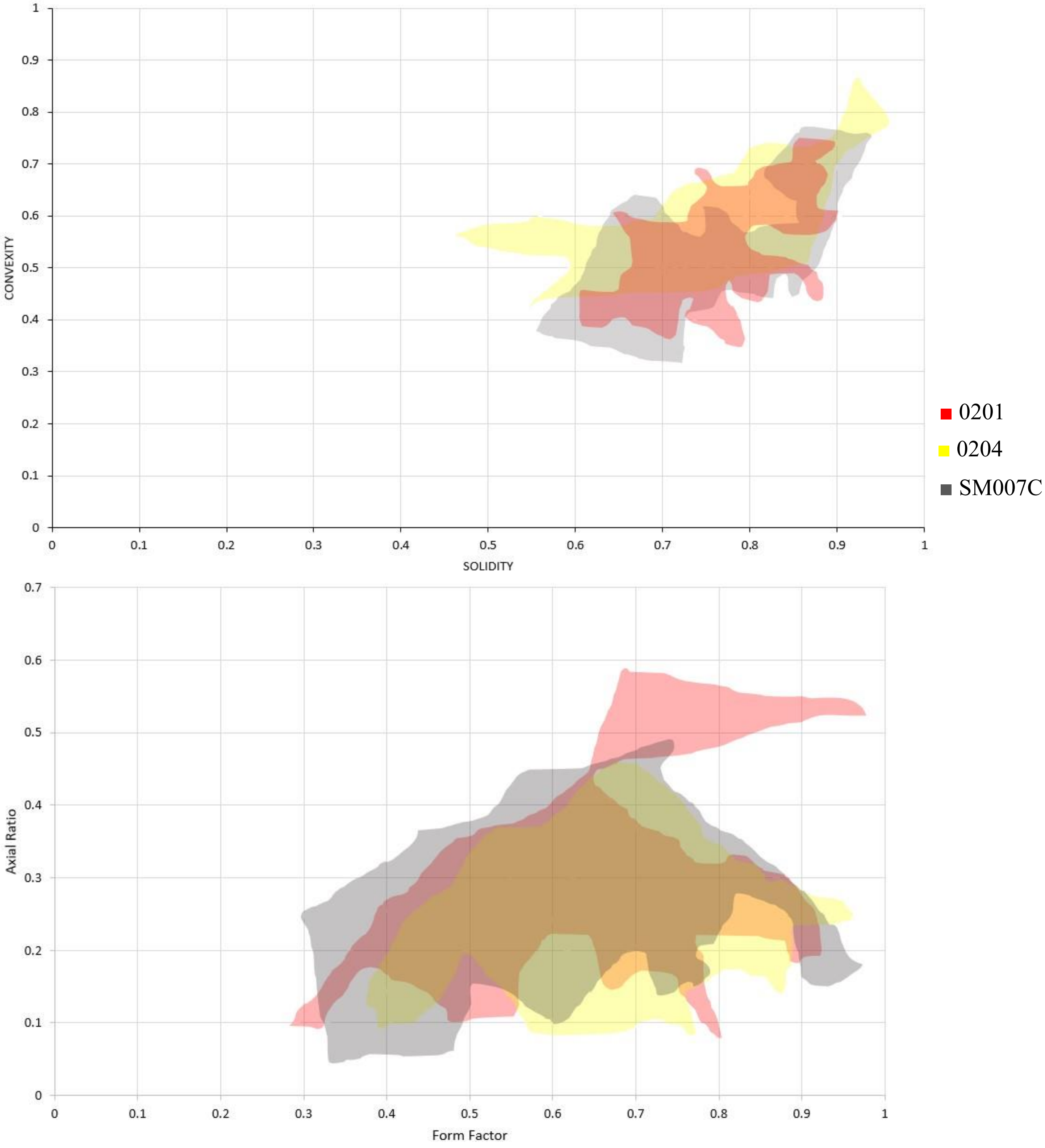

Figure 4.3.1. San Miguel samples 0201 (red), 0204 (yellow) and SM007C (grey): Comparison of convexity, solidity, axial ratio and form factor.

Figure 4.3.2a. Comparison of convexity and solidity for San Miguel and selected historic eruptions (Liu et al., 2015).

Figure 4.3.2b. Comparison of convexity and solidity for San Miguel and selected historic eruptions (Liu et al., 2015).

Figure 4.3.3a. Comparison of axial ratio and form factor for San Miguel and selected historic eruptions (Liu et al., 2015).

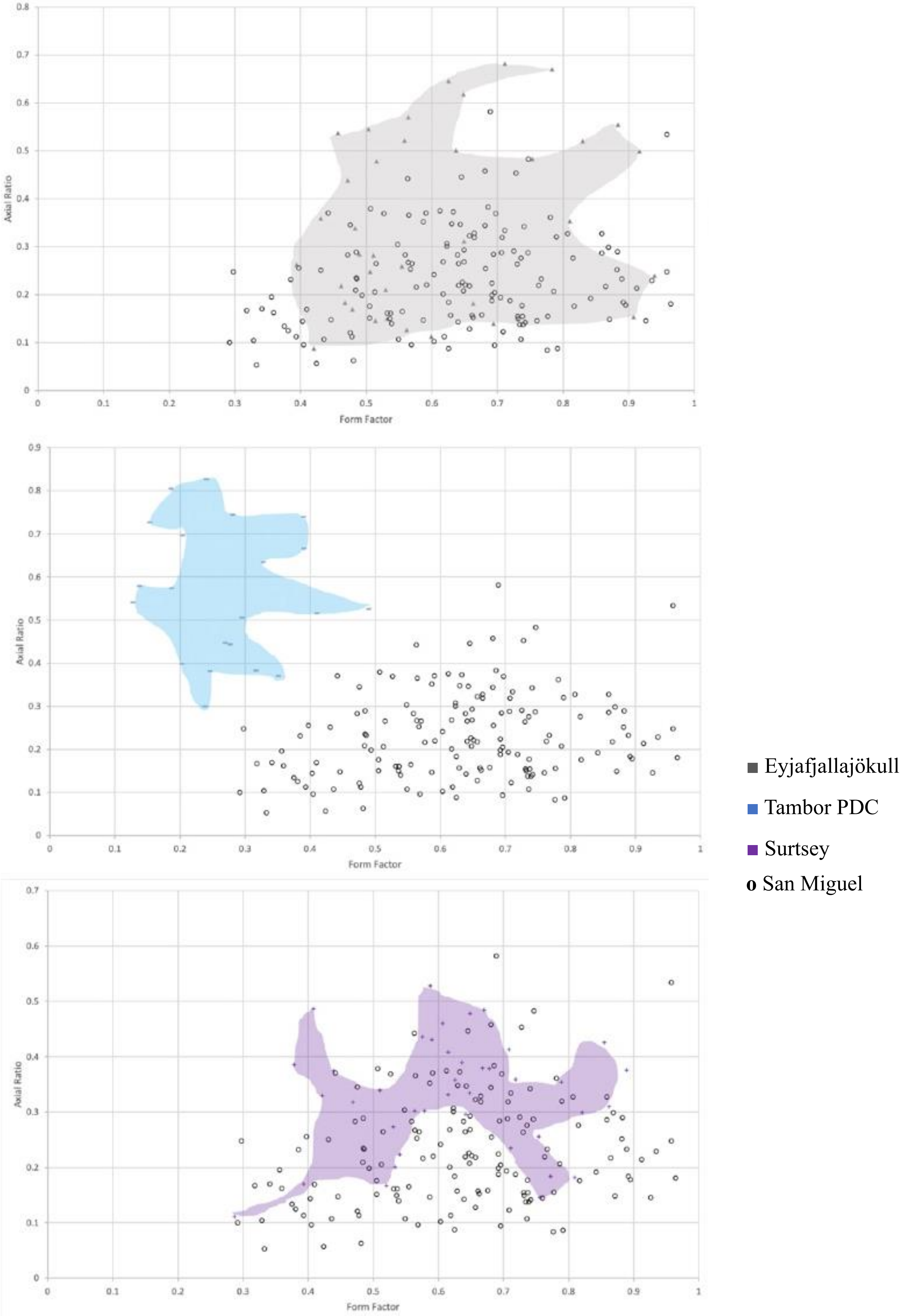

Figure 4.3.3b. Comparison of axial ratio and form factor for San Miguel and selected historic eruptions (Liu et al., 2015).